Summer 8-15-2018

Development and Application of Quadratic Constitutive Relation and Transitional Crossflow Effects in the Wray-Agarwal Turbulence model

Hakop Jack Nagapetyan
Washington University in St. Louis

WASHINGTON UNIVERSITY IN ST. LOUIS

School of Engineering & Applied Science
Department of Mechanical Engineering & Material Science

Dissertation Examination Committee:
Dr. Ramesh Agarwal, Chair
Dr. Kenneth Jerina
Dr. Swami Karunamoorthy
Dr. David Peters
Dr. Palghat Ramachandran

Development and Application of Quadratic Constitutive Relation and Transition Crossflow Effects in the Wray-Agarwal Turbulence model

by
Hakop J. Nagapetyan

A dissertation presented to
The Graduate School
of Washington University in
partial fulfillment of the
requirements for the degree
of Doctor of Philosophy

August 2018
St. Louis, Missouri

Table of Contents

List of Figures

List of Tables

Nomenclature

CFD	=	Computational Fluid Dynamics
C_f	=	Skin friction coefficient
C_p	=	Pressure coefficient
ν	=	Molecular kinematic viscosity
μ	=	Molecular dynamic viscosity
γ	=	Intermittency
$\tilde{\gamma}$	=	Heat capacity ratio
λ^+	=	Crossflow pressure gradient parameter
$\lambda_{\theta L}$	=	Local pressure gradient parameter
F_{PG}	=	Pressure gradient function
Tu_L	=	Local turbulence intensity
He	=	Helicity
H	=	Shape Factor
Re	=	Reynolds number, $\rho u_\infty c/\mu$
Re_v	=	Local vorticity Reynolds number
$Re_{\theta c}$	=	Critical momentum thickness Reynolds number
Re_{He}	=	Helicity Reynolds number
S	=	Strain rate magnitude
ρ	=	Density
P	=	Pressure
$\vec{u}$	=	Velocity vector, m/s

$\vec{s}$	=	Streamline vector
d_w	=	Distance to nearest wall, m
u_∞	=	Freestream velocity, m/s
P_∞	=	Freestream pressure, Pa
C	=	Crossflow constant
c	=	Chord length
D_1	=	NASA Glenn S-Duct inlet diameter
f_1	=	Blending function of Wray-Agarwal model
f_μ	=	Wall damping function of SA model and Wray-Agarwal model
k	=	Turbulent kinetic energy
M	=	Mach number
F_d	=	Drag force
F_l	=	Lift force
C_d	=	Drag coefficient
C_l	=	Lift coefficient
P_R^{lim}	=	Turbulent production term in WA-γ transition model
P_w	=	Wall pressure
T	=	Wall temperature
R	=	Undamped eddy viscosity, k/ω
RANS	=	Reynolds-Averaged Naiver-Stokes
S	=	Mean strain rate magnitude
SA	=	Spalart-Allmaras
SST	=	Shear Stress Transport
s	=	NASA Glenn S-Duct centerline curve length

u	=	x-component of velocity
v	=	y-component of velocity
W	=	Mean vorticity magnitude
WA	=	Wray-Agarwal
y^+	=	Non-dimensional wall distance
Δ	=	Grid spacing
ε	=	Turbulent dissipation
ν_T	=	Turbulent viscosity
$\tilde{\nu}$	=	Transport variable of Spalart-Allmaras model
ρ	=	Density
ω	=	Specific turbulent dissipation rate

Acknowledgments

I would like to extend my gratitude to my advisor, Dr. Ramesh Agarwal. His confidence in my abilities as well as his patience and guidance has helped make this work possible. He has set an example of excellence as a mentor, researcher, and role model.

Thanks to the committee members and MEMS staff for both their time and assistance during my time at Washington University in St. Louis.

I would also like to thank all my peers who helped me with all the technical aspects of my work. My colleagues at the CFD lab provided invaluable collaboration and comradeship that helped me keep pace with my work.

A special thanks to my family for their unwavering love and support, which helped keep me motivated and focused in my educational career.

The financial support for this work was provided by the NASA Space Grant and is gratefully acknowledged.

Hakop J. Nagapetyan

Washington University in St. Louis

August 2018

Abstract of the Dissertation

Development and Application of Quadratic Constitutive Relation and Transition Crossflow Effects in the Wray-Agarwal Turbulence model

by

Hakop J. Nagapetyan

Doctor of Philosophy in Mechanical Engineering

Washington University in St. Louis, 2018

Research Advisor: Ramesh Agarwal

Computational Fluid Dynamics (CFD) has now become an almost indispensable tool for modern engineering analysis of fluid flow over aircrafts, turbomachinery, automobiles, and many other industrial applications. Accurate prediction of turbulent flows remains a challenging problem. The most popular approach for simulating turbulent flows in complex industrial applications is based on the solution of the Reynolds-Averaged Navier-Stokes (RANS) equations. RANS equations introduce the so called "Reynolds or turbulent stresses" which are generally modeled using the Boussinesq approximation known as "Turbulence modeling." Despite their development over a century, the turbulence models used with RANS equations still need much improvement. The first part of this research introduces the Quadratic Constitutive Relations (QCR), which is a nonlinear approach to approximating the turbulent stresses in eddy-viscosity class of turbulence models. In Boussinesq approximation, turbulent stresses are assumed to be linearly proportional to the strain with eddy viscosity being the proportionality constant. In recent years it has been found that linear eddy viscosity models are not accurate for prediction of vortical flows and wall bounded flows with mild separation with regions of recirculating flows. Such flows occur in junctions of aerodynamic surfaces e.g. the wing-body junction and in inlets and ducts with corners. The

accurate prediction of these flows is needed for design improvements and better product performance. To remedy some of the shortcomings of the linear eddy-viscosity models, the Quadratic Constitutive Relation (QCR) for eddy viscosity is investigated to test its capability for predicting non-equilibrium turbulence effects. QCR is implemented in Spalart-Allmaras (SA), SST k-ω and Wray-Agarwal (WA) turbulence models and is applied to several applications involving large recirculating regions. It is demonstrated That QCR improves the results compared to linear eddy viscosity models. Another shortcoming of RANS models is their inability to accurately predict regions of transitional flow in a flow field. Many flow regions in industrial applications contain the transitional flow regime e.g. flows over aircraft wings and fuselages, past wind turbines and in gas turbines engines to name a few. The second part of this research has been on the development of a transitional model by suitably combining a correlation based intermittency-γ equation with the WA turbulence model; this new model is designated as Wray-Agarwal-γ (WA-γ) transition model. The WA-γ is extensively validated by computing a number of benchmark cases. The WA-γ model is also extended to include the crossflow-instability induced transition which is a dominant mode of transition in flows involving three-dimensional boundary layers, e.g. flow past swept wings and ellipsoids. This modified WA-γ model is validated using a benchmark test case for analyzing crossflow-induced transition.

Chapter 1: Introduction

1.1 Background and Motivation

Computational Fluid Dynamics (CFD) is an important tool in today's modern engineering analysis for aircraft, turbomachinery, automobiles, and many other industrial applications. Majority of flows in industrial applications are turbulent. Accurate prediction of turbulent flows remains a challenging problem. The most popular and widely used approach for simulating turbulent flows is the solution of the Reynolds-Averaged Navier-Stokes (RANS) equations. The RANS equations include 'turbulent stresses' that are modeled in order to achieve closure to the equations. RANS equations introduce a great deal of empiricism and despite their many decades of use, the turbulence models required with these equations still need much improvement; for example, these models can fail to accurately capture flow separation in wall bounded flows in adverse pressure gradients, and secondary flows in corner flows. Standard RANS models are also limited to the predictions of turbulent flow regimes and cannot predict transition. Many of the aforementioned industrial applications can undergo flow transition, which can greatly influence the performance of the industrial device/product.

1.2 Objectives

The goal of this research is to study ways to extend the capabilities of modern RANS models, or develop new turbulence models e.g. the newly developed one equation Wray-Agarwal turbulence model. The first part of the research in this dissertation introduces the Quadratic Constitutive Relations (QCR), which is a nonlinear approach to solving the turbulent stresses for eddy-viscosity models. Normally, eddy-viscosity models use a linear approach (the Boussinesq approximation) to model turbulent stresses, but they appear to lack the capability for prediction of vortical flows,

secondary flows, and wall bounded flows with mild separation (regions of recirculating flows). The secondary flows occur in junctions of aerodynamic surfaces e.g. the wing-body junction and in inlets and ducts. The accurate prediction of these flows is needed for design improvements and better performance of industrial devices. To remedy some of the shortcomings of the linear eddy-viscosity models, the Quadratic Constitutive Relation (QCR) for eddy viscosity has been proposed in the literature. The first part of this research aims to show that QCR can improve a turublence model's capability for predicting non-equilibrium turbulence effects.

Another shortcoming of RANS models is their inability to accurately predict regions of transitional flow. Many flow regions in industrial applications fall into the transition regime e.g. flows over aircraft wings and fuselages, past wind turbines and in gas turbines engines to name a few. The second part of this research aims at first developing and validating a transitional flow model with crossflow instabilities based on the Wray-Agarwal (WA) turbulence model. By including a correlation based intermittency (γ) model, the WA-γ transition model is validated by computing a number of test cases for transitional flow over a flat plate, simple and multi-element airfoils, and an inclined prolate spheroid.

1.3 Outline

The goal of this dissertation is twofold: (1) To examine the applicability of the QCR method when applied to RANS equations by numerically analyzing a number of benchmark test cases that contain secondary recirculating flows and (2) to extend the capabilities of original baseline WA model by including an intermittency equation based on the local correlation-based transition-modelling concept, and then extend this transition model concept to include three-dimensional geometries with the inclusion of a crossflow-instability model.

A brief summary of various chapters and their content is given below:

Chapter 2: Turbulence Modeling: This chapter briefly describes the concept of turbulent flows and turbulence modeling. The main approach for computing turbulent flows namely the Reynolds-Averaged Navier-Stokes (RANS) equations and eddy-viscosity models are introduced along with the formulation of the newly developedWray-Agarwal turbulence model. The concept behind the Quadratic Constitutive Relation and the local correlation-based transition-modelling are briefly discussed. A brief introduction to computational fluid dynamics (CFD) is given, along with the software employed for developing and testing the new models. OpenFOAM is used to develop the new models and compute the validation cases.

Chapter 3: The Quadratic Constitutive Relation: In this chapter, the formulation of the Quadratic Constitutive Relation is given. Numerical results of benchmark and validation test cases are provided to show that the QCR relation does not degrade the performance of the linear eddy-viscosity models; it only improves the performance and some cases dramatically. To show substantial improvement in results using QCR in turbulence models, several benchmark cases of corner flows test in ducts are computed for both incompressible and compressible flow.

Chapter 4: Laminar-Turbulent Transition: This chapter provides a detailed implementation of the intermittency equation with the Wray-Agarwal Wall-distance free turbulence model, which results in the WA-γ transition model. The transition correlation constants in the WA-γ model are validated by computing the benchmark test cases of flow past a flat plate in zero-pressure gradient and in pressure gradient comparing the results with the experimental data from ERCOFTAC online database. Several other application test cases for flows over airfoils and non-symmetrical bodies

are also computed to show the accuracy of this transition model compared to other existing transition models in the literature.

Chapter 5: Implementation of Crossflow Transition Effects in the WA-γ Model: A brief introduction of crossflow-instability induced transition is given, followed by a detailed implementation of the crossflow transition correlation into the local correlation-based WA-γ transition model described in chapter 4 to develop the WA-γ-Crossflow transition model. The new model is validated by performing numerical analysis of flow over a prolate spheroid, which is a benchmark test case for analyzing crossflow-induced transition.

Chapter 6: Summary and Future Work: This chapter provides a summary of the work accomplished in this dissertation with discussion of the results obtained with the integration of QCR in existing turbulence models (SA and SST k-ω) and in the WA model, and the newly developed WA-γ transition model. Future work describes ways to extend the WA-γ transition model to include the roughness effects.

Chapter 2: Introduction to Turbulence Modeling

2.1 Reynolds-Averaged Navier Stokes Equations

Laminar flow behavior can be calculated precisely using the Navier-Stokes equation if the boundary of a laminar flow region can be accurately described. This is because laminar flow is determined by a single length scale, which typically comes from the boundaries of the flow region. On the contrary, when flow becomes turbulent the fluctuations can only be fully characterized by an infinite number of length and time scales that vary from small to large values. The oldest model developed to mathematically approximate turbulent flow behavior is based on time-averaging of the Navier-Stokes equations which results in the Reynold-Averaged Navier-Stokes (RANS) equations. RANS averaging result in “turbulent stresses” or “Reynolds Stresses” that require modeling using empiricism. The most common models are the linear eddy-viscosity type transport models, being the simplest models that can be easily solved with RANS equations. However, they are not accurate in modeling flow separation, secondary flows in curved ducts and corners, vortical and recirculating flows, and flow transition.

2.2 Eddy-Viscosity Turbulence Models

The most common turbulence models are the linear eddy-viscosity type transport models, being the simplest models that can be easily solved with RANS equations. “Reynolds Stresses” are usually modeled using the eddy viscosity concept in the stress-strain constitutive relation. These models solve the turbulent transfer of momentum by eddies giving rise to an internal fluid friction. The models have many empirical relations and coefficients which are determined by comparison of the computations with the experimental data. Although no model has clearly emerged as superior, the Spalart-Allmaras (SA) one equation eddy-viscosity model [1] and the Shear Stress

Transport (SST) k-ω two equation model [2] are the most prevalent and widely used turbulence models in the industry. The versatility of these models in computing many aerodynamic flows with reproducible results using majority of CFD solvers makes them very popular. However, there are difficulties and challenges in predicting turbulent flows over complex 3D geometries with massive separation that need to be addressed; they cannot be accurately predicted by SA or SST k-ω models. This is due to the models containing a great deal of empiricism that has resulted in model coefficients to be calibrated for only a small number of simple shear and wall bounded flows.

2.3 Wray-Agarwal Turbulence Model

The recently developed one equations Wray-Agarwal turbulence model [3] (WA2017) is a new linear eddy-viscosity turbulence model derived from *k-ω* closure. In this model, a new variable *R* is introduced which is defined as *k*/*ω*. It includes a cross diffusion term and a blending function f_1 to switch between the two destruction terms. The equation of WA2017 model is shown in Eq. (2.1).

$$\frac{\partial R}{\partial t}+\frac{\partial u_j R}{\partial x_j}=\frac{\partial}{\partial x_j}\left[(\sigma_R R+\nu)\frac{\partial R}{\partial x_j}\right]+C_1 RS+f_1 C_{2k\omega}\frac{R}{S}\frac{\partial R}{\partial x_j}\frac{\partial S}{\partial x_j} - (1-f_1)C_{2k\varepsilon}R^2\left(\frac{\frac{\partial S}{\partial x_j}\frac{\partial S}{\partial x_j}}{S^2}\right) \tag{2.1}$$

The turbulence eddy viscosity is given by the equation:

$$\nu_T = f_\mu R \tag{2.2}$$

The wall blocking effect is accounted for by the damping function f_μ. The value of C_w was determined by calibrating the model to a simple zero pressure gradient flat plate flow. ν has the usual definition of kinematic viscosity.

$$f_\mu = \frac{\chi^3}{\chi^3 + {C_w}^3}, \qquad \chi = \frac{R}{\nu} \tag{2.3}$$

S is the mean strain described below.

$$S = \sqrt{2S_{ij}S_{ij}}\,, \qquad S_{ij} = \frac{1}{2}\left(\frac{\partial u_i}{\partial x_j} + \frac{\partial u_j}{\partial x_i}\right) \tag{2.4}$$

The model can behave either as a one equation *k-ω* or one equation *k-ε* model based on the switching function f_1. The switching function f_1 is limited by an upper value of 0.9 for better stability.

$$f_1 = min(tanh(arg_1^4), 0.9) \tag{2.5}$$

$$arg_1 = \frac{1 + \frac{d\sqrt{RS}}{\nu}}{1 + \left[\frac{max\left(d\sqrt{RS}, 1.5R\right)}{20\nu}\right]^2} \tag{2.6}$$

The values of constants used in WA2017 model are listed below [4].

$$\begin{gathered} C_{1k\omega} = 0.0829 \quad C_{1k\varepsilon} = 0.1127 \\ C_1 = f_1(C_{1k\omega} - C_{1k\varepsilon}) + C_{1k\varepsilon} \\ \sigma_{k\omega} = 0.72 \quad \sigma_{k\varepsilon} = 1.0 \\ \sigma_R = f_1(\sigma_{k\omega} - \sigma_{k\varepsilon}) + \sigma_{k\varepsilon} \\ \kappa = 0.41 \\ C_{2k\omega} = \frac{C_{1k\omega}}{\kappa^2} + \sigma_{k\omega} \quad C_{2k\varepsilon} = \frac{C_{1k\varepsilon}}{\kappa^2} + \sigma_{k\varepsilon} \\ C_w = 8.54 \end{gathered} \tag{2.7}$$

The WA2017 model has shown improved accuracy over the SA model as well as being competitive with the SST *k-ω* model for a wide variety of wall-bounded and free shear layer flows [4]. The WA2017 model has the advantage in efficiency over multi-equation models in computational cost. Even though the WA2017 model appears promising, it also has limitations in accuracy for computing secondary flows and transitional flows.

2.4 The Quadratic Constitutive Relation

In an attempt to improve RANS models, specifically linear eddy-viscosity models, new empirical terms in the Reynolds-stress tensor are added. The Quadratic Constitutive Relation (QCR)[5] modifies the traditional linear model of the Reynolds-stress tensor into a nonlinear form. The approximation introduces a fair level of anisotropy within the outer region of a simple boundary layer $u'^2 > w'^2 > v'^2$ (the streamwise, spanwise and wall-normal Reynolds stresses, respectively). This approximation has shown improved results for some corner flows, but overall very limited testing has been done using this nonlinear approximation. QCR can improve a model's capability for predicting non-equilibrium turbulence effects. This work investigates the influence of QCR by applying it to the Spalart-Allmaras (SA), Shear-Stress-Transport (SST) k-ω, and WA models. The SA - QCR, SST - QCR and WA- QCR models and standard SA, SST k-ω, and WA models are used to compute several canonical flows. Formulation of QCR is derived in a later section of this thesis.

2.5 Laminar-Turbulent Transition Modeling

Transition modeling has been a very challenging task in the turbulence modeling community due to many factors; lack of experimental data, complexity of transition physics, and the fact that transition can occur in at least four different modes which are known in the literature as natural transition, bypass transition, separation-induced transition, and crossflow induced transition. It is unlikely that all these mechanisms of transition, or even a few of them, could be modeled in physics-based equations framework. Currently, the most widely known and used model for computing transition is the four-equation SST-Transition model developed by Menter et al. [2]. This model is based on three correlations, which are functions of the local transition onset momentum thickness Reynolds number obtained from a transport equation. Recently, a three-

equation model was developed based on the local correlation-based transition-modeling (LCTM) concept, removing the need for a transport equation for the transition onset momentum thickness Reynolds number [6]. The LCTM concept was developed as a unified concept, which could eventually handle all different mechanisms of transition. LCTM is a set of CFD compatible transport equations, which allow combining experimental correlations in a local fashion with the underlying turbulence model. This work intends to extend the capabilities of the WA turbulence model capabilities with the LCTM concept and run benchmark transition validation and application test cases. The goal is to create a WA transition model that will be Galilean invariant, provide meaningful coefficients that can be easily fine-tuned to match specific application areas, and reduce the formulation to a two transport equation transition model with substantially improved efficiency.

2.6 OpenFOAM

All numerical analysis in this research was performed using the CFD flow solver OpenFOAM (Open source Field Operation And Manipulation). OpenFOAM is an open source CFD software developed on Linux operating system initially released in 2004. The software continues to be supported by the addition of all kinds of CFD capability in complex fluid physics modeling, type of grids and numerical algorithms, and turbulence models. It has several well-known turbulence models; namely the SA model, SST k-ω model, and k-ϵ model. It can therefore be used for wide range of applications, including incompressible and compressible turbulent flows, buoyancy-driven flows, multiphase flows, and turbulent flow applications with heat transfer, combustion and particle dynamics etc.

In contrast to other commercial CFD software, OpenFOAM provides the source code which makes it easy to modify and to add new models, algorithms and other upgrades. It has been developed in

C++ programming language which has many good features like modularity and extensibility. Users can easily and effectively develop and test the new CFD capability. This is a much less tedious process to implement new capability in OpenFOAM than in executable commercial software.

All simulation in this work are performed using OpenFOAM, and new models are developed and implemented as OpenFOAM libraries. All simulations use second-order upwind discretization or similar second order accurate schemes for the convection terms and second-order central differencing for viscous terms. All incompressible simulations use steady-state solution schemes, with a few exceptional cases using a combination of transient and steady-state solution schemes using the PISO and SIMPLE algorithms respectively, to reach a converged solution. Compressible cases utilize a local transient solver based on Kurganov-Tadmore scheme for compressible flows and PISO method.

Chapter 3: The Quadratic Constitutive Relation

3.1 Formulation

The QCR relation has no effect on how the three turbulence models solve for the eddy viscosity but instead it alters the way turbulent stresses are calculated. The traditional linear Boussinesq relation gives:

$$\tau_{ij} = 2\mu_t \left(S_{ij} - \frac{1}{3}\frac{\partial u_k}{\partial x_k}\delta_{ij} \right) - \frac{2}{3}\rho k \delta_{ij} \tag{3.1}$$

The QCR relation modifies Eq. (3.1) to the following form:

$$\tau_{ijQCR} = \tau_{ij} - C_{cr1}\left[O_{ik}\tau_{jk} + O_{jk}\tau_{ik} \right] \tag{3.2}$$

where τ_{ij} are the turbulent stresses computed from the linear Boussinesq relation (3.1) and O_{ik} is an antisymmetric normalized rotation tensor defined as:

$$O_{ik} = 2\,W_{ik} \Big/ \sqrt{\frac{\partial u_m}{\partial x_n}\frac{\partial u_m}{\partial x_n}} \tag{3.3}$$

$$W_{ik} = \frac{1}{2}\left(\frac{\partial u_i}{\partial x_k} - \frac{\partial u_k}{\partial x_i} \right) \tag{3.4}$$

The denominator of the Eq. (3.3) for O_{ik} expands to:

$$\sqrt{\frac{\partial u_m}{\partial x_n}\frac{\partial u_m}{\partial x_n}} = \sqrt{u_x^2 + u_y^2 + u_z^2 + v_x^2 + v_y^2 + v_z^2 + w_x^2 + w_y^2 + w_z^2} \tag{3.5}$$

Thus QCR can be used with any turbulence model that employs the Boussinesq relation for computation of eddy viscosity. Additional information about the QCR relation can be found in Ref. [5].

3.2 Computation of Benchmark Flows

3.2.1 Flat Plate Flow

A turbulent flat plate boundary layer is a widely used simple verification and validation test case. RANS turbulence models have no problem in accurately predicting the turbulent boundary layer and are often calibrated by computing this flow. The Reynolds number of the flow is Re = $5x10^6$ based on the upstream flow of M = 0.2 and reference length of one meter. The computational grids used were taken from the NASA Turbulence Modeling Resource (TMR) website [7]. The computational grid with every other node and the boundary conditions are shown in Fig.3.1.

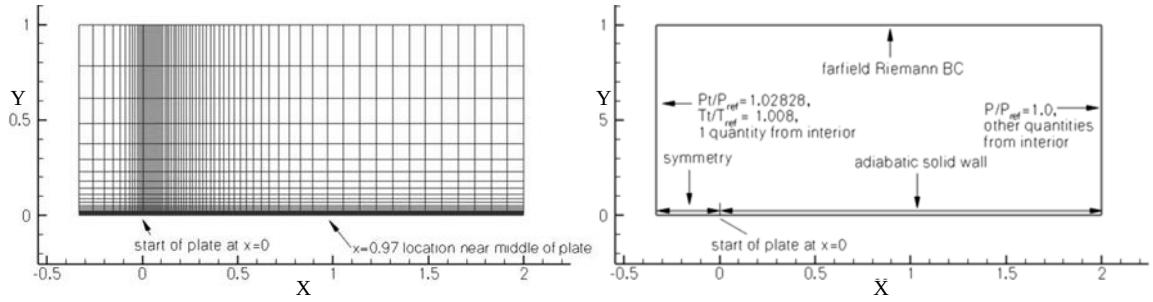

(a) **(b)**

Figure 3.1: Grid and boundary conditions for subsonic flow past a flat plate.

To test the correct implementation of QCR in OpenFOAM, QCR results were first compared to the standard models (SA and SST k – ω) results. Figures 3.2 and 3.3 show that the results of SA-QCR and SST-QCR for skin friction on the flat plate match very well with the standard SA and SST k-ω results from NASA TMR [7]. This calculation validates the QCR implementation in OpenFOAM. Figure 3.4 compares the skin friction obtained using WA-QCR with that obtained with SA-QCR and SST - QCR. The comparison shows that all three QCR models are in excellent agreement with one another as well as with the NASA TMR [7] results.

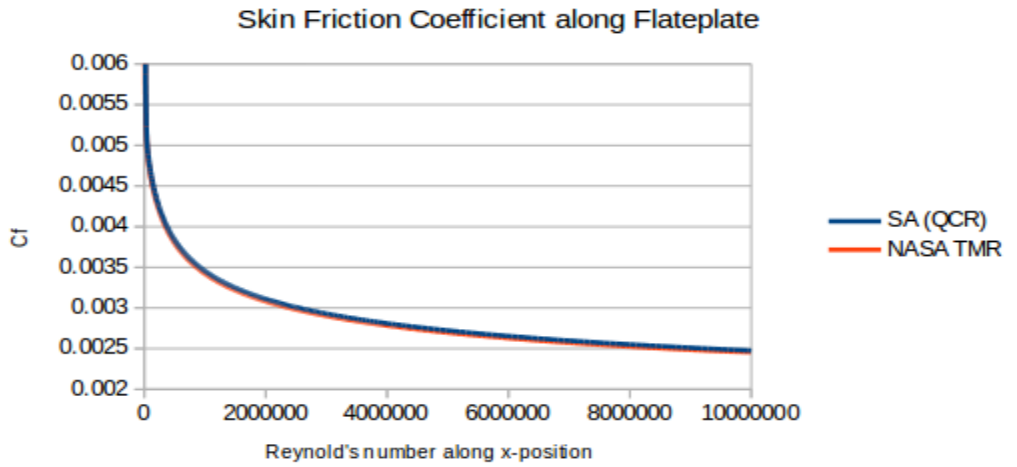

Figure 3.2: Skin Friction Coefficient results for SA - QCR compared to NASA TMR results [7].

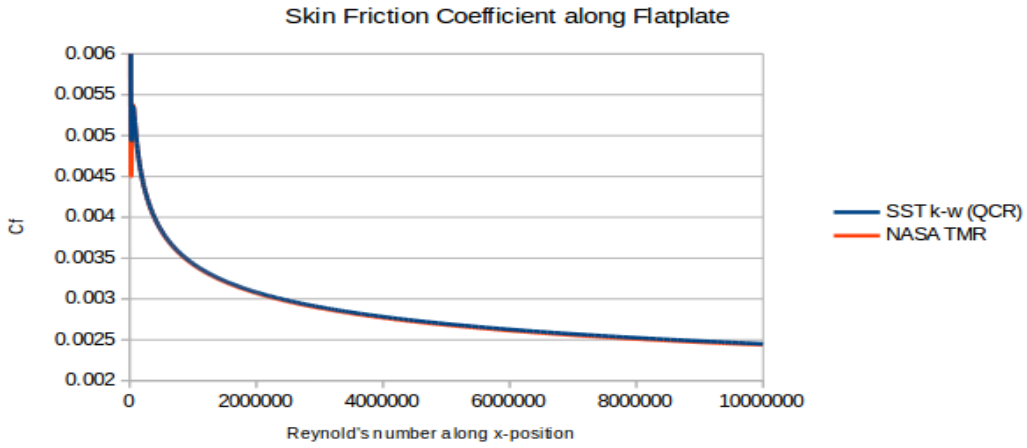

Figure 3.3: Skin Friction Coefficient results for SST - QCR compared to NASA TMR results [7].

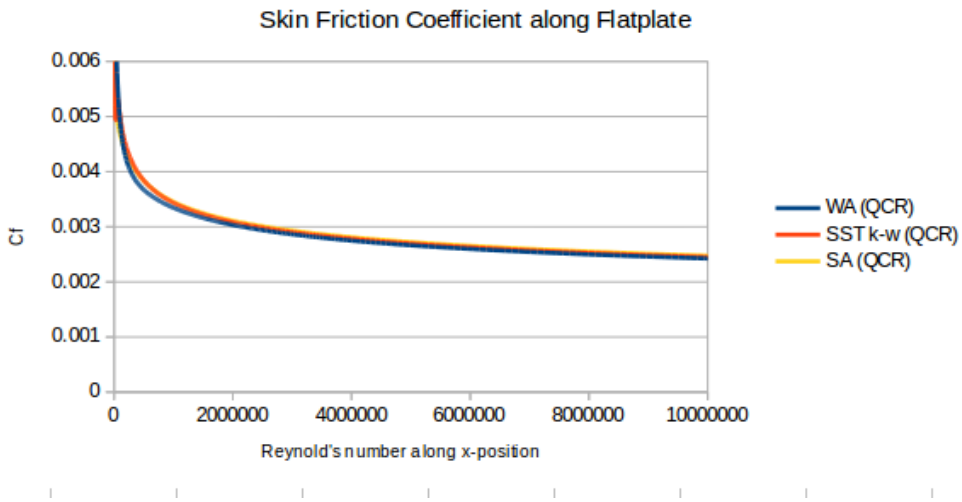

Figure 3.4: Skin Friction Coefficient results for WA - QCR compared to results from SA- QCR and SST-QCR.

Velocity profiles computed from different QCR models are also compared. Let u+ be the dimensionless velocity defined by:

$$u^+ = \frac{u}{u_\tau} \tag{3.6}$$

where u is the fluid velocity in the x-direction and u_τ is the shear velocity given by:

$$u_\tau = \sqrt{\frac{\tau_w}{\rho}} \tag{3.7}$$

In Eq. (3.7), τ_w is the wall shear stress calculated numerically by OpenFOAM and ρ is the density. The dimensionless y-coordinate away from the wall, $y+$, is given by the following equation:

$$y^+ = \frac{y * u_\tau}{v} \tag{3.8}$$

where ν is the kinematic viscosity. These dimensionless variables are calculated using the numerical solutions for wall shear stress and stream-wise velocity obtained with SA-QCR and SST-QCR at x = 0.97; these are compared to the results from NASA TMR as shown in Figs. 3.5 and 3.6.

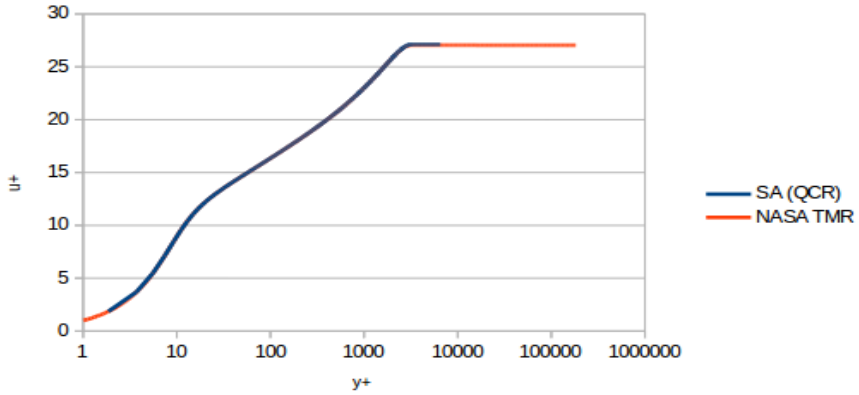

Figure 3.5: u+ at x=0.97 using SA-QCR and its comparison to the result from NASA TMR [7].

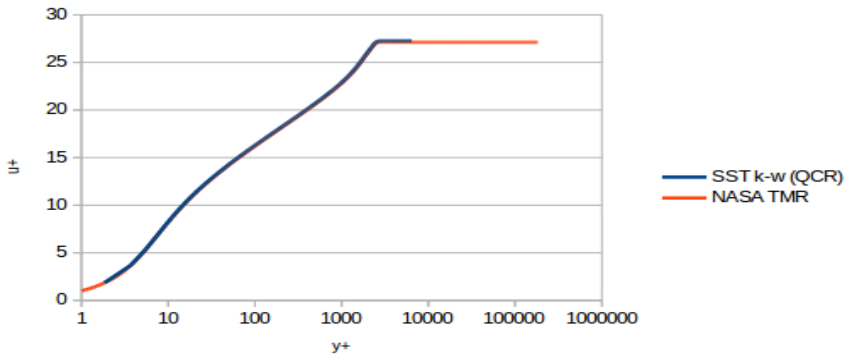

Figure 3.6: u+ at x=0.97 using SST-QCR and its comparison to the result from NASA TMR [7].

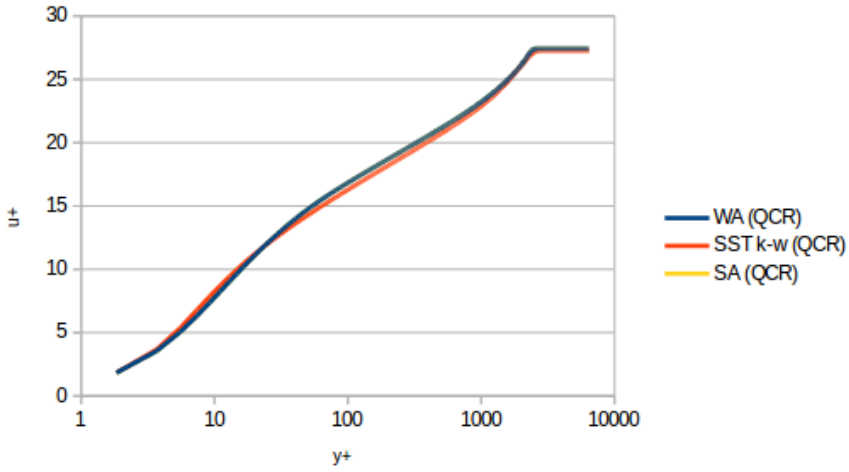

Figure 3.7: u+ at x=0.97 using WA-QCR and its comparison to results from SST-QCR and SA-QCR.

The QCR results for WA-QCR, SA-QCR and SST-QCR almost overlap with the NASA TMR results, validating the correct implementation of QCR in OpenFOAM. The comparison shows that all three models are in good agreement with one another, which is expected for this simple case.

3.2.2 Flow in a 2D Lid-Driven Square Cavity

Fluid flow in a lid-driven square cavity is computed at Re = 20,000. All sides of the cavity are considered to be of unit length. The lid has a velocity U=1 and the viscosity of the fluid is varied to achieve the desired Reynolds number. The Dirichlet boundary conditions are employed on the cavity wall as shown in Fig. 3.8. A 500 x 500 uniform mesh is employed.

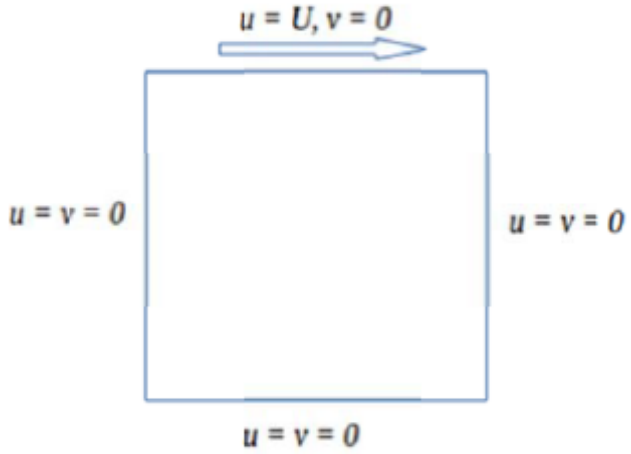

Figure 3.8: Boundary Conditions for a 2D lid-driven cavity flow.

The computed streamlines from Erturk et al. [8] are shown in Fig. 3.9. The results from this figure show multiple eddies in three of the four corners of the square cavity. Figures 3.10-3.12 show the streamlines for SA, SST k-ω, and WA models. The left hand side shows results using the standard linear eddy viscosity model and the right hand side shows results using QCR. The Boussinesq type linear eddy viscosity relation fails to capture the formation of all secondary eddies in the three corners using both the SA and SST k-ω models. The WA model is able to predict the corner eddies with or without the QCR. The SA model is significantly improved with the addition of QCR as it is able to predict the additional secondary eddies in the three corners as shown in Figure 3.9. The

streamlines of SST *k-ω* model shows some improvement with the addition of QCR with the formation of additional eddies in the three corners.

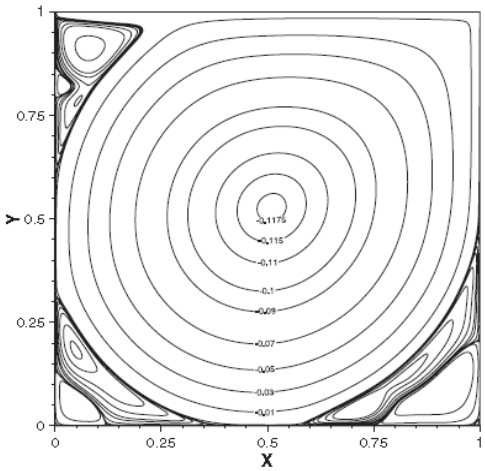

Figure 3.9: Streamline contours from Erturk et al. [8] at Re=20,000.

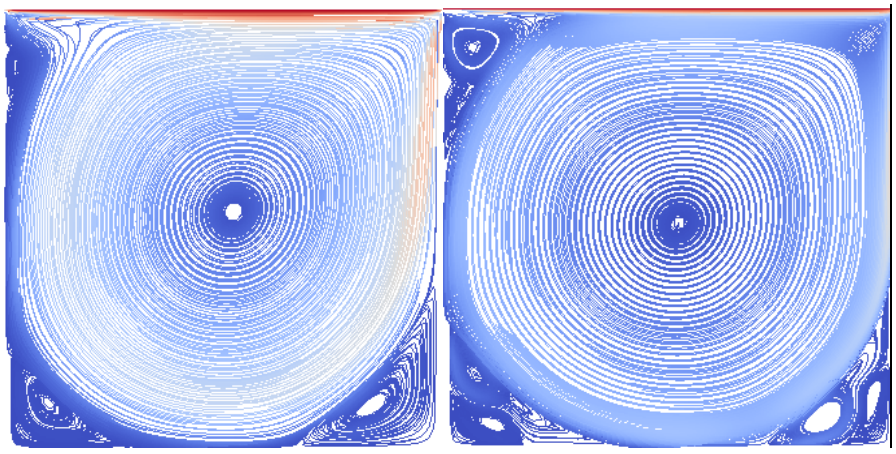

Figure 3.10: Streamline contours for SA (left) and SA-QCR (right) at Re=20,000.

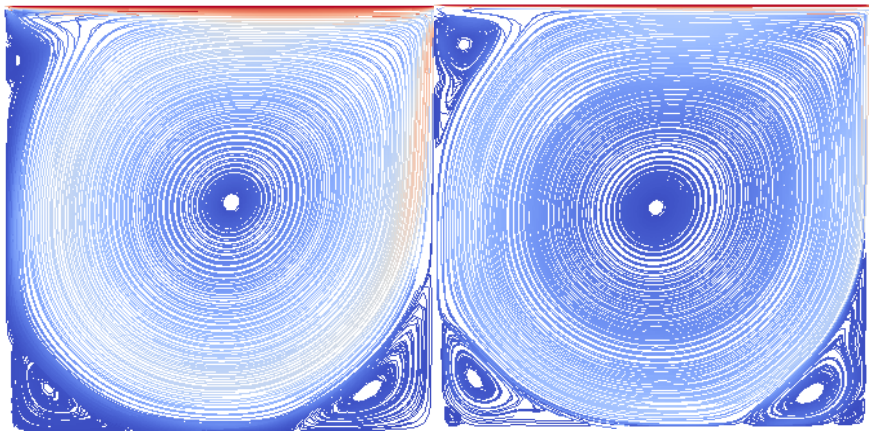

Figure 3.11: Streamline contours for SST k-ω (left) and SST-QCR (right) at Re=20,000.

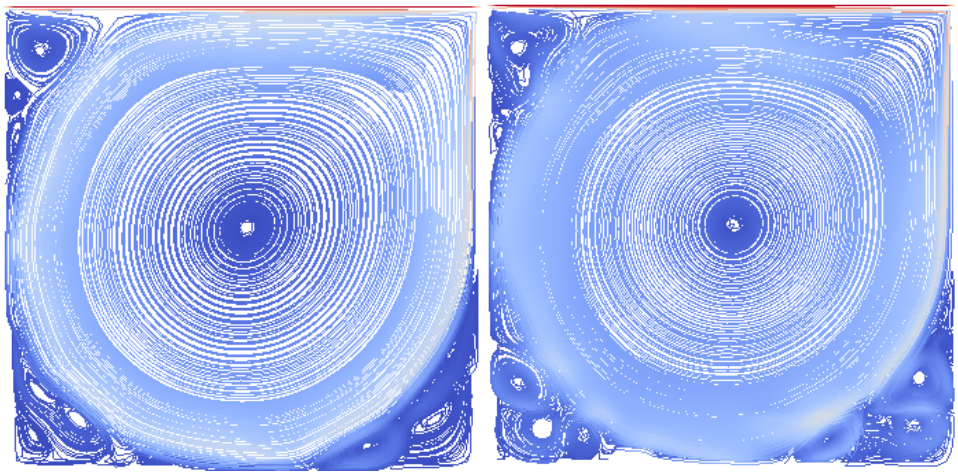

Figure 3.12: Streamline contours for WA (left) and WA-QCR (right) at Re=20,000.

In Figs. 3.13-3.15, velocity components, *v* and *u*, along the horizontal and vertical centerlines of the cavity obtained with standard linear eddy viscosity model and corresponding QCR model are compared for SA, SST k-ω and WA models respectively. It can be seen from Fig. 3.13 that the application of QCR to the SA model improves the solution accuracy compared to the standard SA model. For SST k-ω model, no significant change is observed between the result from standard SST and SST-QCR model as shown in Fig. 3.14. Figure 3.15 shows that the WA-QCR results show a minor improvement in v-velocity component along the horizontal centerline but no significant change in the *u*-velocity component along the vertical centerline when compared to the Standard WA model.

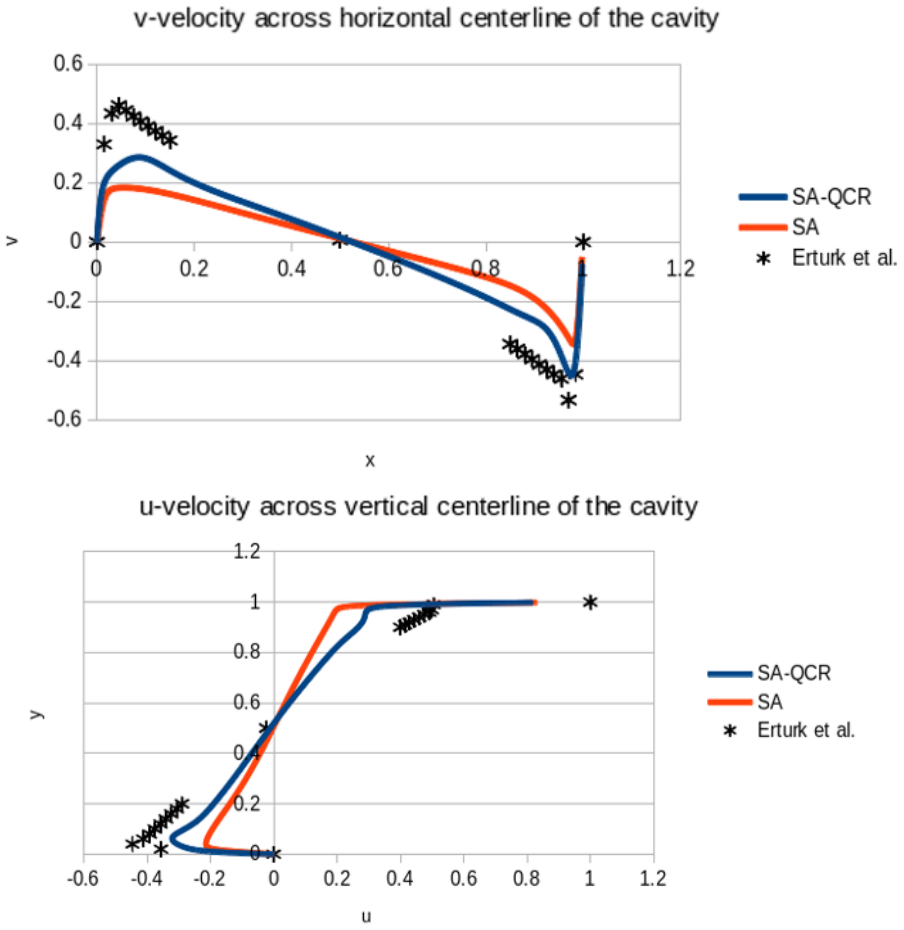

Figure 3.13: Numerical results of SA and SA-QCR models compared to solutions from Erturk et al [8].

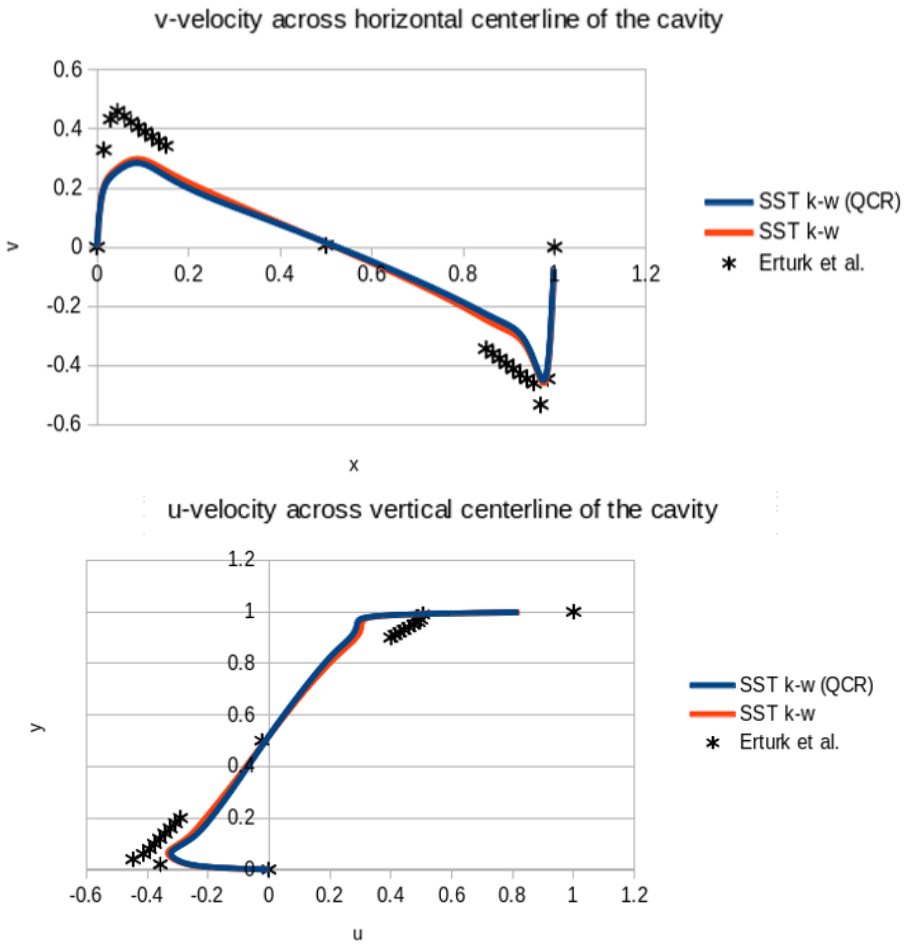

Figure 3.14: Numerical results of SST and SST-QCR models compared to solutions from Erturk et al [8].

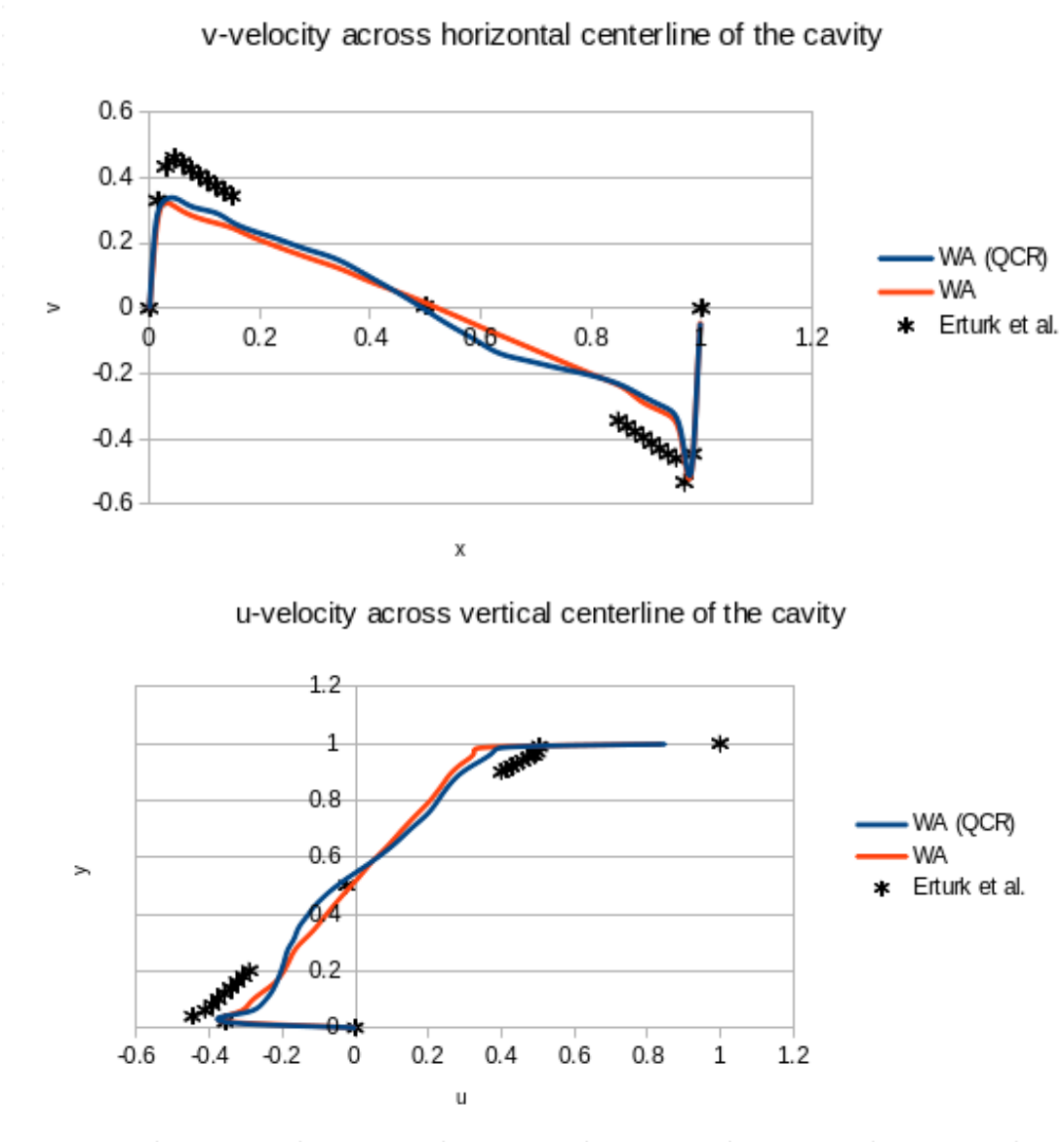

Figure 3.15: Numerical results of WA and WA-QCR models compared to solutions from Erturk et al [8].

3.2.3 Flow over a Backward Facing Step

Flow over a backward facing step is a widely-tested benchmark separated flow case. In this case, a turbulent boundary layer upstream encounters a sudden back step causing flow separation. The flow reattaches downstream of the step on the lower wall. The simulations were run to match the flow conditions of the experiment of Driver and Seegmiller [9]. The freestream velocity is M=0.128. The Reynolds number based on the step height and free stream velocity is Re=36,000.

Figures 3.16-3.18 show the comparison of experimental pressure coefficient and skin friction coefficient obtained from NASA TMR [7] and the results computed with standard SA, SST k-ω and WA models, and SA-QCR, SST-QCR and WA-QCR models respectively. The figures indicate that there is minor improvement (less than 1%) with the application of QCR compared to standard models. WA and WA-QCR results however show better agreement with the initial detachment of the flow near the back step boundary compared to SA and SST k-ω models.

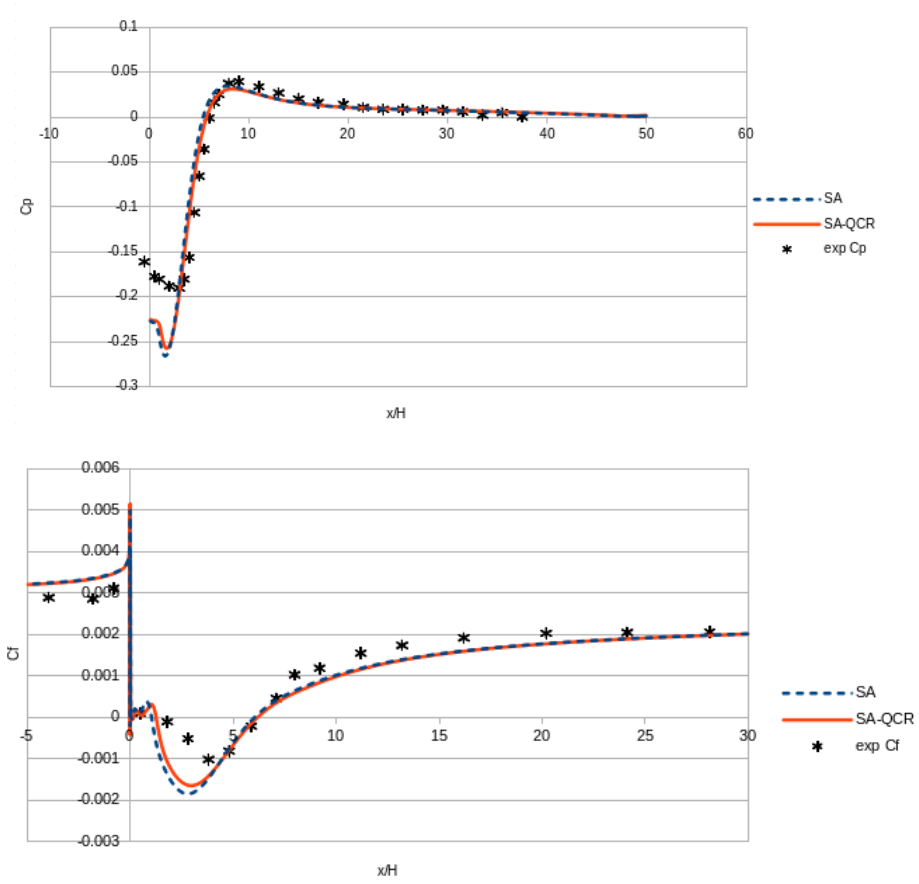

Figure 3.16: Cp and Cf from SA and SA-QCR models compared to experimental results [7]

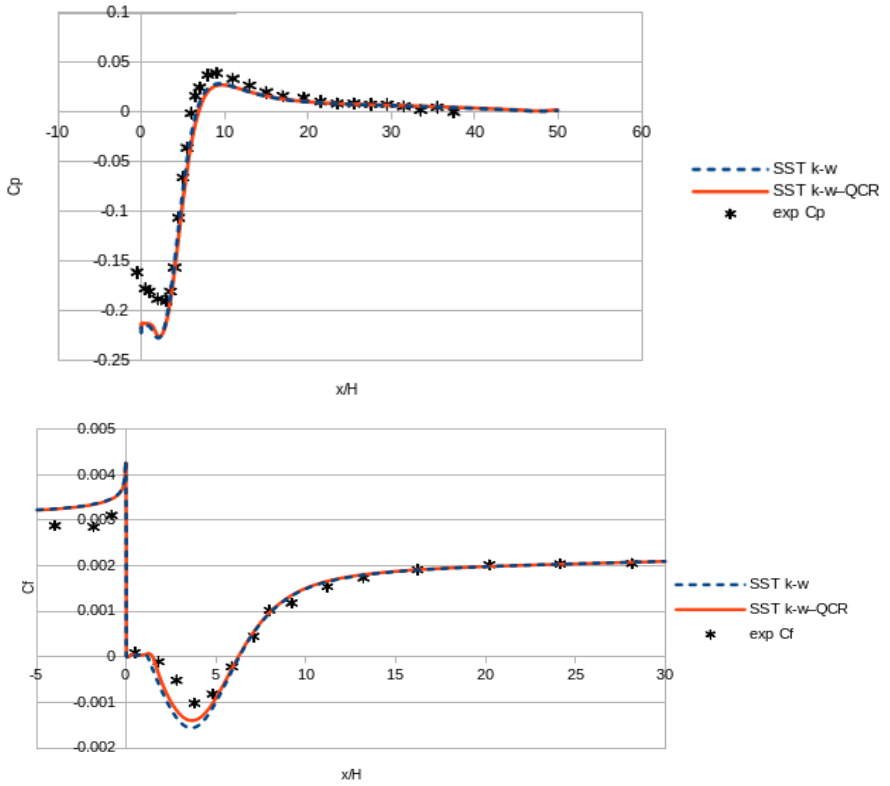

Figure 3.17: Cp and Cf from SST and SST-QCR models compared to experimental results [7]

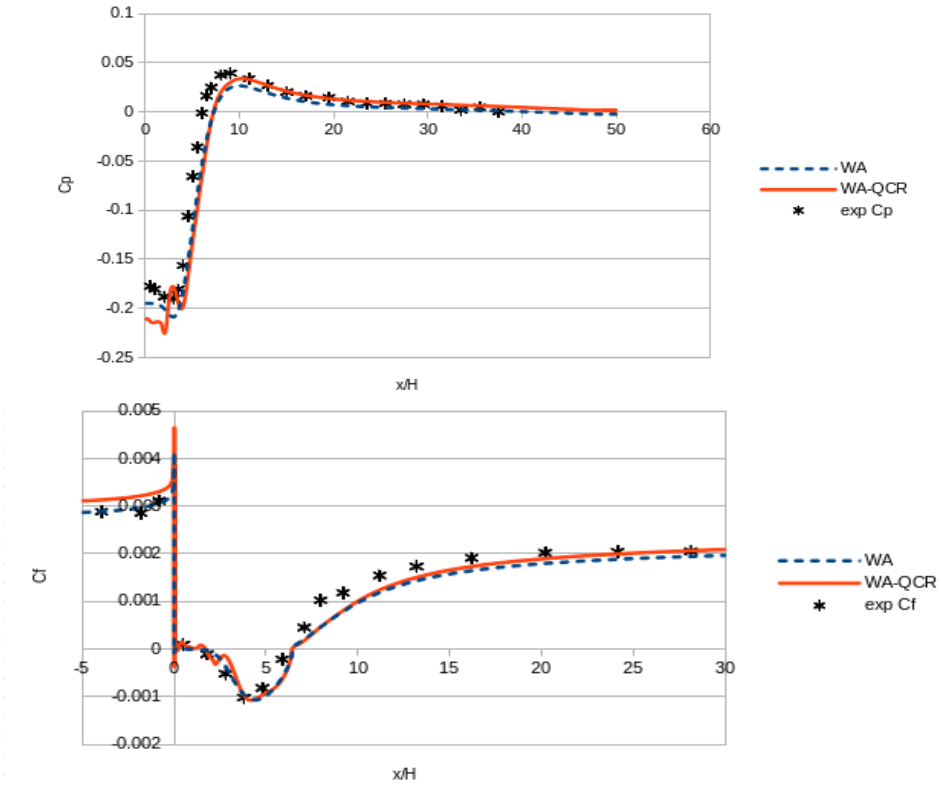

Figure 3.18: Cp and Cf from WA and WA-QCR models compared to experimental results [7]

3.2.4 Flow past a NACA 4412 Airfoil

Flow past a 2D NACA 4412 airfoil is also commonly used as a validation case. This test case has flow separation on the upper surface of the airfoil near the trailing edge. The simulations were run to match the flow conditions in the experiment of Coles and Wadcock [10]. The freestream velocity is M = 0.09 and the Reynolds number based on the chord and free stream velocity is Re_c=1.52 million, where chord c = 1. A 897x257 non-uniform mesh with strong clustering near the airfoil surface was used to find the grid independent numerical solutions.

Figures 3.19-3.21 show the comparison of experimental pressure coefficient [10] and the results computed with standard SA, SST k-ω and WA models, and SA-QCR, SST-QCR and WA-QCR models respectively. The figures indicate that there is no appreciable improvement with the application of QCR compared to the standard models. None of the models is able to compute the pressure near the trailing edge region of the airfoil correctly when compared to the experimental data.

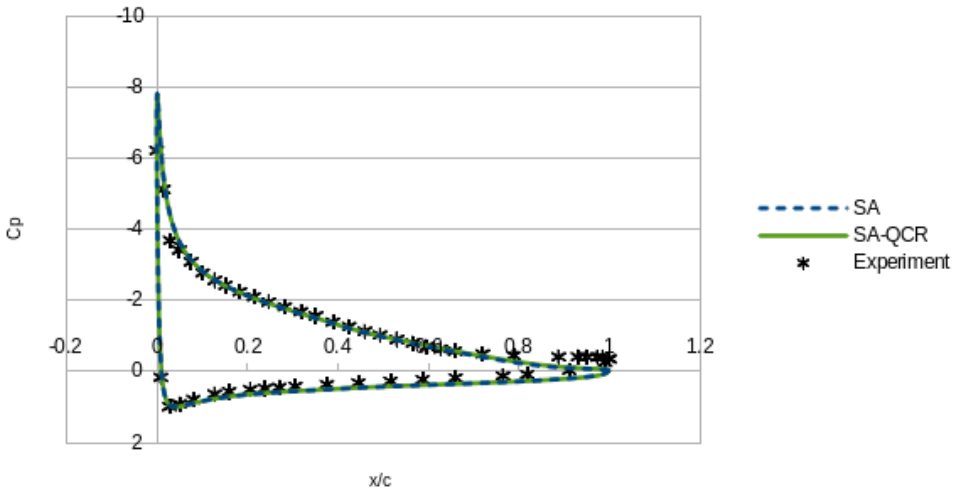

Figure 3.19: Cp results for SA and SA-QCR models compared to experimental values.

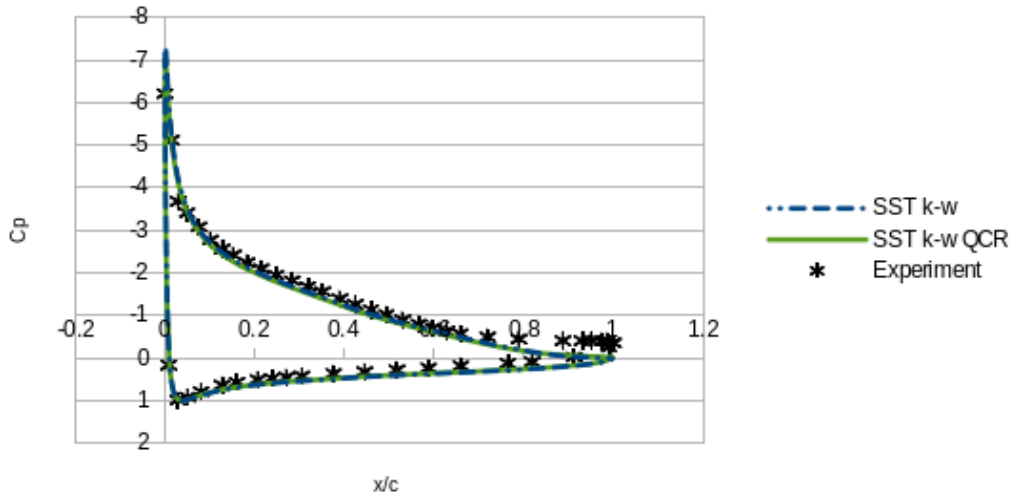

Figure 3.20: Cp results for SST and SST-QCR models compared to experimental values.

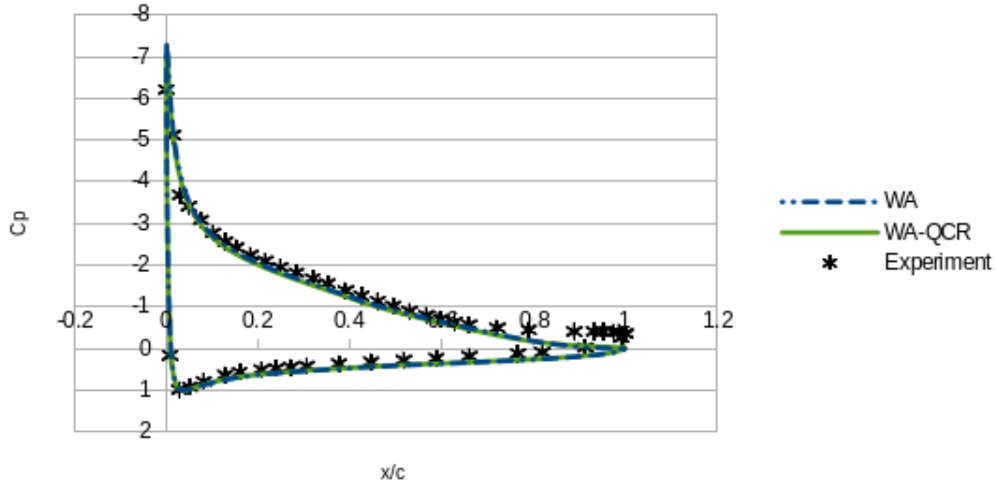

Figure 3.21: Cp results for WA and WA-QCR models compared to experimental values.

3.3 Compressible Wall-Bounded Separated Flows

3.3.1 Flow inside NASA Glenn S-Duct

S ducts are a very common component used in the propulsion system of an aircraft, both commercial and military. They serve to decelerate flow, increasing static pressure, and to provide a fairly uniform velocity and pressure distribution at the engine face. The curved shape and increasing cross-sectional area of the duct create secondary flows and boundary layer separation. It is anticipated that the addition of the QCR terms should have some effect to the result for this

case. Figure 3.22 shows the S duct computational domain as well as the cross section including grid structure.

Boundary conditions for this case were assigned to match the NASA Glenn experiment's flow conditions [11]. Walls were assigned a no-slip adiabatic condition with a plane of symmetry cutting down the y-axis at z equal to zero to save computation time. The inlet was treated as a "pressure inlet" with a total pressure and temperature matching the experimental conditions. The mass flow at the outlet was set to match the centerline Mach number of M = 0.6 at the reference inlet.

Figures 3.23-3.25 show the comparison of the calculated coefficient of pressure along the duct walls at three different circumferential angles (ϕ = 10^o, 90^o, and 170^o). The SA, SST k-ω, WA models and their QCR extensions are compared for each angle. The figures indicate that there is no appreciable improvement with the application of QCR compared to standard models. WA and WA-QCR results show the closest agreement with experimental results. The SA-QCR model seems to show the most improvement over the SA model.

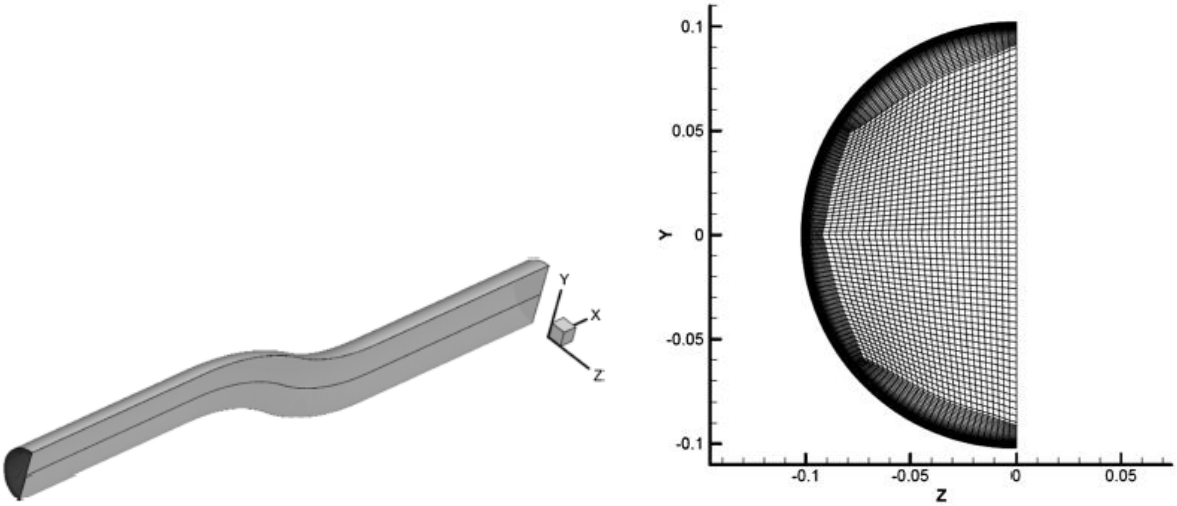

Figure 3.22 S-duct full view (left) and cross-section (right) with grid structure from Ref. [18].

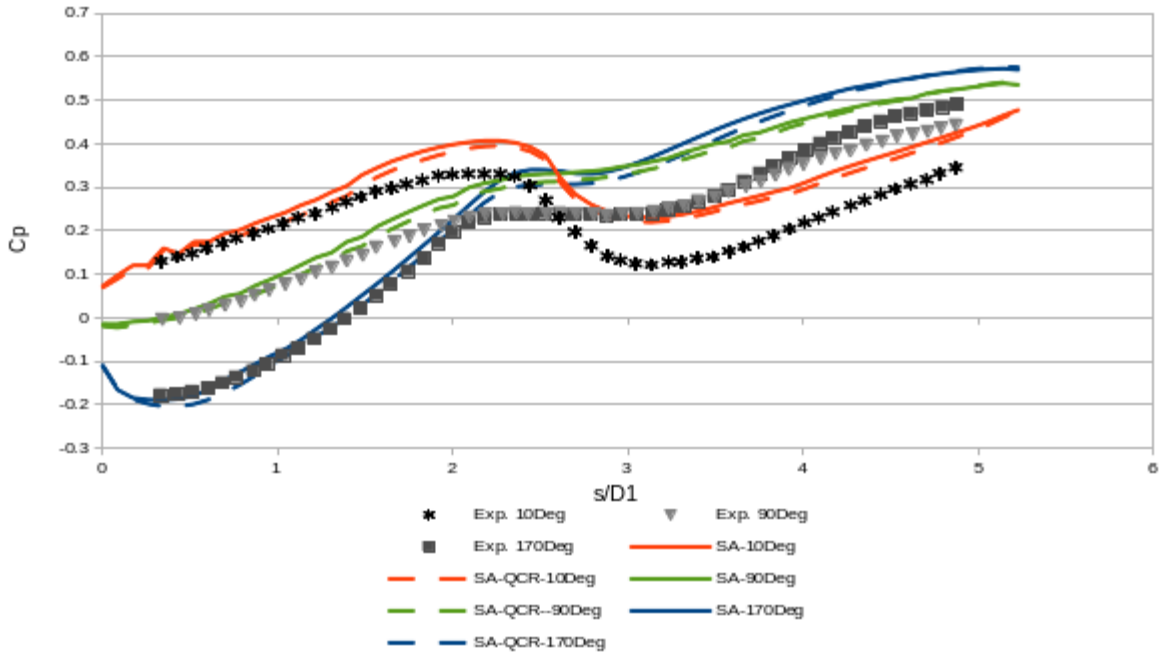

Figure 3.23: Experimental and computed Cp using SA and SA-QCR model along the duct walls at ϕ = 10º, 90º, and 170º

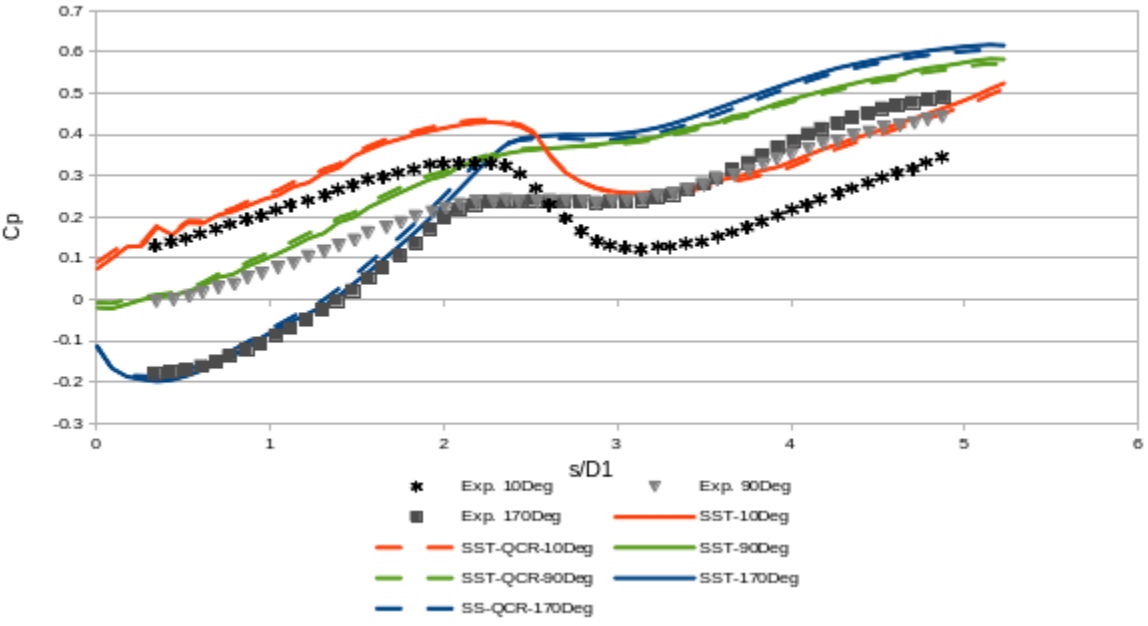

Figure 3.24: Experimental and computed Cp using SST and SST-QCR model along the duct walls at ϕ = 10º, 90º, and 170º

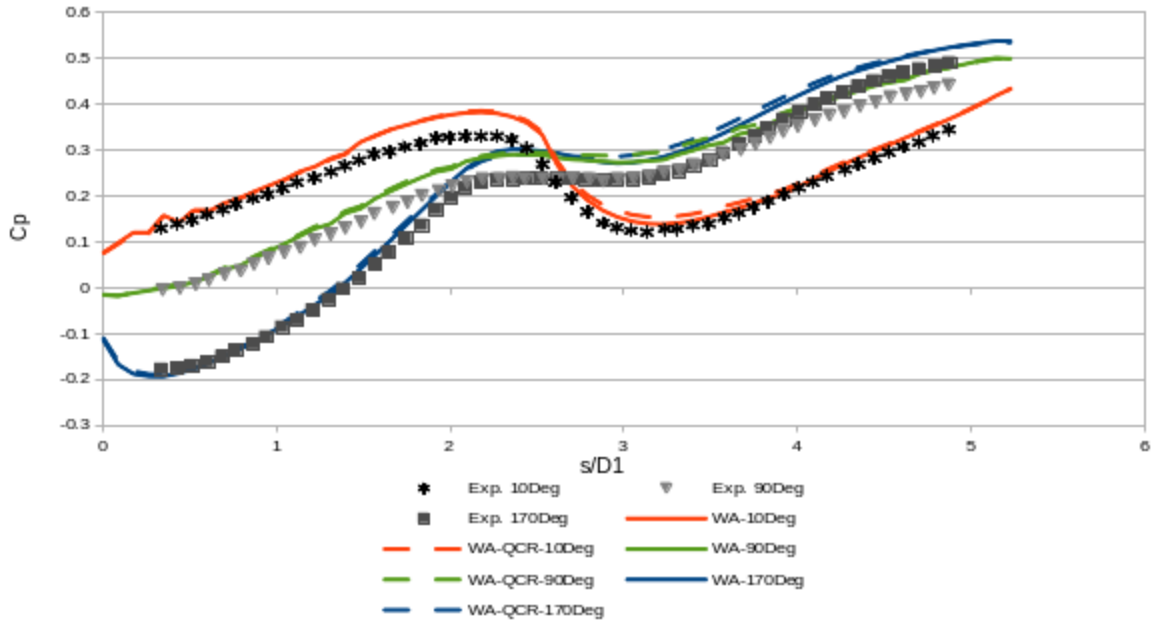

Figure 3.25: Experimental and computed Cp using WA and WA-QCR model along the duct walls at ϕ = 10º, 90º, and 170º

3.3.2 Supersonic Flow in a Square Duct

Computation of supersonic flow in a square duct necessarily requires a compressible flow solver in contrast to the previous test cases. The numerical simulation for this case was run to match the flow conditions in the experiment of Davis and Gessner taken from NASA TMR [7]. The duct has a square cross-section of each side D = 25.4mm and a length x/D = 50. Figure 3.26 shows the duct along with its cross section including the non-uniform mesh. A quarter of the duct size was employed in the simulation because of symmetry. The solid walls of the duct are adiabatic with no slip. The upstream velocity is M = 3.9 and the Reynolds number based on D and upstream velocity is Re_D= 508,000 with a reference temperature T = 520 R.

Figures 3.27-3.29 show the comparison of dimensionless velocity profile, u/u_{CL} (where u_{CL} is the centerline velocity) at cross section x/D = 40 with computed velocity profiles using the SA and

SA-QCR, SST and SST-QCR, and WA and WA-QCR models respectively. It can be seen that QCR models show significant improvement over the results from standard models.

Figures 3.30-3.32 show contour plots of secondary flow at *x/D*=50 using the SA and SA-QCR, SST and SST-QCR, and WA and WA-QCR models respectively. These plots were created using the following equation:

$$\sqrt{v^2 + w^2}/u_{CL} \tag{3.9}$$

where *v* is the y-component of velocity and *w* is the z-component of velocity. For each turbulence model, it can be seen that the standard models did not develop secondary flow; however the QCR models developed secondary flows. This test case clearly demonstrates the strengths of QCR models.

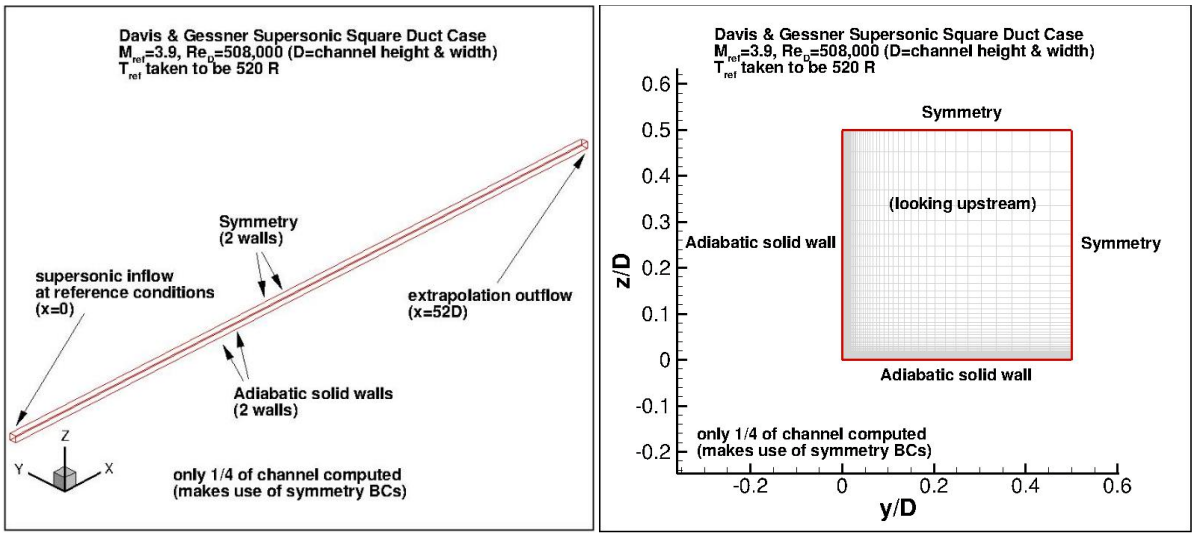

Figure 3.26: Square Duct full view (left) and square cross-section (right) with boundary conditions [7].

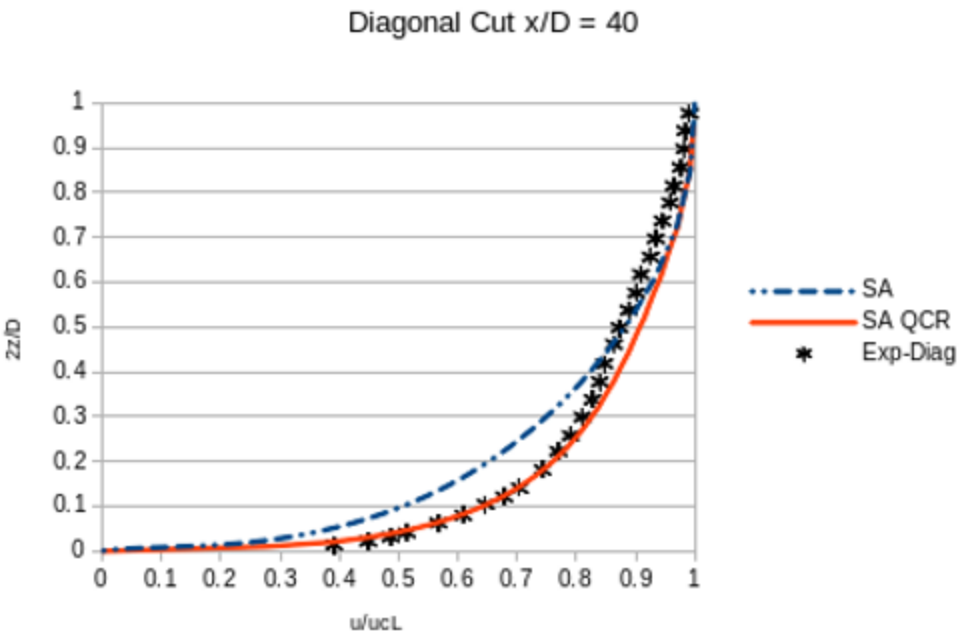

Figure 3.27: Experimental and computed dimensionless velocity profile using SA and SA-QCR model across the diagonal from corner to the center of the duct at x/D = 40.

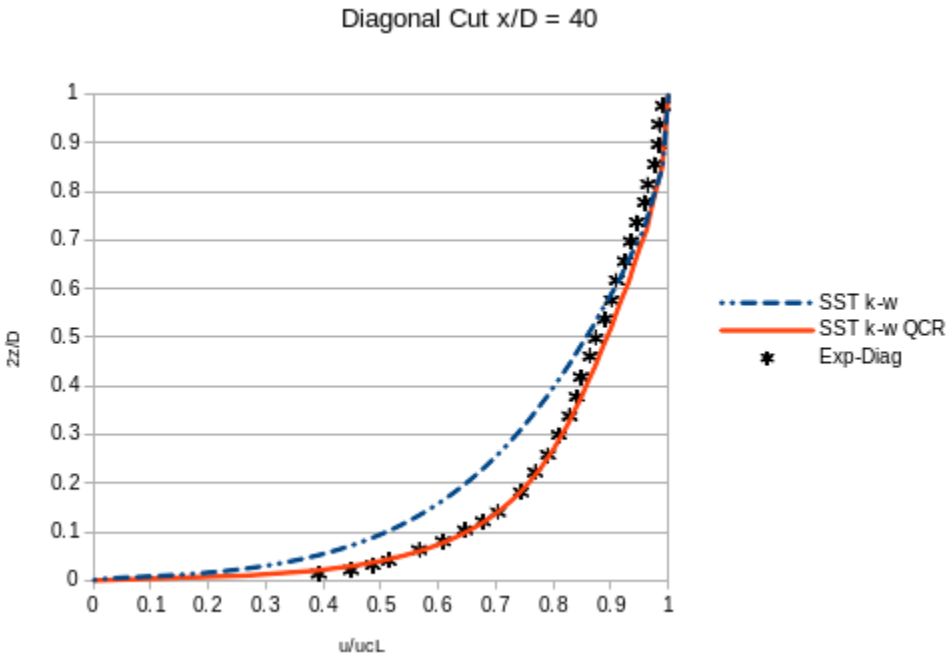

Figure 3.28: Experimental and computed dimensionless velocity profile using SST and SST-QCR model across the diagonal from corner to the center of the duct at x/D = 40.

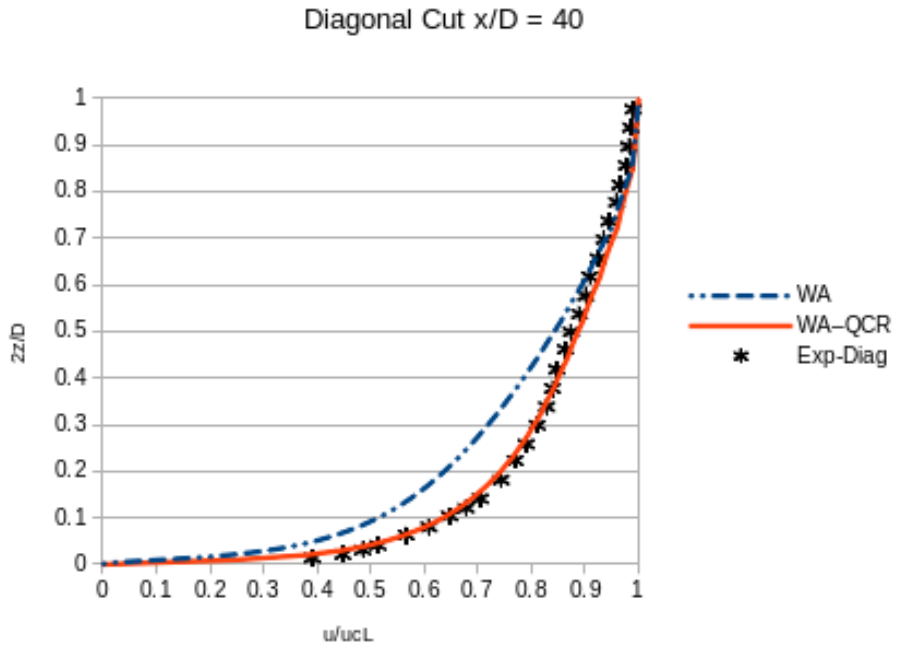

Figure 3.29: Experimental and computed dimensionless velocity profile using WA and WA-QCR model across the diagonal from corner to the center of the duct at x/D = 40.

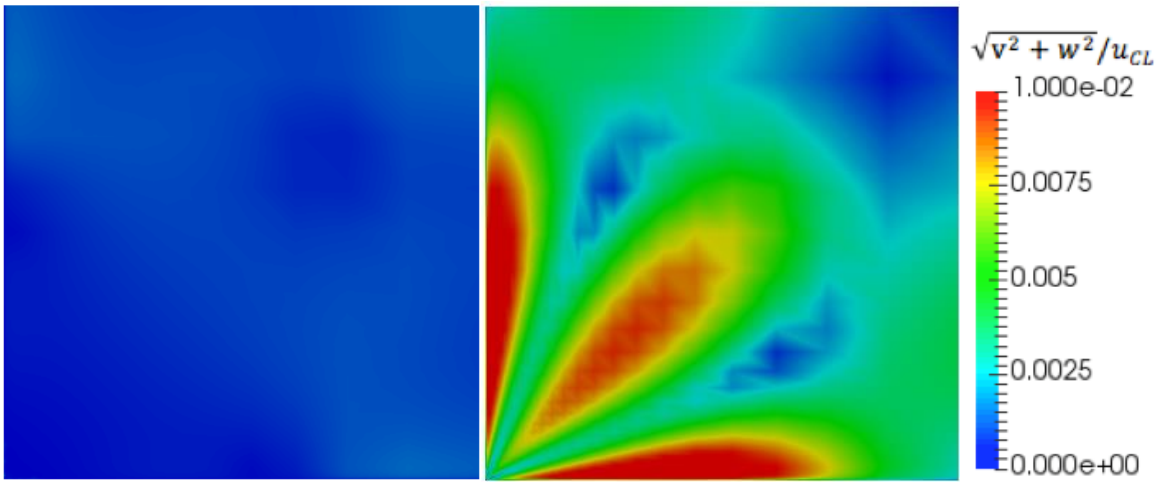

Figure 3.30: Contour plots of secondary flow at x/D=50 using SA (left) and SA-QCR (right) models

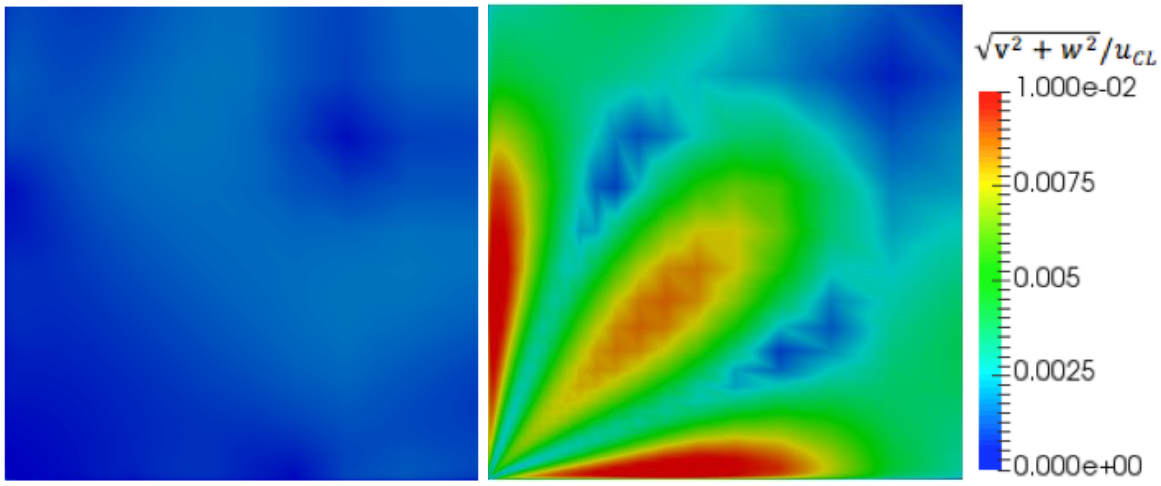

Figure 3.31: Contour plots of secondary flow at x/D=50 using SST (left) and SST-QCR (right) models

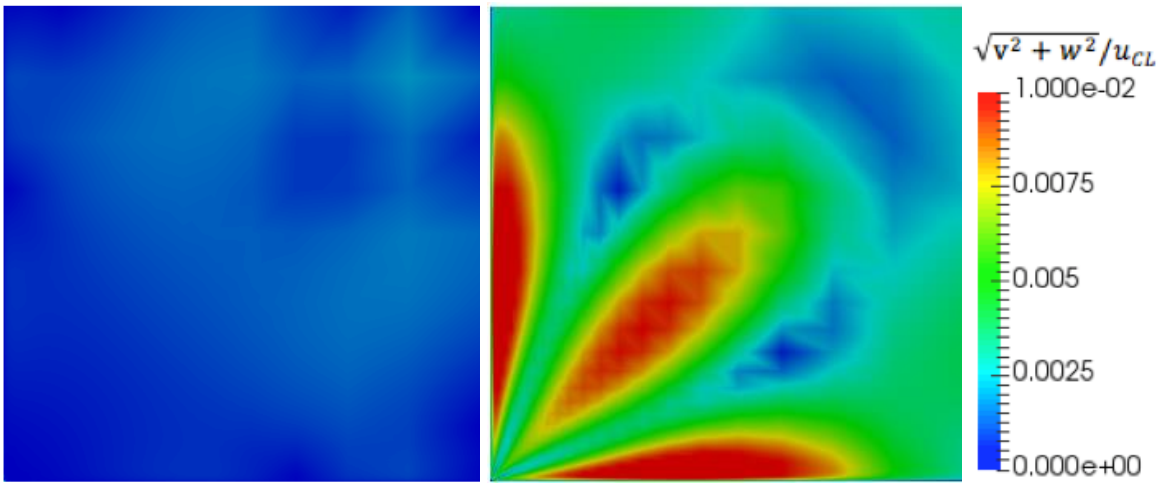

Figure 3.32: Contour plots of secondary flow at x/D=50 using WA (left) and WA-QCR (right) models

3.3.3 Flow due to a 2D Impinging Shock

This test case investigated a 2D impinging shock boundary layer interaction with a Mach angle of β = 14°. It is anticipated that QCR should have some effect on the interactive flow field of an incident oblique shock with a turbulent boundary layer. The flow and boundary conditions were set to match the experiment by Schulein et al [12]. The inlet was treated as a "pressure inlet" with a total pressure P_0 = 2.12 MPa and total temperature T_0 = 410 K. Wall temperature was kept at a constant T_w = 300 K. The pressure driven flow has an inlet Mach number M = 5. The outlet was

set to have zero gradient pressure, velocity and temperature. Figure 3.33 shows the computational domain with labeled boundary conditions.

Pressure ratio values at the bottom wall divided by the inlet pressure were measured before and after the location of the shock interaction with the boundary layer. This interaction forms a separation bubble. Figures 3.34 and 3.35 give the pressure ratio values for SA and WA models, along with their QCR extensions respectively compared to the experimental values taken from Schulein et al [12]. It can be seen that the WA model results agree better with the experimental results compared to the SA model. There is no appreciable improvement with the application of QCR compared to the standard models without QCR.

Three vertical sections were used to plot the velocity profiles along the y-axis of the flow field. These sections are labeled as sections 7, 8 and 9. Section 7 is measured velocity vertically at x = 376 mm up to y = 5.1 mm. Section 8 is measured velocity vertically at x = 396 mm up to y = 10.1 mm. Section 9 measured velocity vertically at x = 426 mm up to y = 7.1 mm. These specific locations were chosen to compare the computed velocity profiles with the experimental results. Figures 3.36-3.38 are the numerical results for SA, WA, SA-QCR, and WA-QCR models for sections 7-9. There is no appreciable improvement with application of QCR compared to the standard models.

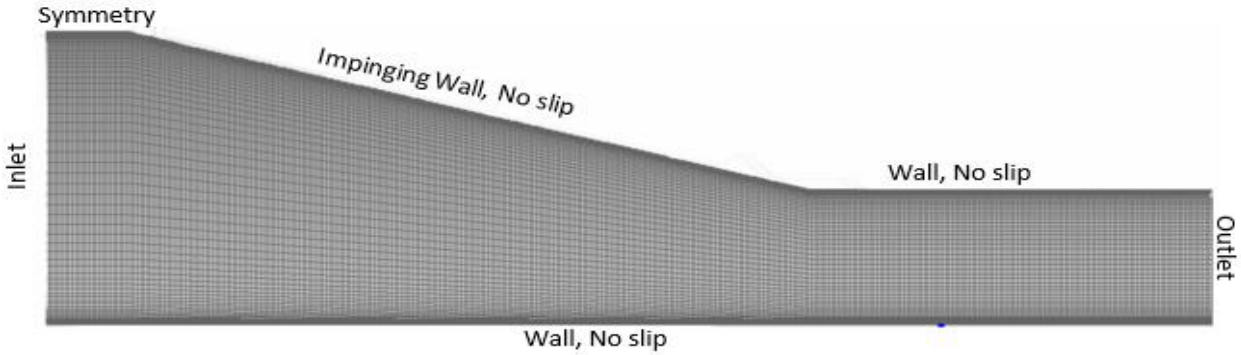

Figure 3.33: Computational domain and boundary conditions for simulation of a 2D shock impinging on a turbulent boundary layer

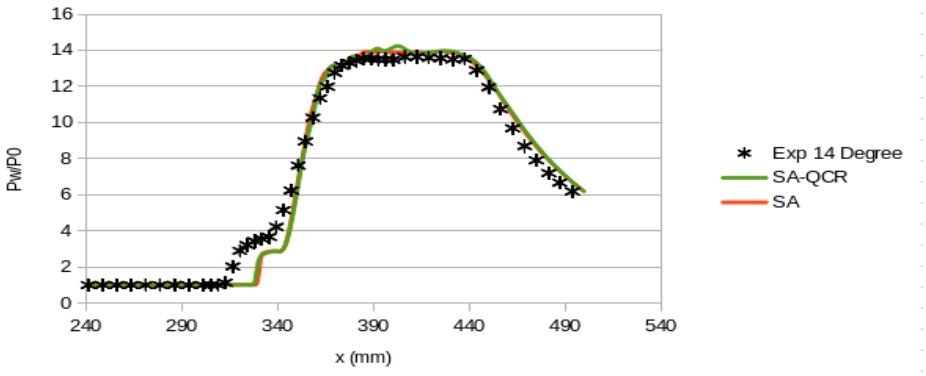

Figure 3.34: Wall pressure over inlet pressure ratio of SA and SA-QCR models compared to experimental values

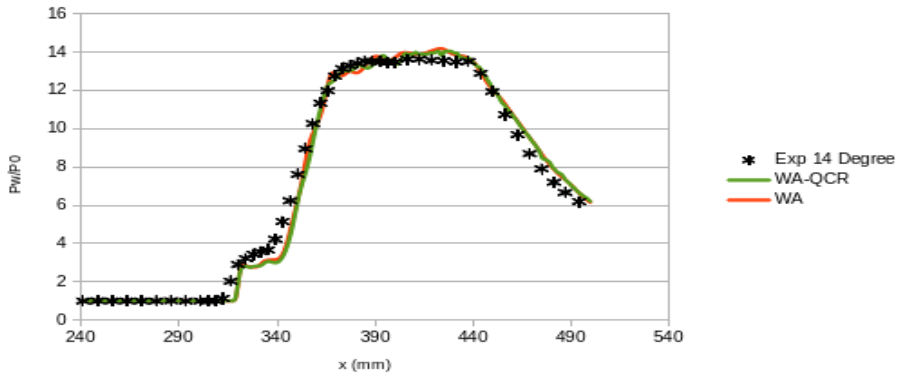

Figure 3.35: Wall pressure over inlet pressure ratio of WA and WA-QCR models compared to experimental values

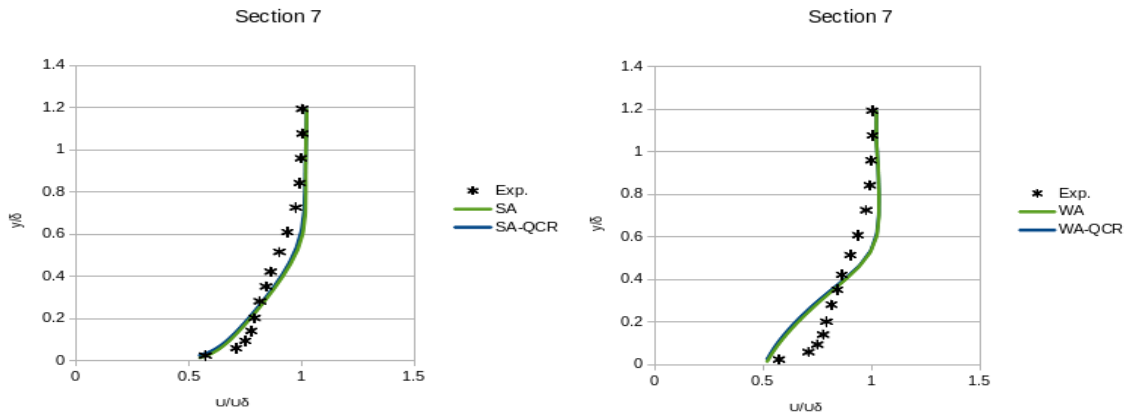

Figure 3.36: Velocity profiles at section 7 for SA and SA-QCR models (left), and WA and WA-QCR models (right)

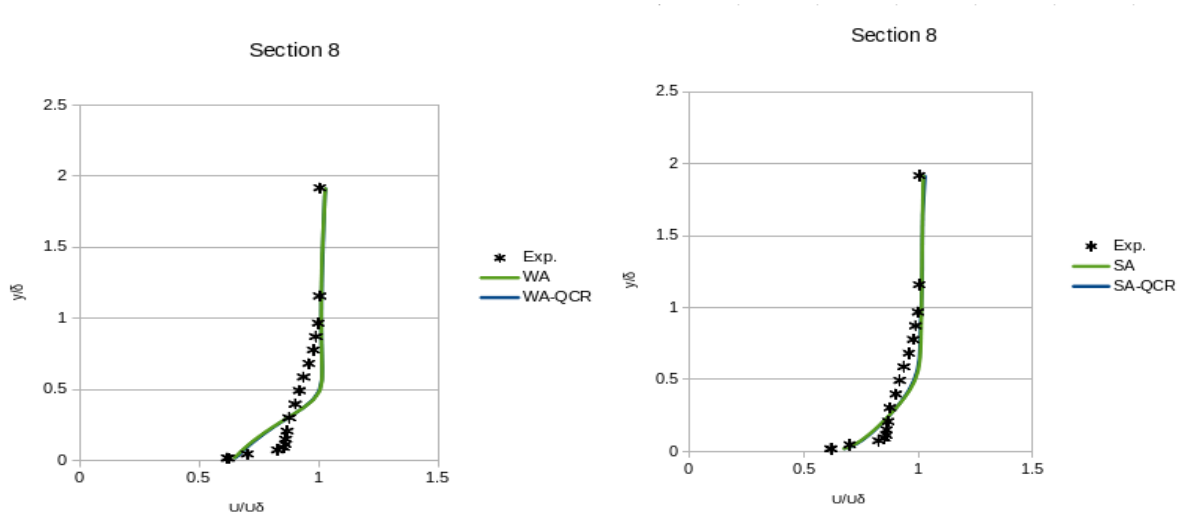

Figure 3.37: Velocity profiles at section 8 for SA and SA-QCR models (left), and WA and WA-QCR models (right)

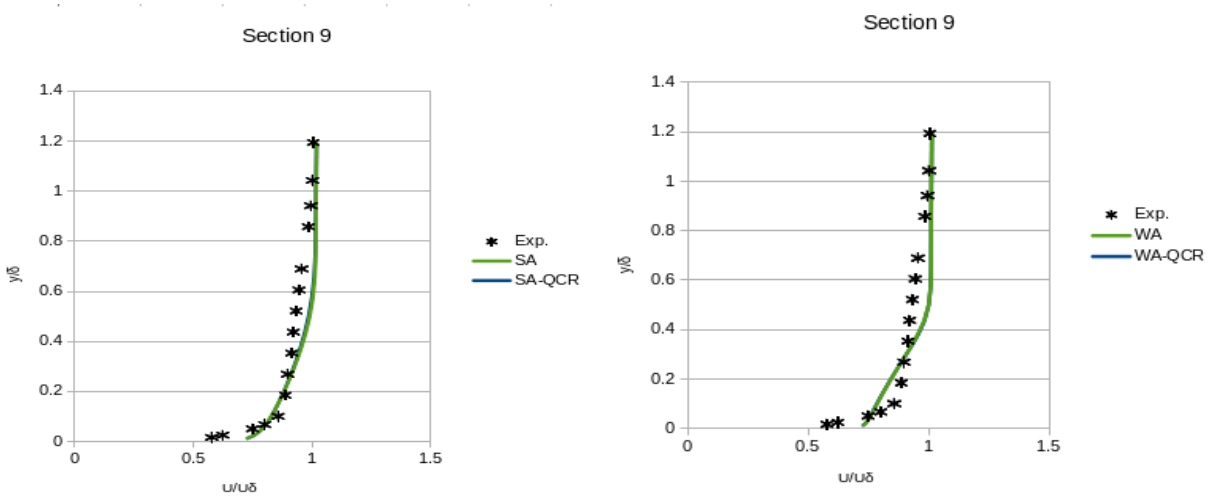

Figure 3.38: Velocity profiles at section 9 for SA and SA-QCR models (left), and WA and WA-QCR models (right)

3.3.4 Flow due to 3D Oblique Shock Boundary Layer Interaction

There are very few test cases where QCR has been shown to improve results drastically over the standard linear eddy viscosity relation. So far, QCR effects have been most evident in supersonic compressible flow cases with strong flow interactions with the boundary layer. A 3-D shock boundary layer interaction is an excellent case to show the significant effect of QCR terms on shock boundary layer interaction of an incident oblique shock with a turbulent boundary layer. Simulations by Benek et al. [13] have already shown some of the effects of the QCR terms on 3D shock/ boundary layer interactions.

Benek et al. ran three different run lengths with three different mesh widths at Mach numbers of 2.5, 2.7 and 2.9 each with three different oblique shock angles. Figure 3.39 and 3.40 show their computational domains for different run lengths. Figures 3.41 and 3.42 show the results of one of the many tests they ran; they show the streamlines of the flow near the bottom boundary of the computational domain, which show significant secondary flow effects with the QCR terms. Figures 3.43 and 3.44 show the numerical results obtained using the WA model with and without the QCR terms respectively. These figures exhibit similar results as seen by the simulations of

Benek et al. WA-QCR develops secondary flow patterns similar to what was seen in Fig. 3.41 with SST-QCR. This demonstrates that the QCR terms do have some significant effect in supersonic compressible flow with strong flow interactions with the boundary layer.

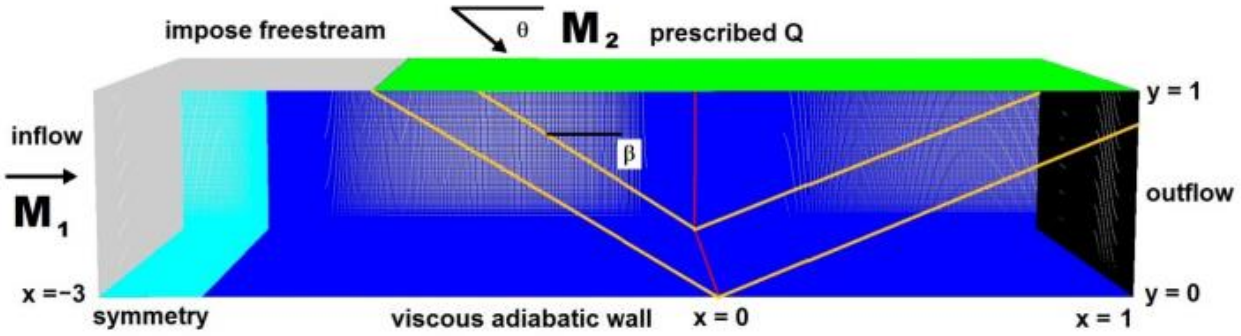

Figure 3.39: Computational Domain for 2.5 m run length

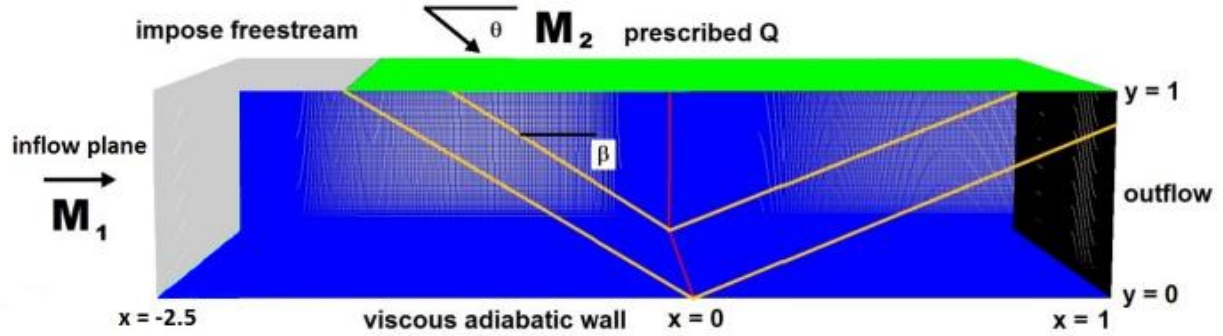

Figure 3.40: Computational Domain for 4.0 m and 5.5 m run lengths.

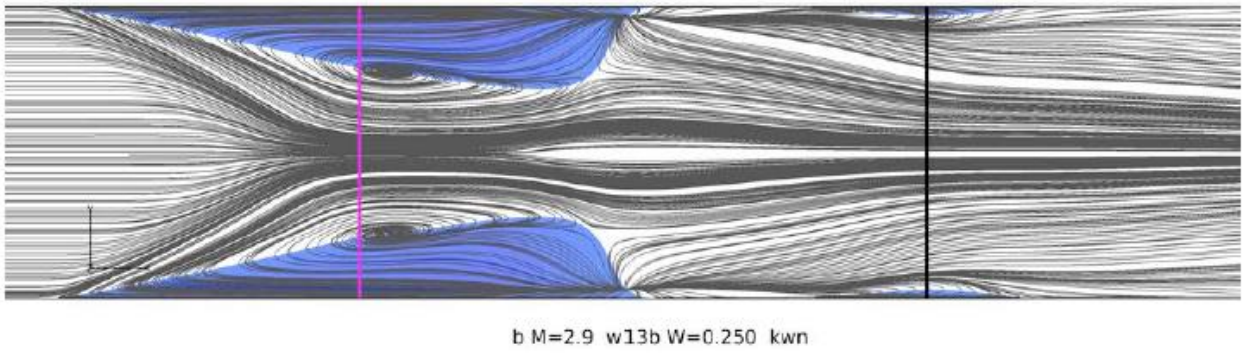

Figure 3.41: Floor flow streamlines at Mach = 2.9, wedge angle = 13^0, width = 0.25, run length of 5.5 m, with no QCR terms SST *k-ω* model

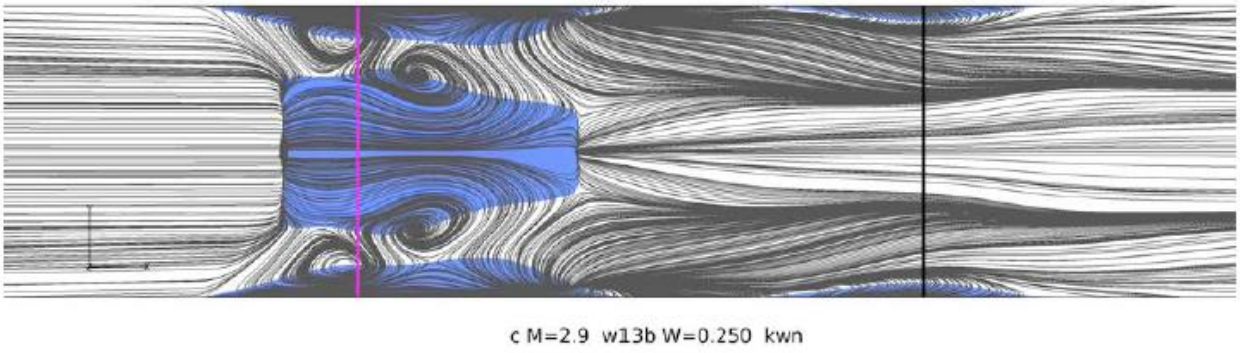

Figure 3.42 Floor flow streamlines at Mach = 2.9, wedge angle = 13º, width = 0.25, run length of 5.5 m with QCR terms in SST *k-ω* model

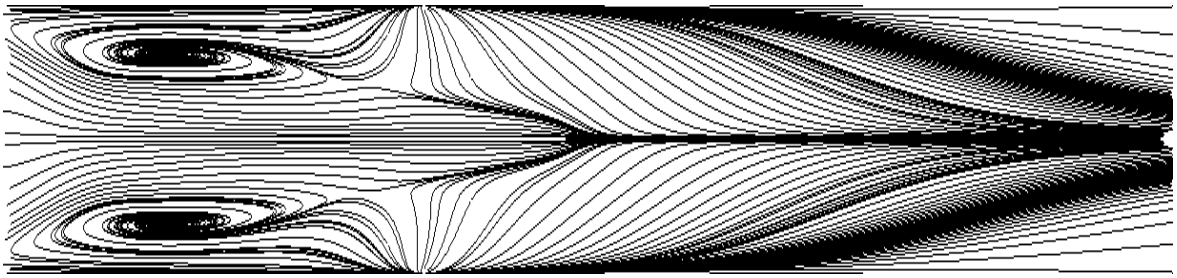

Figure 3.43: Floor flow streamlines at Mach = 2.9, wedge angle = 13º, width = 0.25, run length of 5.5 m, with no QCR terms in WA model

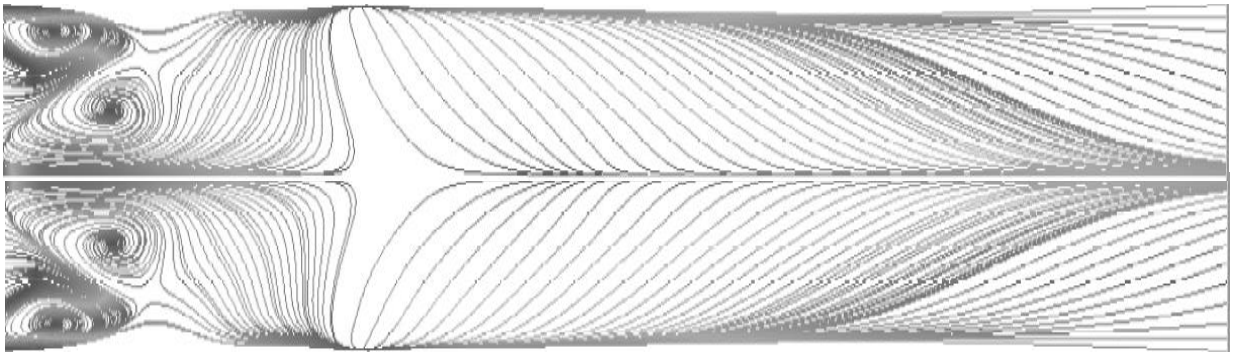

Figure 3.44: Floor flow streamlines at Mach = 2.9, wedge angle = 13º, width = 0.25, run length of 5.5 m with QCR terms in WA model

Chapter 4: Laminar-Turbulence Transition

4.1 Derivation of the WA-γ Transition model

The Wray-Agarwal (WA) model is a one-equation eddy-viscosity model derived from the k-ω closure [3]. An important distinction between the WA model and previous one-equation models based on k-ω closure is the inclusion of the cross diffusion term in the $R = k/\omega$ equation and a blending function, which allows smooth switching between the two destruction terms. The model determines $R = k/\omega$ by the following transport equation. This model alone cannot predict transition and is modified to include the correlation based intermittency equation γ, employing the local correlation-based transition-modelling concept. In this aspect, the modeling philosophy behind the two equations WA-γ model is similar to that of the four equations Shear-Stress Transport (SST) transition model of Menter et al. [14]. A newly formed wall-distance free version of the WA turbulence model [15] is used to create this transition model as detailed below.

In the wall-distance-free WA model [3,15], the eddy-viscosity is given by:

$$\nu_T = f_\mu R \tag{4.1}$$

The transport equation for R which includes the effect of γ in the production term is formulated as [16]:

$$\frac{\partial \rho R}{\partial t} + \frac{\partial \rho u_j R}{\partial x_j} = \frac{\partial}{\partial x_j}\left[(\mu + \sigma_R \mu_T)\frac{\partial R}{\partial x_j}\right] + \gamma \rho C_1 R S + \rho f_1 C_{2k\omega}\frac{\partial R}{\partial x_j}\frac{\partial S}{\partial x_j}\frac{R}{S} + P_R^{lim} - (1 - f_1)\rho C_{2k\epsilon}\min\left(\frac{R^2}{S^2}\frac{\partial S}{\partial x_j}\frac{\partial S}{\partial x_j}, Cm\frac{\partial R}{\partial x_j}\frac{\partial R}{\partial x_j}\right) \tag{4.2}$$

In Eq. (4.1), P_R^{lim} is used to ensure proper generation of R for very low values of turbulent intensity Tu. This term is formulated as:

$$P_R^{lim} = 1.5W \max(\gamma - 0.2, 0)\,(1.0 - \gamma) \min\left(\max\left(\frac{Re_v}{2420} - 1, 0\right), 3\right) \max(3v - v_t, 0) \tag{4.3}$$

Following [6], the intermittency transport equation can be written as:

$$\frac{\partial \rho\gamma}{\partial t} + \frac{\partial \rho u_j \gamma}{\partial x_j} = \frac{\partial}{\partial x_j}\left[\left(\mu + \frac{\mu_T}{\sigma_\gamma}\right)\frac{\partial \gamma}{\partial x_j}\right] + F_{length}\rho S\gamma(1-\gamma)F_{onset} - \rho c_{a2}\Omega\gamma F_{turb}(c_{e2}\gamma - 1) \tag{4.4}$$

In Eq. (4.4), F_{onset} is used to trigger the intermittency production and is a function of R_T, Re_v, and $Re_{\theta c}$ as given in the following equations:

$$F_{onset1} = \frac{Re_v}{2.2Re_{\theta c}},\ F_{onset2} = \min(F_{onset1},\ 2.0),\ F_{onset3} = max\left(1 - \left(\frac{R_T}{3.5}\right)^3,\ 0\right) \tag{4.5}$$

$$F_{onset} = \max(F_{onset2} - F_{onset3},\ 0) \tag{4.6}$$

$$F_{turb} = e^{-\left(\frac{R_T}{2}\right)},\ R_T = \frac{\mu_t}{\mu},\ Re_v = \frac{\rho d_w^2 S}{\mu} \tag{4.7}$$

The model constants for the intermittency equation are as follows [6]:

$$F_{length} = 100,\ c_{e2} = 50,\ c_{a2} = 0.06,\ \sigma_\gamma = 1.0 \tag{4.8}$$

The local turbulence intensity Tu_L is given by [16]:

$$Tu_L = min\left(100\,\frac{\sqrt{\frac{2R}{3}}}{\sqrt{\frac{S}{0.3}} * d_w},\ 100\right) \tag{4.9}$$

where d_w is the wall distance. In the original formulation of Tu_L obtained from Ref. [6], R replaces turbulent kinetic energy k (note that $R = k/\omega$) and ω in the original formulation is replaced by $\omega \approx S/0.3$.

The formula for the pressure gradient parameter can be written as [6]:

$$\lambda_{\theta L} = -7.57 \cdot 10^{-3} \frac{dV}{dy} \frac{d_w^2}{\nu} + 0.0128 \tag{4.10}$$

This term is bounded by -1.0 ≤ $\lambda_{\theta L}$ ≤ 1.0 for numerical robustness.

The $Re_{\theta c}$ correlation is given by [6]:

$$Re_{\theta c} = 100.0 + 1000.0 * \exp[-1.0 * Tu_L * F_{PG}] \tag{4.11}$$

where F_{PG} is a correlation function of $\lambda_{\theta L}$:

$$F_{PG} = \begin{cases} \min\left(1 + C_{PG1}\lambda_{\theta L}, C_{PG1}^{lim}\right), \ \lambda_{\theta L} \geq 0 \\ \min\left(1 + C_{PG2}\lambda_{\theta L} + C_{PG3}\min[\lambda_{\theta L} + 0.0681, 0], C_{PG2}^{lim}\right), \ \lambda_{\theta L} < 0 \end{cases} \tag{4.12}$$

$$C_{PG1} = 14.68, \ \ C_{PG2} = -7.34, \ \ C_{PG3} = 0.0 \tag{4.13}$$

$$C_{PG1}^{lim} = 1.5, \ \ C_{PG2}^{lim} = 3.0 \tag{4.14}$$

F_{PG} is limited in order to avoid negative values:

$$F_{PG} = \max(F_{PG}, 0) \tag{4.15}$$

The wall blocking effect is accounted for by the damping function f_μ.

$$f_\mu = \frac{\chi^3}{\chi^3 + C_w^3}, \chi = \frac{R}{\nu} \tag{4.16}$$

S is the mean strain given by

$$S = \sqrt{2S_{ij}S_{ij}}, \qquad S_{ij} = \frac{1}{2}\left(\frac{\partial u_i}{\partial x_j} + \frac{\partial u_j}{\partial x_i}\right) \tag{4.17}$$

W is the mean vorticity given by

$$W = \sqrt{2W_{ij}W_{ij}}, \ \ W_{ij} = \frac{1}{2}\left(\frac{\partial u_i}{\partial x_j} - \frac{\partial u_j}{\partial x_i}\right) \tag{4.18}$$

While the $C_{2k\omega}$ term is active, Eq. (4.2) behaves as a one-equation model based on the standard k-ω equations. The inclusion of the cross diffusion term in the derivation causes the additional $C_{2k\varepsilon}$ term to appear. This term corresponds to the destruction term in one equation models derived from the standard k-ε closure. The presence of both terms allows the WA model to behave as either a one-equation k-ω or one equation k-ε model based on the switching function f_1. The blending function was designed so that the k-ω destruction term is active near solid boundaries and the k-ε destruction term becomes active away from the wall near the end of the log-layer. This function was modified from the original Wray-Agarwal model to remove its dependence on the wall distance. The following equations describe the formulation of f_1 for wall distance free WA model [15].

$$f_1 = tanh(arg_1^4) \tag{4.19}$$

$$arg_1 = \frac{R + v}{2}\frac{\eta^2}{C_\mu k\omega} \tag{4.20}$$

$$k = \frac{v_T S}{\sqrt{C_\mu}}, \qquad \omega = \frac{S}{\sqrt{C_\mu}}, \qquad \eta = S * \max\left(1, \left|\frac{W}{S}\right|\right) \tag{4.21}$$

The model constants and equations for C_1, $C_{2k\omega}$, $C_{2k\varepsilon}$, and σ_R terms are described by the following equations:

$$C_1 = f_1(C_{1k\omega} - C_{1k\varepsilon}) + C_{1k\omega} \tag{4.22}$$

$$C_{2ke} = \frac{C_{1k\varepsilon}}{\kappa^2} + \sigma_{k\varepsilon} \tag{4.23}$$

$$C_{2k\omega} = \frac{C_{1k\omega}}{\kappa^2} + \sigma_{k\omega} \tag{4.24}$$

$$C_{1k\omega} = 0.0829, \qquad C_{1k\varepsilon} = 0.1284 \tag{4.25}$$

$$\sigma_R = f_1(\sigma_{k\omega} - \sigma_{k\varepsilon}) + \sigma_{k\varepsilon} \tag{4.26}$$

$$\sigma_{k\omega} = 0.72, \sigma_{k\varepsilon} = 1.0 \tag{4.27}$$

$$\kappa = 0.41,\ C_\omega = 8.54,\ C_m = 8.0 \tag{4.28}$$

4.2 Calibration of Correlations and Validation Cases

4.2.1 Zero-Pressure Gradient Flat Plate Flow

Computations were performed for the three zero pressure gradient flat plate cases (T3A, T3B, T3A-), which employ different free-stream velocities $U_\infty$and free-stream turbulence intensities Tu_∞as shown in Table 4.1. The mesh used in simulations of all three cases is the same as shown in Figure 4.1. The WA-γ model results are compared to the results from the four-equation SST-Transition model and the experimental data [17].

Table 4.1: Inlet flow conditions for T3 series flat plates

	U_∞ (m/s)	Tu_∞(%)	μ_T/μ	ρ (kg/m^3)	μ (kg/m.s)
T3A	5.4	3.5	13.3	1.2	1.8e-5
T3B	9.4	6.5	100	1.2	1.8e-5
T3A-	19.8	0.874	8.72	1.2	1.8e-5

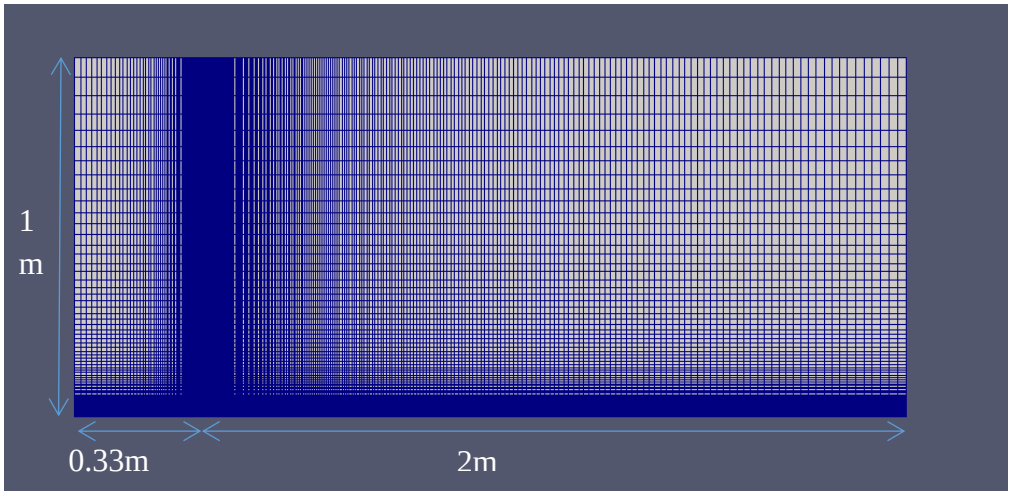

Figure 4.1: Grid in the computational domain for flow over T3 series flat plates.

Skin friction results for the three T3A, T3B and T3- flat plate cases are shown in Figs. 4.2 – 4.4. As shown in these figures, the computed results for the WA-γ model for all three flat plate cases

are in good agreement with the experimental data and outperform the results from the four-equation SST-Transition model.

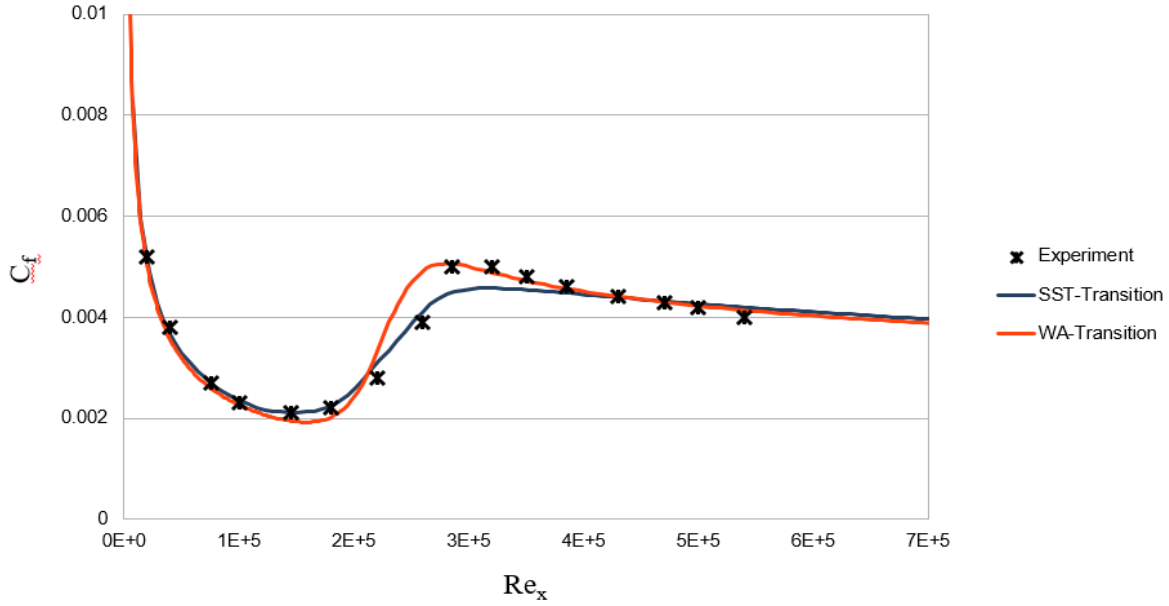

Figure 4.2: T3A Flat Plate results

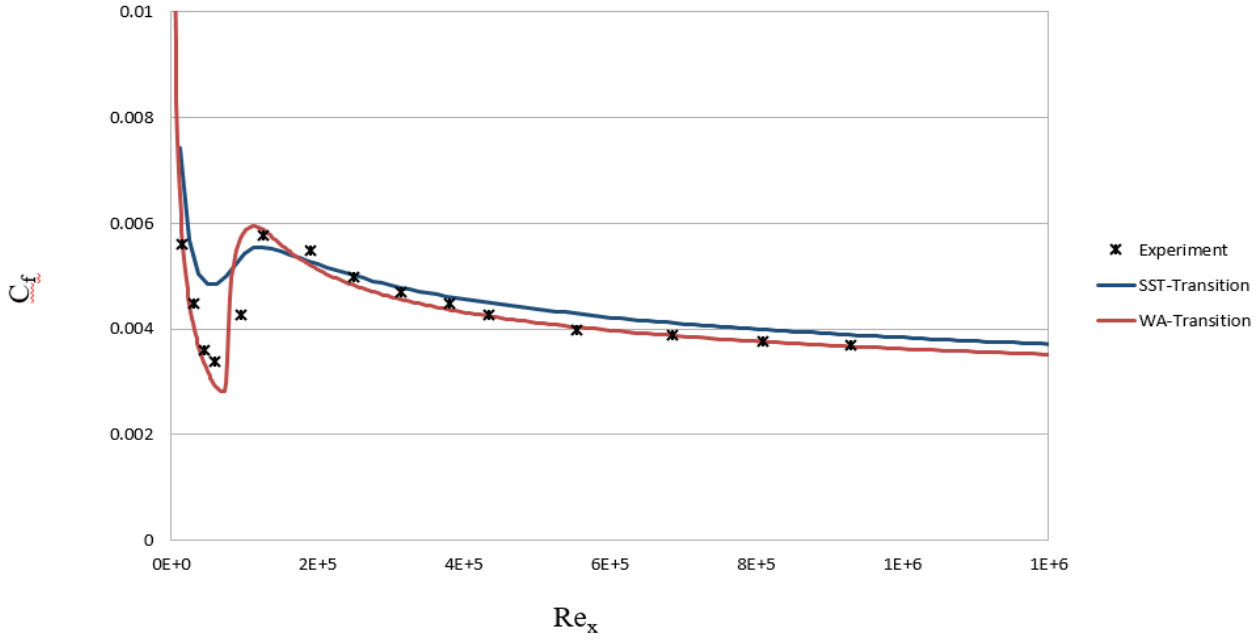

Figure 4.3: T3B Flat Plate results

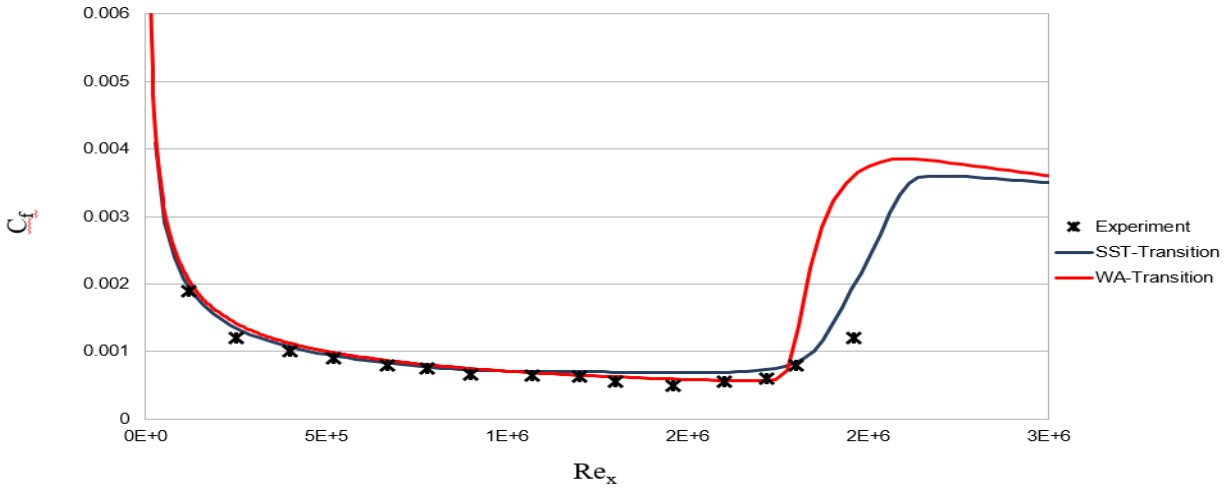

Figure 4.4: T3A- Flat Plate results

4.2.2 Non-Zero-Pressure Gradient Flat Plate Flow

The ERCOFTAC test cases T3C2-5 [17] take into account the effects of pressure gradient and free-stream turbulence decay on transition prediction. A non-zero pressure gradient effect in the simulations was achieved by using the polynomial expressions from Suluskna et al [18] to modify the shape of the duct upper boundary. T3C4 was the only case that required a different shape. The polynomial expression for the domain width as a function of x for the T3C cases is expressed by Eq. (4.29), and the domain width for T3C4 is expressed by Eq. (4.30) as follows:

$$\frac{h}{D} = \min(1.231\mathrm{x}^6 - 6.705x^5 + 14.061x^4 - 14.113x^3 + 7.109x^2 - 1.9x + 0.95, 1.0) \quad (4.29)$$

$$\frac{h}{D} = \min(1356\mathrm{x}^6 - 7.591x^5 + 16.513x^4 - 17.510x^3 + 9.486x^2 - 2.657x + 0.991, 1.0) \quad (4.30)$$

In Eq. (4.29) and Eq. (4.30), h is the upper boundary height, D is the inlet height (0.3m), and x is distance along the plate from the leading edge. Each T3C case uses different free-stream velocity U_∞ and free-stream turbulence intensity Tu_∞ as shown in Table 4.2.

Table 4.2: Inlet flow conditions for T3C series of flat plates

	U_∞ (m/s)	Tu_∞(%)	μ_T/μ	ρ (kg/m^3)	μ (kg/ms)
T3C2	5.0	3.10	9.0	1.2	1.8e-5
T3C3	3.7	3.10	6.0	1.2	1.8e-5
T3C4	1.28	3.10	2.5	1.2	1.8e-5
T3C5	8.4	3.70	15	1.2	1.8e-5

Skin friction results for the T3C flat plate cases given in Table 4.2 are shown in Figs. 4.5-4.8. The computed results from the WA-γ model for all four T3C flat plate cases are in reasonably good agreement with the experimental values [17].

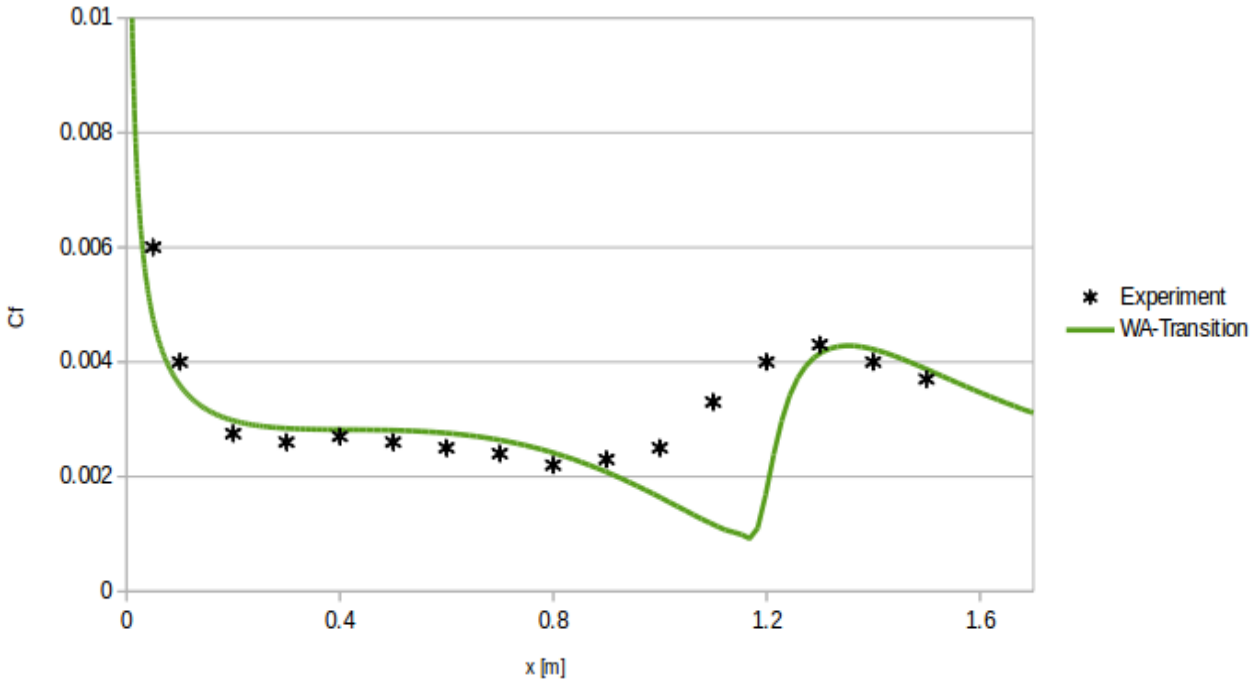

Figure 4.5: T3C2 Flat Plate results

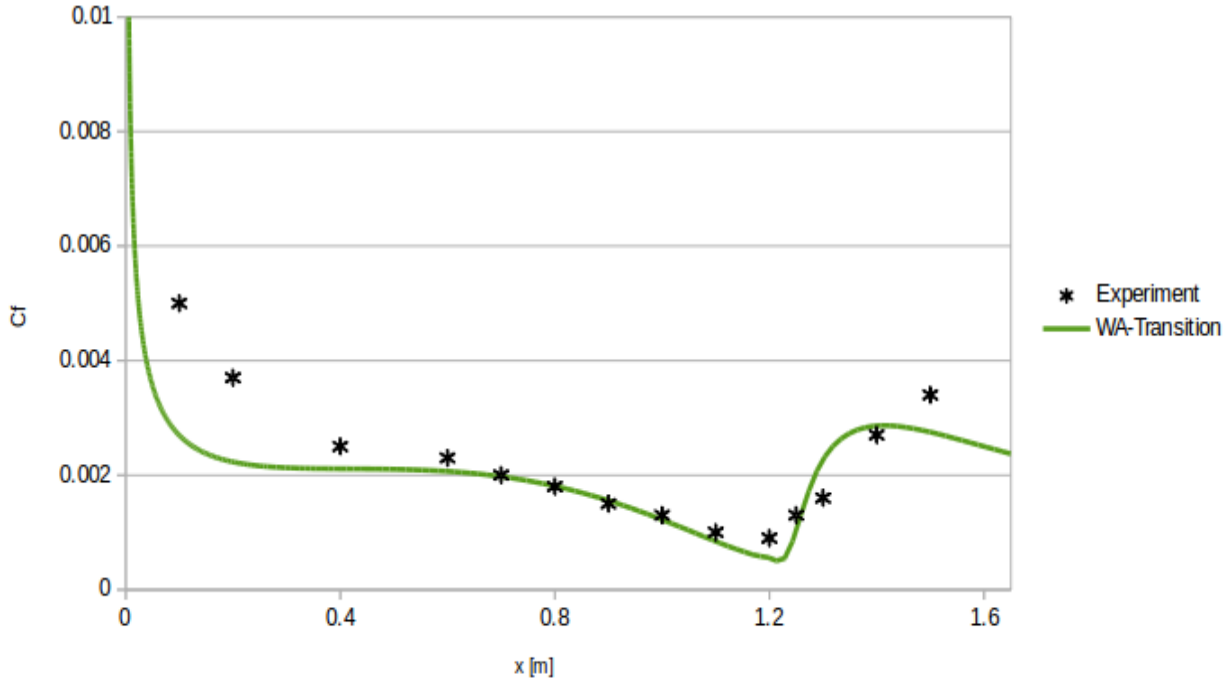

Figure 4.6: T3C3 Flat Plate results

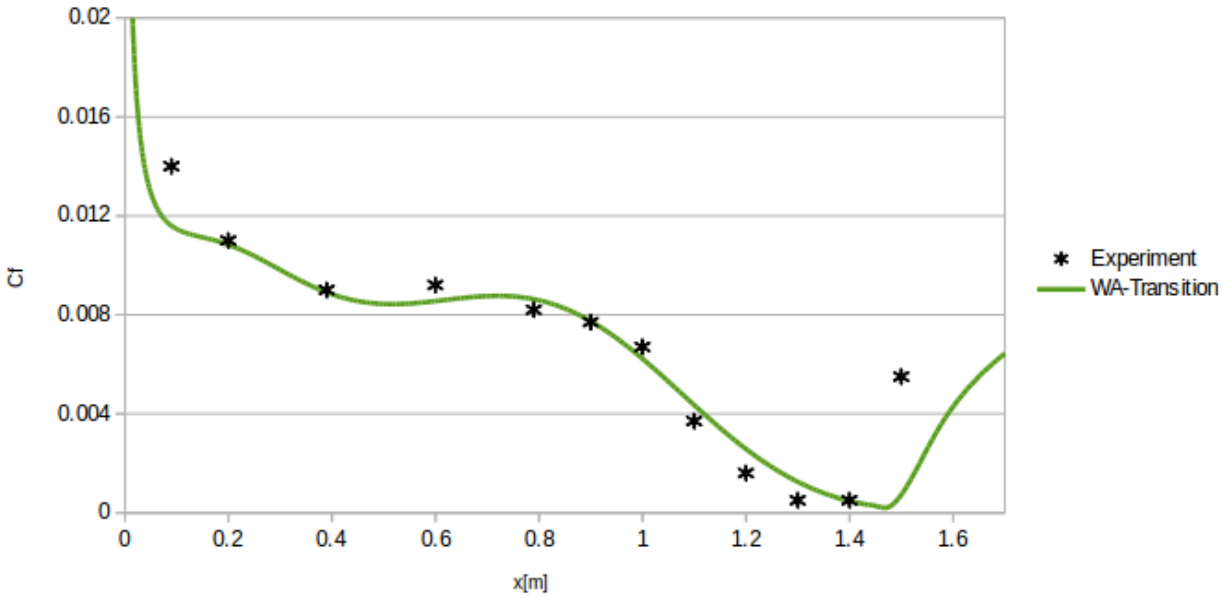

Figure 4.7: T3C4 Flat Plate results

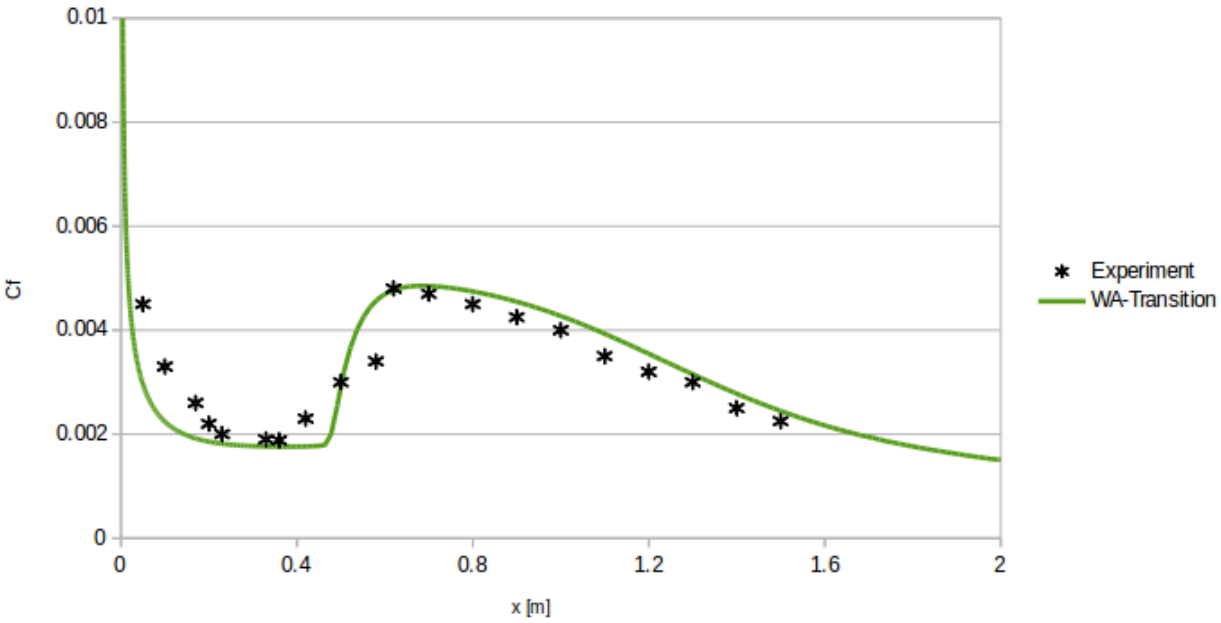

Figure 4.8: T3C5 Flat Plate results

4.3 Application Test Cases

4.3.1 S809 Airfoil

The S809 airfoil is a "laminar flow" airfoil designed for wind turbines, with a 21% thick chord [19]. The airfoil is designed for typical wind energy applications at Mach 0.1 flow that can have laminar flow up to 50% chord length on both the upper and lower surfaces. Computations were performed at three angles of attack $\alpha = 0°, 5°,$ and $10°$ at Reynolds number = 2 x 10^6. For all angles of attack, the free stream turbulence intensity was $Tu_\infty = 0.2\%$ with a viscosity ratio of $\frac{\nu_t}{\nu} = 10$ in the computations. A very fine C-mesh was used with high clustering near the airfoil surface to guarantee a y+ of less than one on all parts of the airfoil.

Figures 4.9-4.11 show numerical results for the coefficient of pressure on the airfoil surface using the WA-γ transition model. These results are compared to the experimental data and the SST-Transition and SST k-ω turbulence model results. For every angle of attack computed, the WA-γ

transition model performs at least as well as the four-equation SST transition model and as expected both transition models outperform the fully turbulent SST k-ω model.

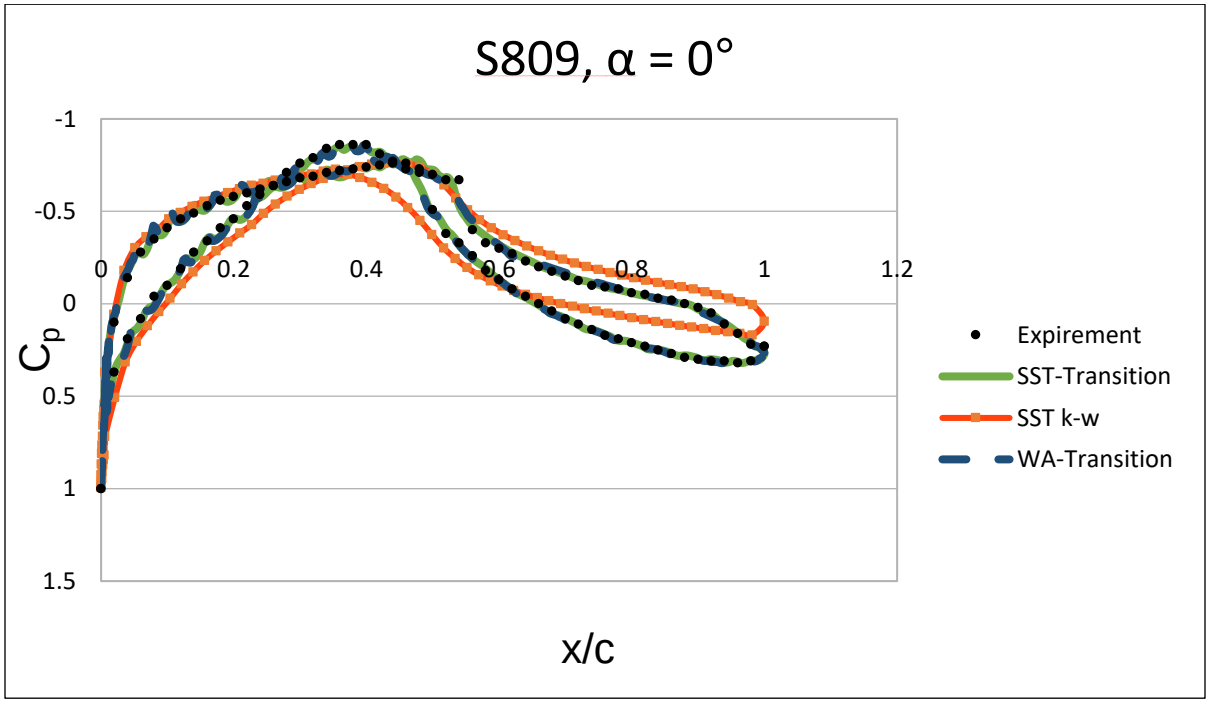

Figure 4.9: Pressure coefficient on S809 airfoil at α = 0°

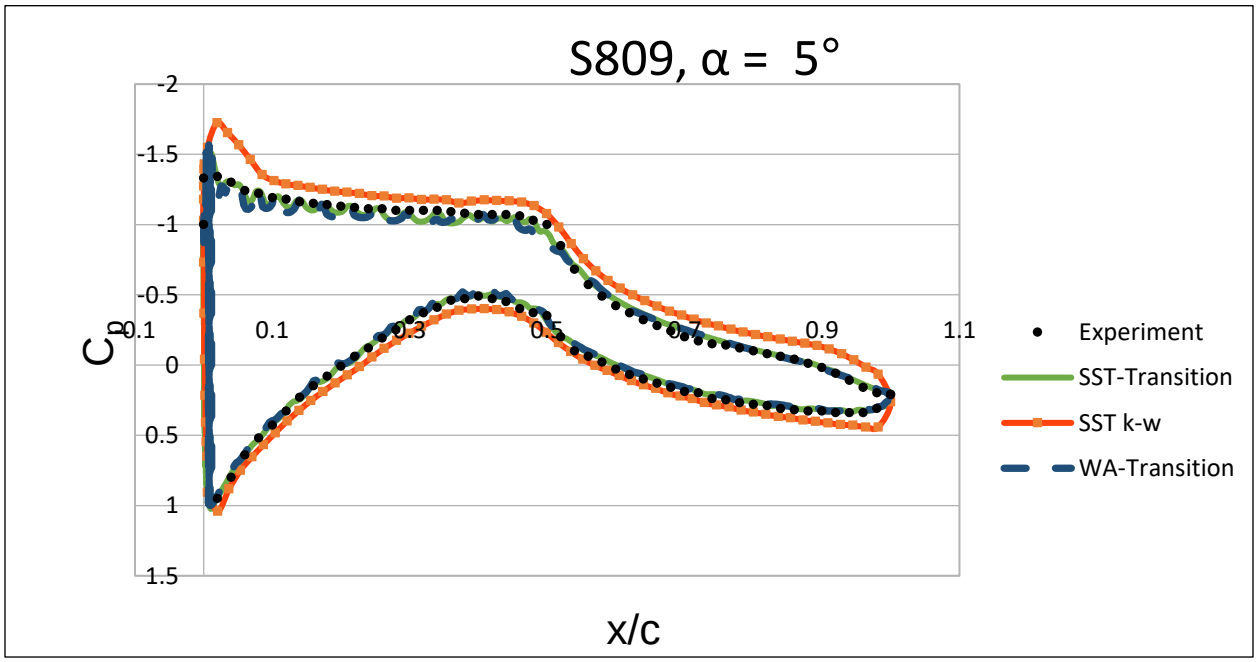

Figure 4.10: Pressure coefficient on S809 airfoil at α = 5°

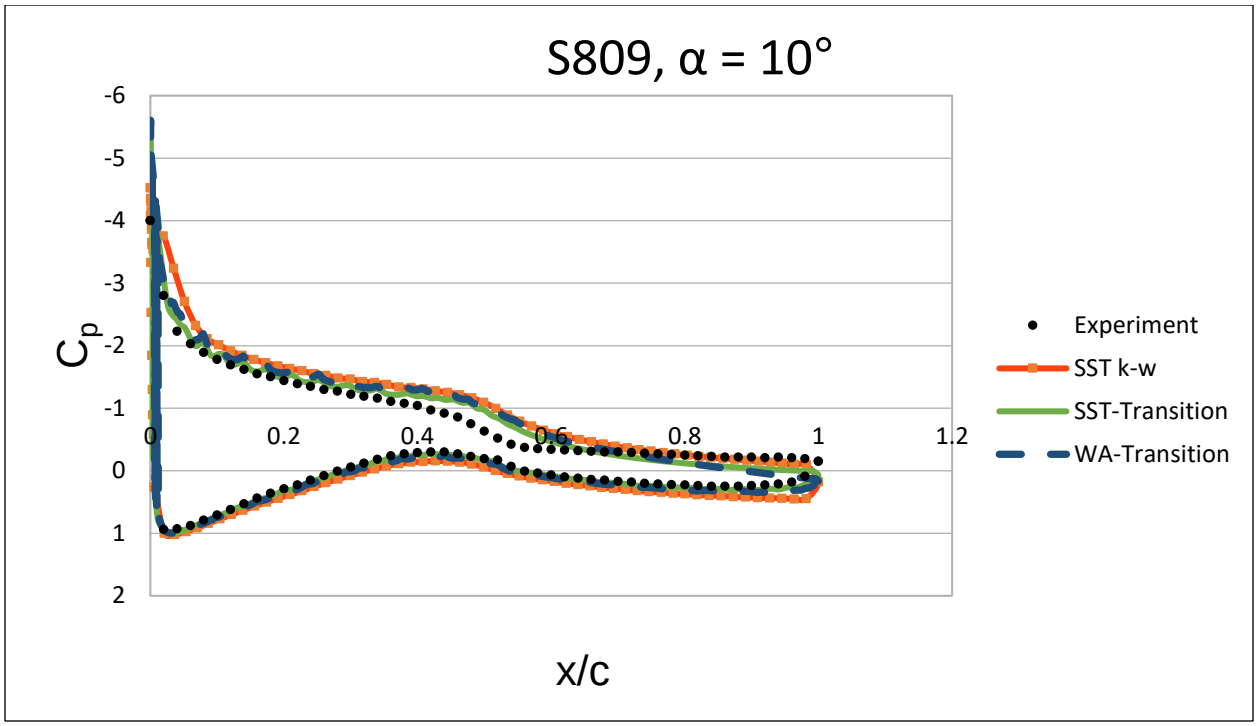

Figure 4.11: Pressure coefficient on S809 airfoil at α = 10°

4.3.2 Aerospatiale-A Airfoil

The Aerospatiale-A airfoil provides a case of laminar-separation-induced transition. It is a 0.6m chord airfoil designed for helicopter applications. Numerical results are compared to the experimental data from the ONERA F1 wind tunnel test [20]. An angle of attack α = 13.1° is employed with Reynolds number of 2.07 x 10^6. Appropriate boundary conditions are set in the computation to obtain a turbulence intensity of $Tu = 0.2\%$ with a viscosity ratio of $\frac{\nu_t}{\nu} = 10$ at the leading edge of the airfoil. A very fine C-mesh is used with strong clustering near the airfoil surface to guarantee a y+ of less than one on all parts of the airfoil.

Figure 5 shows numerical results for the coefficient of skin-friction along the airfoil surface using the WA-γ transition model. These results are compared to the SST-Transition model and the

experimental data. Both transition models compare very well with the experimental data. WA-γ is twice more efficient in computations compared to SST Transition model.

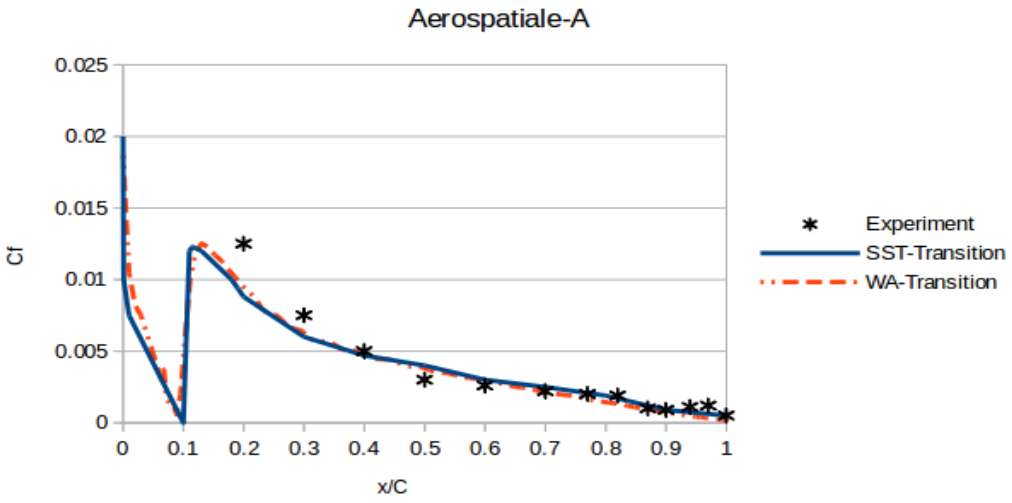

Figure 4.12: Results for Aerospatiale-A airfoil at α = 13.1°

4.3.3 NLR-7301 Two-Element Airfoil

The NLR-7301 two-element airfoil is also a commonly used configuration for validation of transitional flow. The configuration used in this study has a moderate flap angle of 20^0 which is a typical take-off flap setting. The gap width between the airfoil and flap is 2.6%c, where c is the chord of the main airfoil. The freestream conditions are α = 13.1° and Reynolds number = 2.51 x 10^6. A very fine C-mesh is used with strong clustering near the airfoil surface to guarantee a y+ of less than one on all parts of the airfoil and flap. Numerical results using WA-γ for the coefficient of pressure and friction are compared with the experimental data [21].

Figure 4.13 shows the pressure coefficient distribution on the airfoil and flap surfaces compared to the experimental values. Figure 4.14 shows a magnified perspective of the pressure coefficient values near the leading edge of the airfoil. The comparison of computations and experimental data shows that the transition model is able to capture the small separation bubble near the airfoil

leading edge. Figures 4.15 and 4.16 show the comparison of WA-γ numerical results for the skin friction coefficient on the airfoil and flap compared to the experimental data. The dashed bars mark the experimental transition location. The computational result using WA-γ transition model is in good agreement with the experimental data, and numerical transition prediction is only slightly ahead of the experimental transition location.

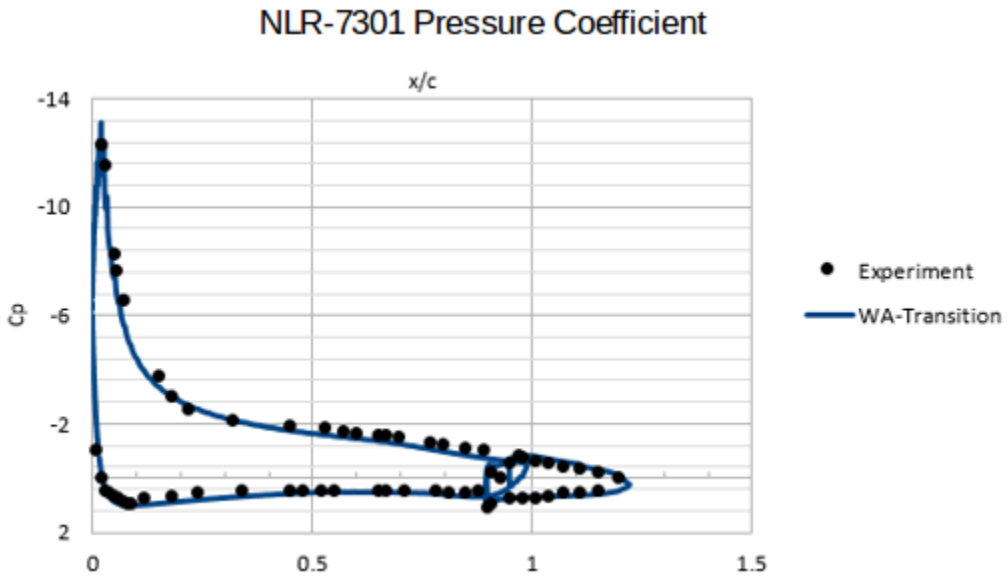

Figure 4.13: Pressure coefficient on the surface of NLR-7301 airfoil and flap.

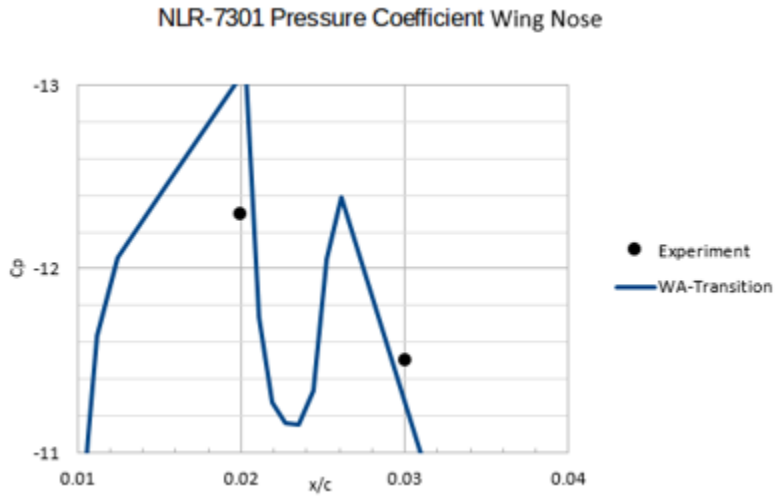

Figure 4.14: Pressure coefficient on NLR-7301 airfoil leading edge.

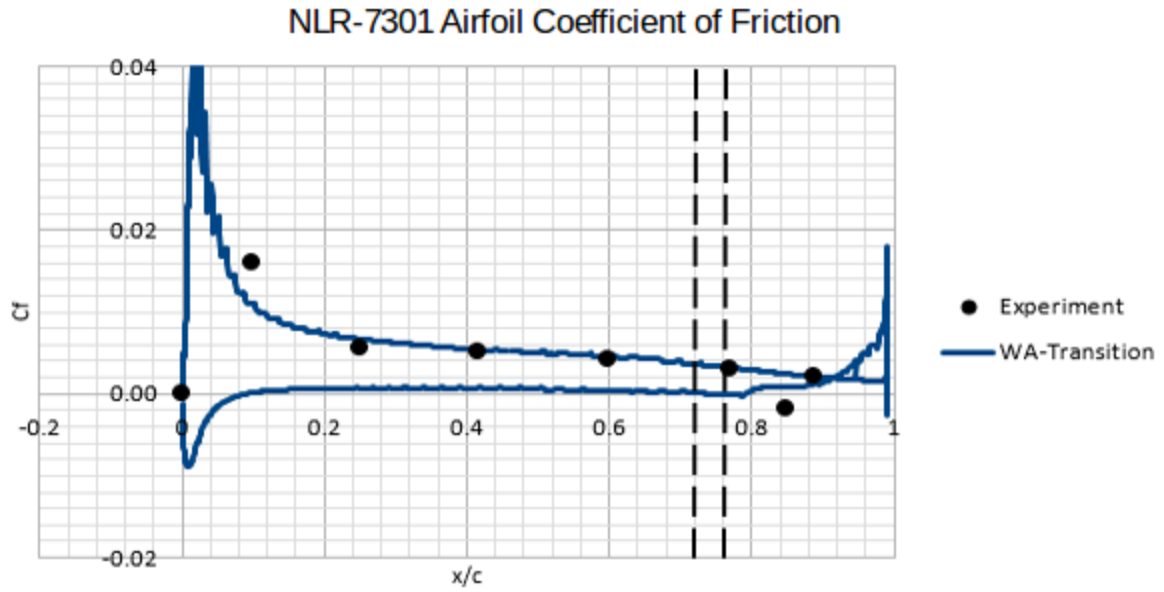

Figure 4.15: Skin-friction coefficient on NLR-7301 airfoil.

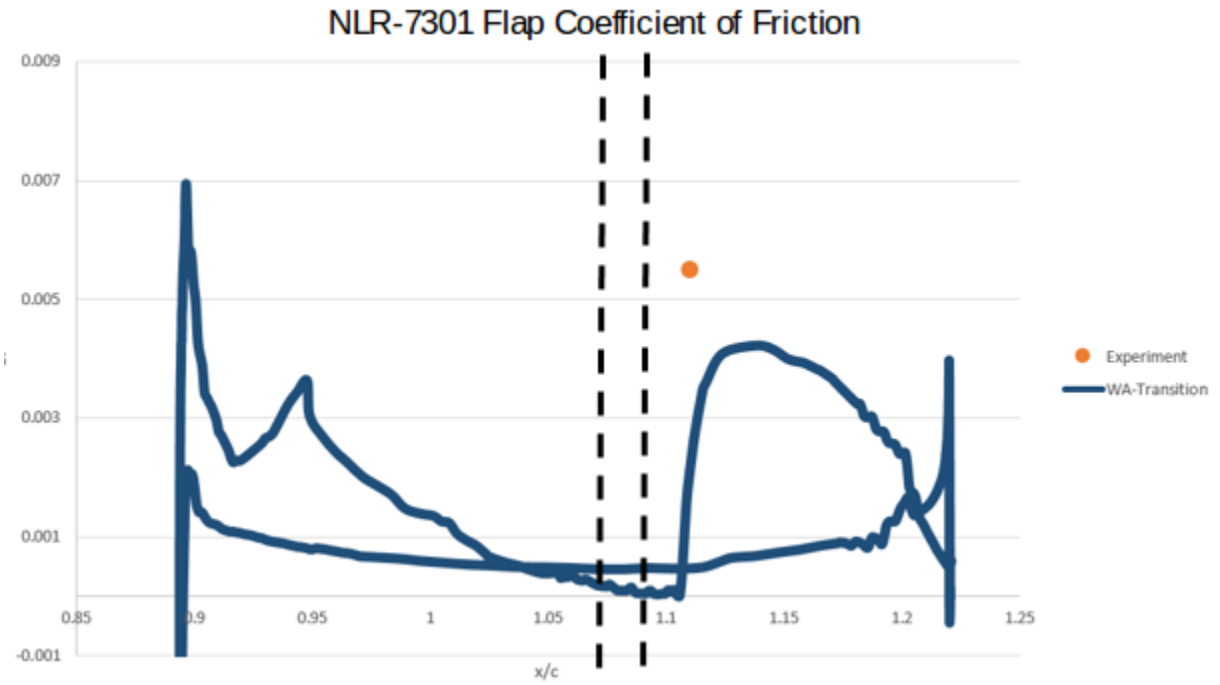

Figure 4.16: Friction coefficient on NLR-7301 flap.

4.3.4 Flow past a Circular Arc

Drag crisis is a well-known phenomenon first observed by Eiffel [22] more than a century ago. Experiments demonstrate that the drag crisis corresponds to narrowing of the wake of the bluff obstacle. Transition of the boundary layer around an object from laminar to turbulent moves the separation point further along on the rear surface of the object in the flow field. A critical Reynolds number associated with this transition is largely affected by the shape of the obstacle, its surface roughness, and the free stream turbulence intensity. Generally, drag crisis has been described for a symmetrical object, where there is almost no measurable lift force. Slender bodies at an angle of attack and airfoils/wings are designed to achieve large lift with low drag. If the incidence angle becomes too large, lift abruptly decreases due to separation and drag increases; this is also a well-known phenomenon known as stall. Recently, Bot et al. [23] showed experimentally that for a relatively streamlined non-symmetrical body, a sharp jump in lift can be observed as the flow transitions from laminar to turbulent at a critical Reynolds number. They called this sudden jump in lift as the lift crisis in drag crisis region; it is associated with flow transition on the upper surface boundary layer allowing the flow to remain attached further along the surface similar to the situation leading to drag crisis.

A two-dimensional structured mesh was generated for numerical simulations. The geometry of arc cylinder corresponding to the experiment [23] is shown in Figure 4.17. The circular arc section is a 3-mm-thick arc of radius 50mm with a chord length $c = 74.5\text{mm}$, and maximum height $\text{h} = 16.6\text{mm}$.

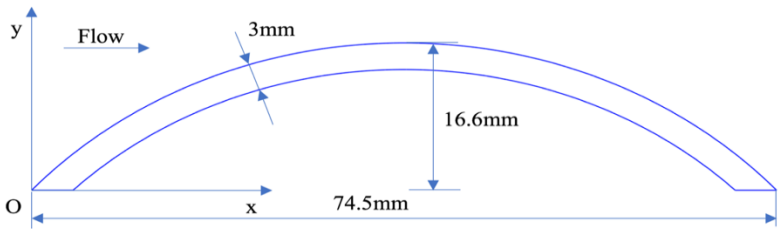

Figure 4.17: Geometry of the circular arc section.

Bot et al.'s experiments [23] were conducted in the IRENav hydrodynamic tunnel using a 192 × 192 mm test section. The 2D computational domain is created to replicate the experimental setup shown in Fig. 4.18.

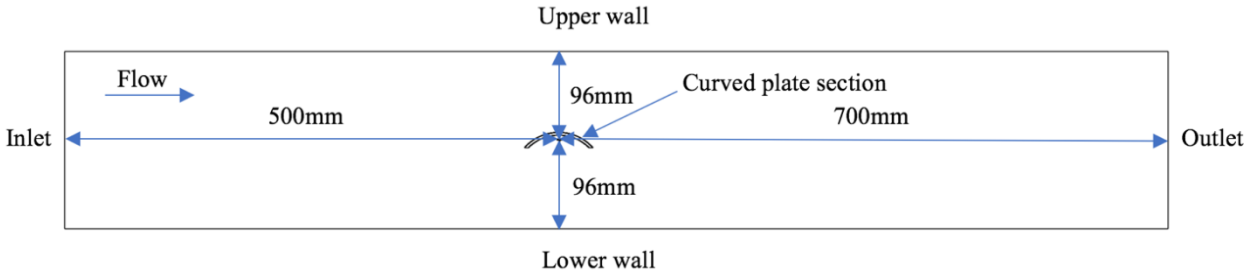

Figure 4.18: Computational domain around the circular arc.

The structured mesh around the circular arc cylinder in test section of the tunnel is shown in Fig. 4.19. The mesh contains about 215,000 elements. Two sharp corners of the curved plate were slightly modified with the radius of curvature of c/100 at the corner as shown in Figure 4.19(c). Corners were rounded to minimize the numerical error when approximating the elements of the metric tensor by using the central differencing. Very fine grid spacing is generated near wall boundaries to ensure that y+ < 1 everywhere on the arc walls.

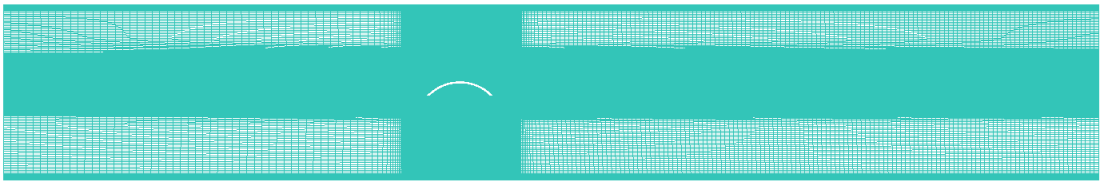

(a) Entire computational domain and mesh around circular arc

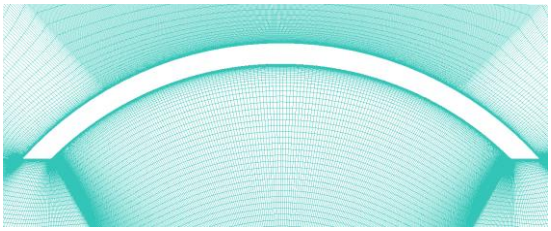

(b) Zoomed-in-view of mesh near the arc

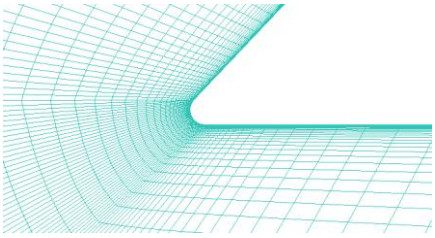

(c) Zoomed-in-view of mesh around the corner of the arc cylinder (radius of curvature at corner = *c*/100)

Figure 4.19: Computational domain and mesh around the circular arc.

The boundary conditions in the numerical calculations correspond to the experiment carried out in the hydrodynamic tunnel by Bot et al. [23]. The density and viscosity of the fluid is set as that of standard liquid water at room temperature. The left boundary of the domain is set as the velocity inlet in the horizontal direction corresponding to the uniform velocity of water upstream in the tunnel. The velocity ranges between 1.35 m/s and 8.09 m/s to achieve range of Reynolds numbers from 1×10^5 to 6×10^5. The turbulence intensity is set at 1.8% at both the velocity inlet and pressure outlet. No-slip conditions are applied to all wall boundary types.

For flow past the circular arc, both drag crisis and lift crisis were observed experimentally in a particular velocity range by Bot et al. [23]. Drag and lift crisis were observed past Reynolds number $\mathrm{Re} = 2 \times 10^5$, also known as the critical Reynolds number with an associated critical velocity. Figure 4.20 shows the computed results using WA-γ model for the coefficient of lift and their comparison to the experimental results from Bot et al. [23]; the theoretical calculations of Bot et al. based on circulation around the arc are also shown in Figure 4.20. In addition to numerical results from transition SST *k-ω* and *k-kl-ω* turbulence models [24, 32] are also shown. All numerical models predict the location of transition reasonably well showing sudden jump in lift (called lift crisis by Bot et al. [23]). It can be noted from Figure 4.20 that the WA-γ transition

model outperforms the other transition models, as its results are closest to the measured values and are well within the error bars for the laminar region. It also does not have a steep drop off for the lift coefficient at high Reynolds numbers when the flow is fully turbulent which can be observed in results from the SST-transition model. The results of WA-γ model and k-kl-ω are fairly close.

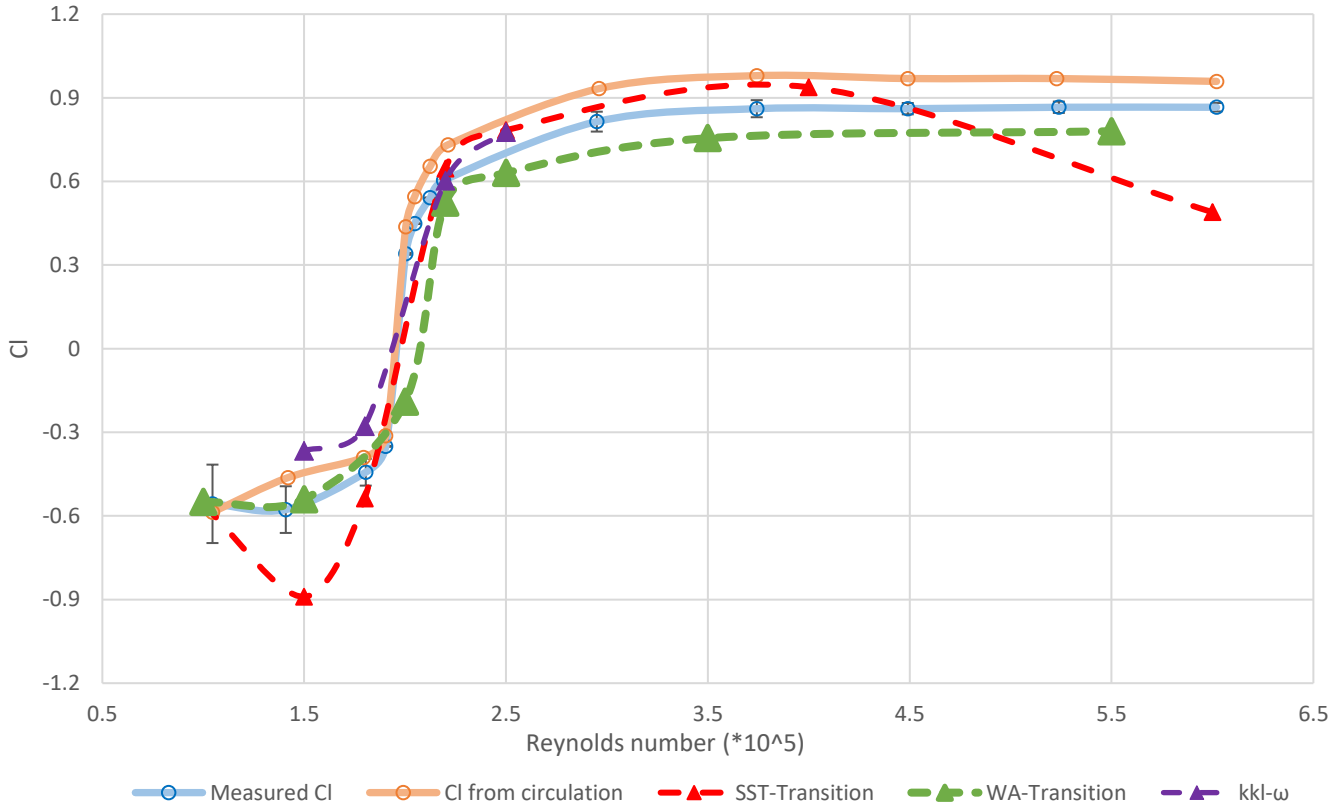

Figure 4.20: Lift coefficient C_L vs. Reynolds number for flow past the circular arc.

Figure 4.21 shows the numerical results from WA-γ model for the coefficient of drag and their comparison with the experimental results of Bot et al. [23] and numerical results obtained using the transition SST k-ω, and k-kl-ω models [24]. The WA-γ transition model and SST-Transition model both do reasonably well in predicting the drag crisis within a very tight margin to the experimental value, whereas the k-kl-ω seems to miss the mark to a much larger degree. None of the models correlates well with the measured drag coefficient values; however WA-γ transition

model shows superior performance compared to the other two models. Significant amount of errors are present within the experimental data in the laminar region as indicated by the error bars. The WA-γ transition model numerical results are either within or very close to these error bars.

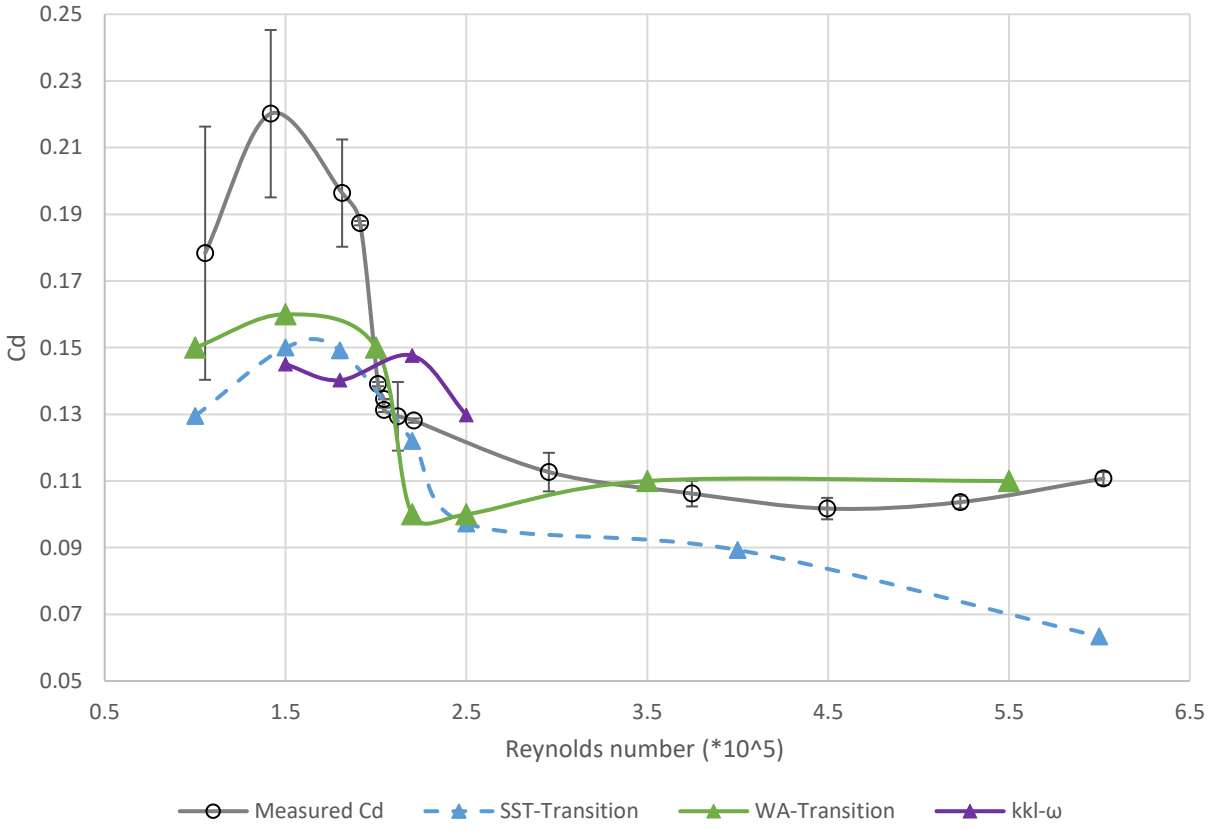

Figure 4.21: Drag coefficient C_D vs. Reynolds number for flow past the circular arc.

In the experiments performed by Bot et al. [23], velocity field measurements were obtained in order to better characterize the lift crisis. Values were taken from the wake created by the circular arc at locations x/c = 1.2 and x/c = 1.5. Figures 4.22(a) and 4.22(b) show the computed velocity profiles using the WA-γ transition model and their comparison with experimental data at x/c = 1.2 and x/c=1.5 at Reynolds number of 1.91 x 10^5, just before the lift crisis. The WA-γ transition model has nearly the same minimum velocity values in the wake as the experiment, but the computed values return to freestream velocity sooner than the experimental results. This indicates that the overall computed wake width is much narrower than that observed experimentally. Figures

4.23(a) and 4.23(b) show the computed velocity profiles using the WA-γ transition model and their comparison with experimental data at x/c = 1.2 and x/c=1.5 at Reynolds number of 2.05 x 10^5, just after the lift crisis. These figures show that the numerical results have slightly lower minimum velocities than the experimental results but the computed and experimental wake widths are nearly the same. Overall, the results show that the WA-γ transition model is able to predict the flow past a circular arc reasonably well including the lift crisis in the drag crisis region.

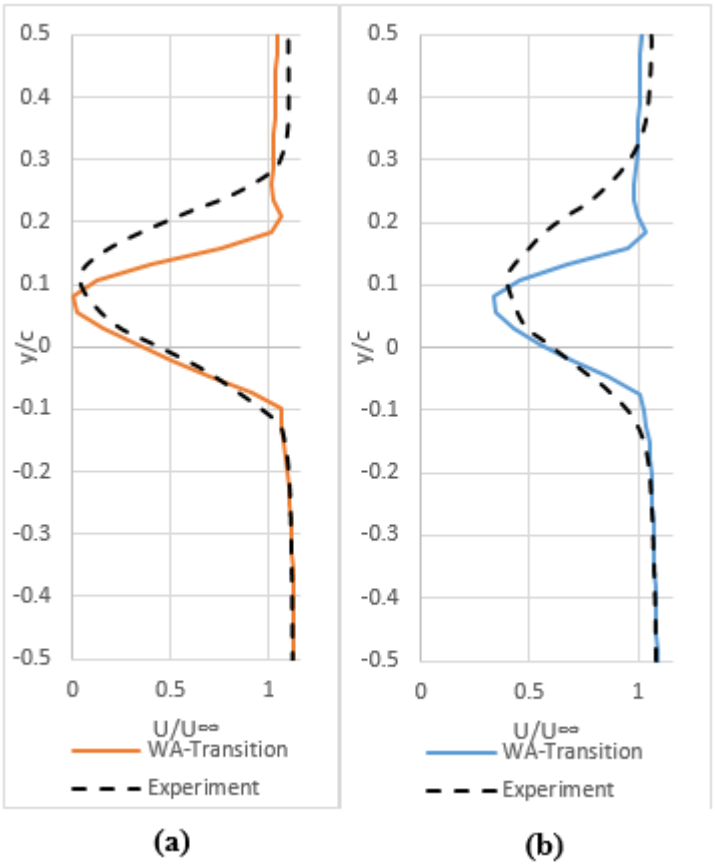

Figure 4.22: Computed and experimental velocity profiles at (a) x/c = 1.2 and (b) x/c=1.5 at Re = 1.91 x 10^5.

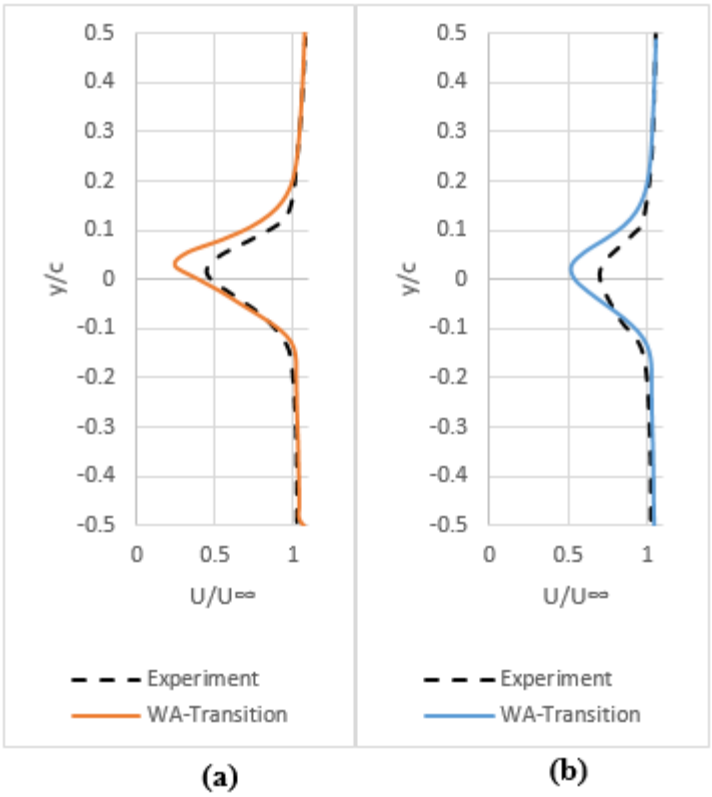

Figure 4.23: Computed and experimental velocity profiles at (a) x/c = 1.2 and (b) x/c=1.5 at Re = 2.05 x 10^5.

Chapter 5: Implementation of Crossflow Transition Effects in WA-γ Model

5.1 Crossflow Coupling with the WA-γ Transition model

Transition modeling has been a very challenging task within the turbulence modeling community due to many factors; lack of experimental data, complexity of transition physics, and the fact that transition can occur in at least four different modes which are known in the literature as natural transition, bypass transition, separation-induced transition, and crossflow induced transition. The WA-γ transition model, and many other commercial models, lack the ability for predicting the crossflow-induced transition. The goal of this chapter is to extend the WA-γ model to include the crossflow effects for predicting crossflow induced transition without adding any additional transport type equation.

Grabe et al. [25] have explored two variants of a correlation-based transport model that can predict transition due to crossflow instability. These two variants use the local C1-criterion [26] approach and the local helicity approach. The local helicity approach is chosen here and is used for crossflow-instability prediction in the WA-γ transition model [16]. This approach has the advantage that it uses many local quantities similar to the LCTM and requires nearly no modification of the original model, and as a result requires the least CPU overhead over the original WA-γ model.

The helicity crossflow model determines a local helicity value:

$$He = \vec{u} \cdot (\nabla \times \vec{u}) \tag{5.1}$$

The local helicity given by Eq. (5.1) is used to determine the helicity Reynolds number:

$$Re_{He} = \frac{\rho z^2 He}{\mu |\vec{u}|} \tag{5.2}$$

A helicity Reynolds number at transition onset, $Re_{He,t}{}^{+}$, is defined as a function of the stream wise shape factor *H* in order to account for the influence of the pressure gradient on the transition location. This transition onset Reynolds number is used to develop a critical crosswise Reynolds-number ratio:

$$\frac{Re_{He}}{Re_{He,t}{}^{+}} = 1 \tag{5.3}$$

Experimental data from various infinite swept wing flows as well as data from three-dimensional non wing-like configurations such as ellipsoids were used to develop an empirical transition criterion by Grabe et al. [25]. A curve fit through the numerical data gives:

$$Re_{He,t}{}^{+} = \max(-456.8H + 1332.7, 150.0) \tag{5.4}$$

As previously mentioned, *H* is approximated by the pressure gradient parameter λ^{+}. Note that this parameter is different from the parameter in the LCTM and has a constant, $C_{He,max}$ = 0.6944, calibrated by computations of flows over infinite swept wings:

$$\lambda^{+} = \frac{\rho l^2}{\mu} \frac{d|\vec{u}_e|}{d\vec{s}}, l = \frac{dw}{C_{He,max}} \frac{2}{15} \tag{5.5}$$

In Eq. (5.5), d_w is the wall distance and $\vec{u}_e$ is the local velocity at the boundary layer edge defined by the following equation.

$$|\overrightarrow{u_e}| = \sqrt{{u_\infty}^2 + \frac{2\tilde{\gamma}}{\tilde{\gamma} - 1}\left[1 - \left(\frac{P}{P_\infty}\right)^{1-\frac{1}{\tilde{\gamma}}}\right]\frac{P_\infty}{\rho_\infty}} \tag{5.6}$$

where $\tilde{\gamma}$ is the heat capacity ratio. The shape factor H is computed using the correlation of Cliquet et al. [27].

$$H = 4.02923 - \sqrt{-8838.4\lambda^{+4} + 1105.1\lambda^{+3} - 67.962\lambda^{+2} + 17.574\lambda^{+} + 2.0593} \tag{5.7}$$

A new set of onset functions are used to implement the helicity crossflow approach into the intermittency equations. These equations are the following:

$$\begin{aligned} F_{onset1,cf} &= \frac{C * Re_{He}}{Re_{He,t}^{+}}, C = 1.4, \\ F_{onset2,cf} &= \min(\max(F_{onset1,cf}, F_{onset1,cf}^{4}), 2.0) \\ F_{onset,cf} &= \max\left(F_{onset2,cf} - max\left(1 - \frac{R_T}{3.5}, 0.0\right), 0.0\right) \end{aligned} \tag{5.8}$$

The crossflow onset is implemented into the intermittency transport equation given by:

$$\begin{aligned} \frac{\partial \rho\gamma}{\partial t} + \frac{\partial \rho u_j \gamma}{\partial x_j} = \frac{\partial}{\partial x_j}\left[\left(\mu + \frac{\mu_T}{\sigma_\gamma}\right)\frac{\partial \gamma}{\partial x_j}\right] + \rho S\gamma(1-\gamma)(F_{length}F_{onset} + F_{length,cf}F_{onset,cf}) \\ -\rho c_{a2}\Omega\gamma F_{turb}(c_{e2}\gamma - 1) \end{aligned} \tag{5.9}$$

where $F_{length,cf} = 5.0$.

The main advantage of using the local helicity approach is that it is not restricted to certain geometries and can be applied to arbitrarily shaped configurations.

5.2 Flow past a Prolate Spheroid

The 6:1 inclined prolate spheroid [28] has a simple geometry but is a challenging configuration for transition predictions due to its non-wing like geometry. The flow around the spheroid shape is comparable to flow around a commercial aircraft fuselage and exhibits complex flow features. The major and minor axis lengths of the experimental and numerical geometry are 2.4 and 0.4 meters respectively. Figure 5.1 shows the geometry of the prolate spheroid.

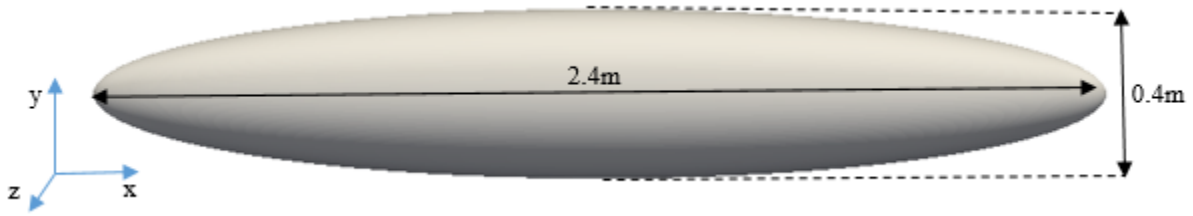

Figure 5.1: Prolate spheroid geometry.

The flow Reynolds number based on the major axis and freestream velocity is 6.5 x 10^5. Turbulence intensity was set at 0.2%. Very fine grid spacing is generated near wall boundaries to ensure that y+ < 1 everywhere on the spheroid surface. More than 6.5 million finite volume cells were used to generate the mesh in the computational domain.

Transitional flow at two different angles of attack, - 5 degree and 15 degree, was investigated. Skin friction contour plots for numerical and experimental results [29] at 5^o angle of attack are shown in Fig. 5.2. Laminar to turbulent flow transition takes place nearly halfway along the surface of the prolate spheroid. Both transition models, WA-γ and WA-γ- Crossflow capture the laminar flow region on the upstream side of the spheroid, but without the crossflow the WA-γ model significantly underestimates the skin friction distribution. The addition of crossflow captures the general shape of the transition region, however inconsistencies can be observed in the lower half of the spheroid. Same problem was observed by Grabe et al [25] and Langtry et al. [30] and remains a topic of further investigation. Nevertheless, WA-γ- Crossflow model gives much improved results.

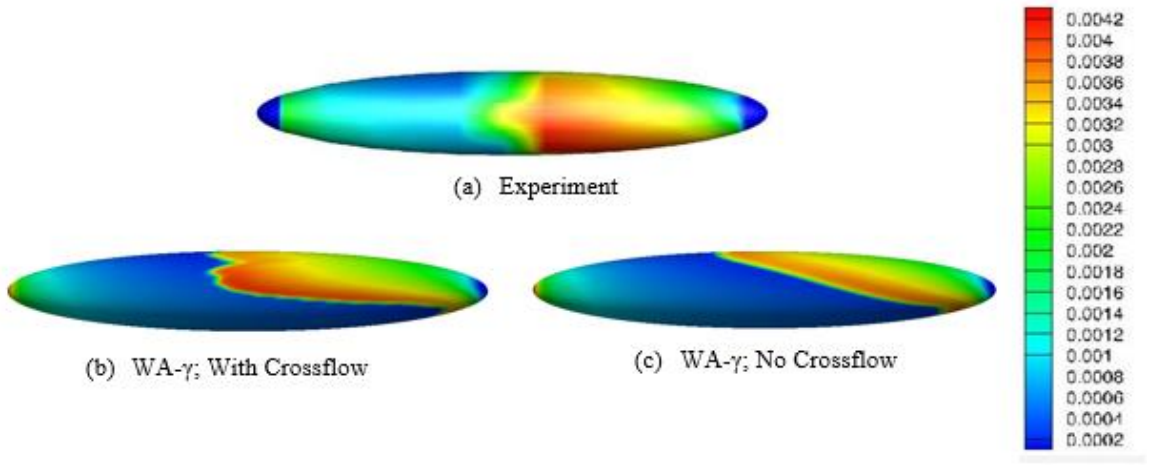

Figure 5.2: Coefficient of skin-friction contours on prolate spheroid at 5º angle of attack.

A plot of the coefficient of skin friction along the center line of the X-Z plane over the prolate spheroid at 5º angle of attack is shown in Figure 5.3. The WA-γ transition model without crossflow predicts transition near the back end of the spheroid whereas the results with WA-γ-Crossflow transition model align with experimental data very well. The model is able to predict the correct location of transition onset as well as the correct skin friction values measured in the experiment.

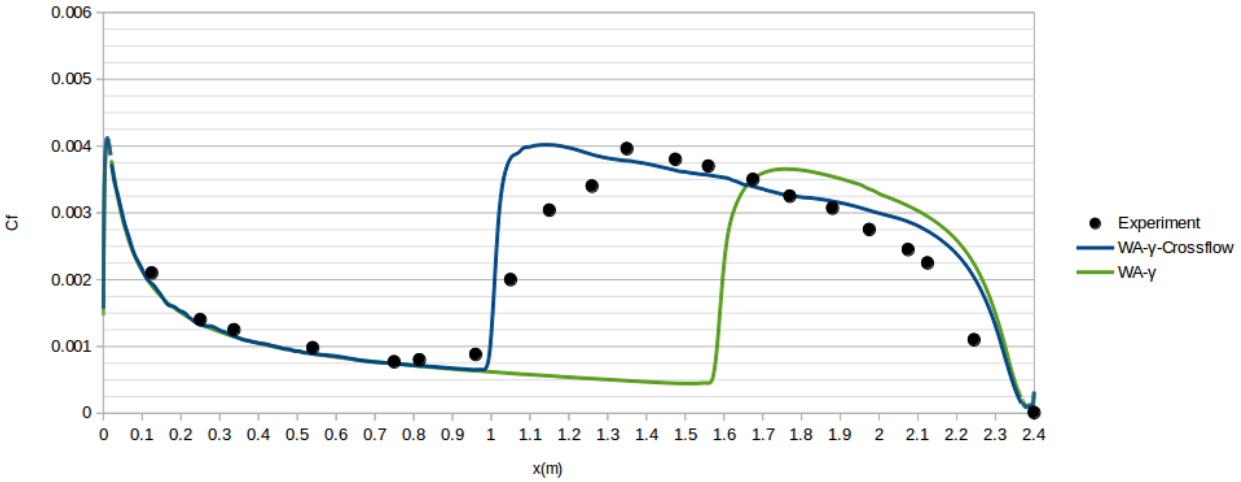

Figure 5.3: Comparison of coefficient of skin-friction along the centerline of X-Z plane of the prolate spheroid at α = 5º.

Computed skin-friction contour plots using the WA-γ model without and with crossflow along with the experimental results [29] at 15º angle of attack are shown in Fig. 5.4. The results for WA-

γ transition model without crossflow underestimate the skin friction distribution. Adding the crossflow in WA-γ model resulted in better agreement with the experimental values for the transition onset location. At this angle of attack, unlike what was observed at 5^{o} angle of attack, it seems that the numerical models are also able to predict transition onset further down the spheroid surface.

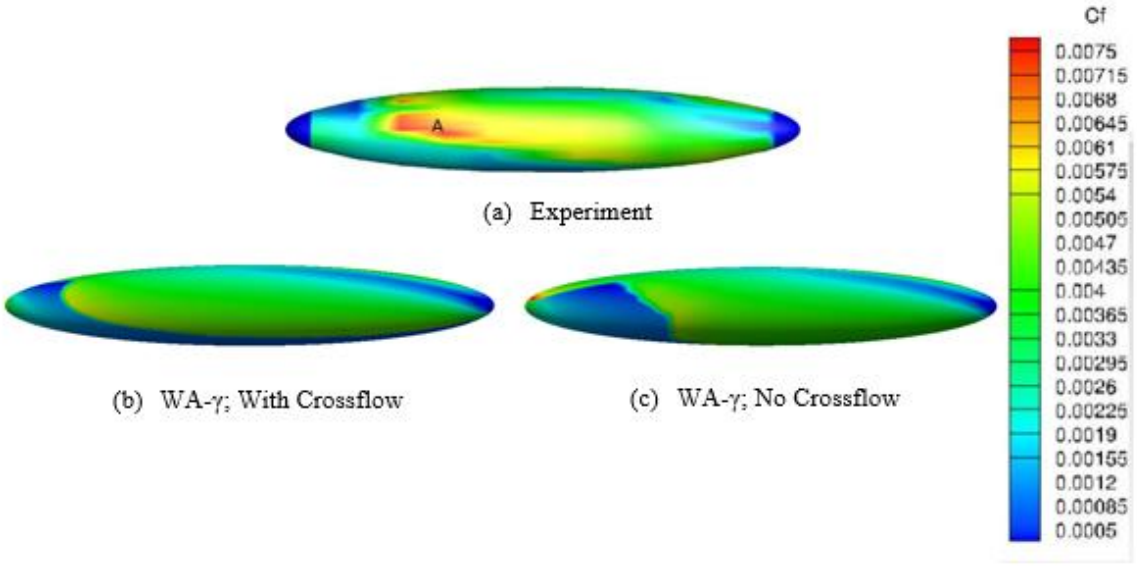

Figure 5.4: Comparison of coefficient of skin-friction contours on prolate spheroid at 15^{o} angle of attack.

A plot of the coefficient of skin-friction along the center line of the X-Z plane on the prolate spheroid at 15^{o} angle of attack is shown in Fig. 5.5. Although the WA-γ transition model without crossflow is able to predict transition onset further upstream, it still does not match the transition onset region observed experimentally without the addition of crossflow. Discrepancies are observed in the peak values of the coefficient of skin-friction right after the transition onset. Even fully turbulent flow models reflect similar low skin friction values, which can lead one to believe that this may be a turbulence issue and not a fault of the transition model as discussed by Pillai and Lardeau [31].

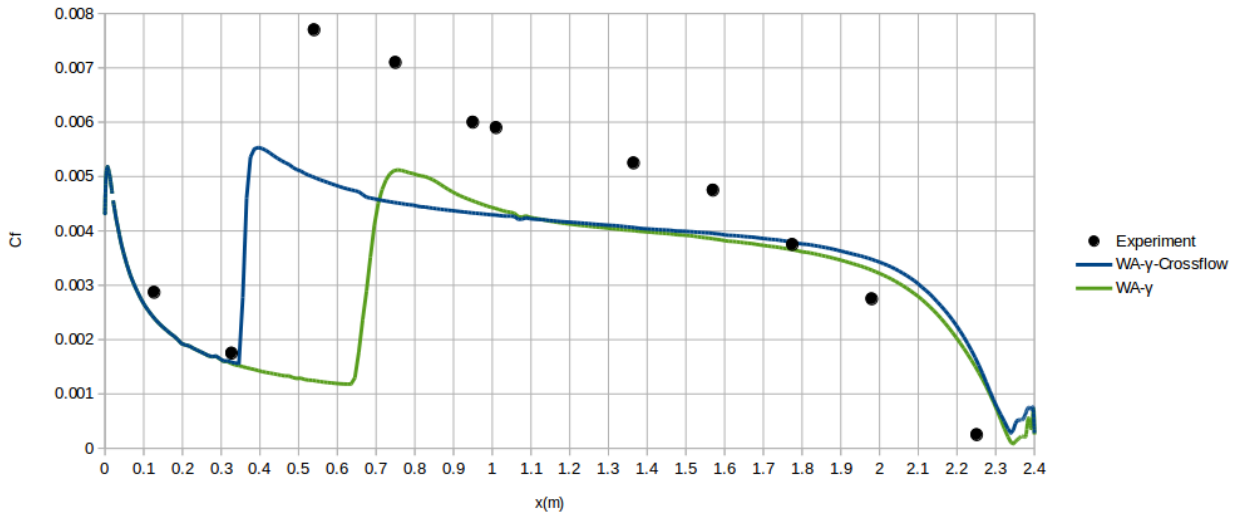

Figure 5.5 :Comparison of coefficient of skin-friction along the centerline of X-Z plane on prolate spheroid at $\alpha = 15^{o}$.

Chapter 6: Summary and Future Work

6.1 Summary

The quadratic constitutive relation (QCR) was successfully implemented in OpenFOAM with SA, SST k-ω and WA turbulence models. The accuracy of QCR models compared to standard linear SA, SST k-ω and WA turbulence models was evaluated by computing seven different flows: boundary layer flow past a flat plate, flow in a lid-driven cavity, flow over a backward facing step, flow past a NACA 4412 airfoil, supersonic flow in a square duct, flow due to a two-dimensional impinging shock on a flat plate, and a three-dimensional oblique shock boundary layer interaction. All models agreed well with the skin friction results for turbulent boundary layer flow past a flat plate as expected. This test case verified that all the QCR models were correctly implemented in OpenFOAM. Differences in QCR and standard linear eddy-viscosity model results were observed in case of flow in a lid-driven cavity. The SA-QCR model improved its ability to predict additional secondary eddies in the corners as well as obtained results for the velocity profiles in better agreement with the experimental data. The WA-QCR model also showed minor improvement in computation of velocity components when compared to the experimental data. However, the SST-QCR model showed no definitive improvement and showed the same results as the standard SST k-ω model. For the flow over a backward facing step, NACA 4412 airfoil, and two-dimensional impinging shock, the QCR models showed no improvement over the standard models, which was unexpected. The computation of 3D supersonic flow in a square duct showed visible improvement when QCR models were used. The three-dimensional oblique shock boundary layer interaction case showed that there is some significant effect with the use of QCR for high velocity corner flows. The QCR models were all able to compute secondary flows where available whereas

standard models could not. It is concluded that QCR models can be beneficial compared to standard turbulence models with a small added computational effort and cost.

An additional accomplishment of this research has been the implementation and verification of the local correlation-based transition-modelling concept in OpenFOAM with the Wray-Agarwal (WA) wall-distance-free turbulence model [4]. The accuracy of the Wray-Agarwal-transition model WA-γ was evaluated by computing several ERCOFTAC benchmark flat plate transition cases in zero and mildly varying pressure gradients and comparing them with the experimental data and the numerical results from four equation SST transition model. The two-equation WA-γ transition model outperformed the four-equation SST-Transition model in accuracy for all three zero-pressure gradient T3 flat plates transitional flow cases. The WA-γ model also performed very well in accurately predicting the experimental results for the non-zero-pressure gradient T3C flat plates transitional flow cases. Transitional flow past two 2D airfoils namely the S809 airfoil and Aerospatiale-A airfoil was also computed using both the WA-γ transition and SST-Transition model. Both models predicted the experimental data very well, with the WA-γ transition being on par or slightly better than the SST-Transition model. Transitional flow past the NRL-7301 two-element airfoil and a circular arc was also computed using the WA-γ transition model and performed very well when compared to the experimental data. Overall, the WA-γ transition model showed very good numerical predictions and matched or exceeded the results from SST-Transition model in transition prediction both in accuracy and efficiency.

The WA-γ transition model was extended to account for crossflow-induced transition in a very simple and effective way. The WA-γ-Crossflow transition model is based on the local helicity approach to predict the onset of crossflow transition. Efforts were made to maintain simplicity and to keep the basic validated properties of the original WA-γ transition model for prediction of by-

pass and separation-induced transition. Transitional flow simulations for flow past a prolate spheroid at two different angles of attack confirmed the effectiveness of the model in accounting for crossflow effects. Values of skin friction along various planes of the spheroid as well as the contour plots of skin friction on the body demonstrated that the WA-γ-Crossflow model was able to predict the general features and shape of the transition regime on a three-dimensional body like spheroid as attested by comparisons with the experimental data. Further validation should be done by computing 3D flow past swept wings and other body shapes for which experimental data is available.

6.2 Future Work: Inclusion of Surface Roughness in Transition Model

Surface roughness is an important factor when considering transition onset of flow from laminar to turbulence. Roughness is a common side effect caused by manufacturing or by environmental degradation of the surface material, such as erosion. Surface conditions play a major role in boundary-layer characteristics and it is important that transition models can account for it. Langtry et al. [30] reported a logarithmic dependency between stationary crossflow Reynolds number and the surface roughness. A similar approach can be used to mimic the roughness effect into the crossflow model. This approach, used by Pillai et al. [31], adds a roughness constant, C_r, which is defined as

$$C_r = 2.0 - 0.5^{\frac{h}{h_o}} \tag{6.1}$$

where h is the surface roughness and h_o is a constant with a value of 0.25 μm. This roughness constant could be used to modify the transition onset equation as follows:

$$F_{onset1,cf} = \frac{C_r * C * Re_{He}}{Re_{He,t}{}^{+}} \tag{6.2}$$

The correlation and relative constants must be calibrated using crossflow case with varying roughness. The NLF(2)-0415 airfoil case is one such case that can be used. This case is a classical swept wing configuration used to calibrate crossflow transition with roughness effects. The NLF(2)-0415 was experimentally investigated at Arizona State University [33]. This infinite swept wing airfoil has a fixed sweep angle of 45 degree with a flow angle of attack of -4 degree. A range of Reynolds numbers along with varying surface roughness levels should be used to compare to the experimental data shown in Fig. 6.1. This figure shows the varying chordwise transition location on the airfoil as a function of Reynolds number with three different roughness values along the upper surface of the airfoil. Additionally, replacing the use of helicity in the model should be a top priority in order to preserve the Galilean invariance, which is the case with the original WA-γ transition model. This will extend the models applicability to cases involving moving reference frames.

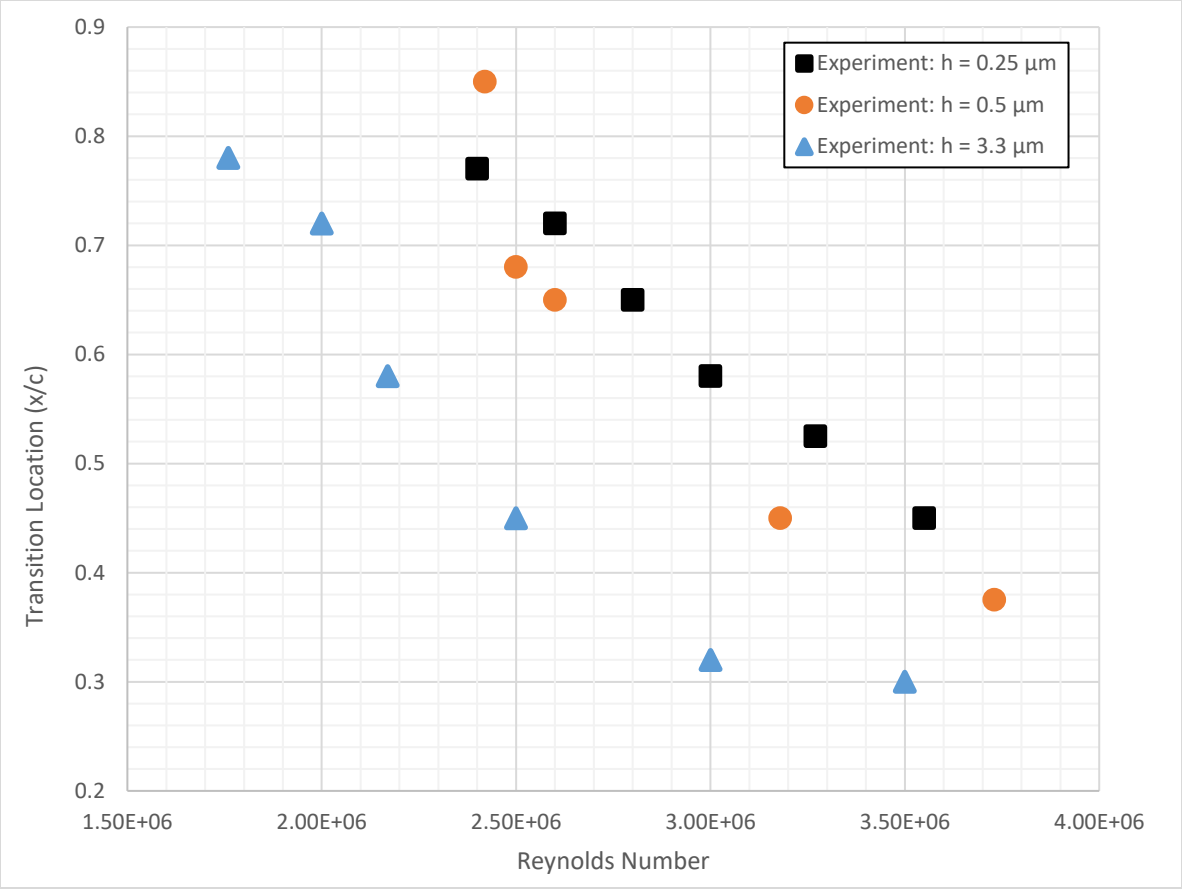

Figure 6.1: Transition location on upper surface of a rough airfoil vs. Reynolds number.

References

1. Spalart, P. R. and Allmaras, S. R, "A One Equation Turbulence Model for Aerodynamic Flows," AIAA Paper 1992-0439, 1992.

2. Menter, F. R., "Two-Equation Eddy-Viscosity Turbulence Models for Engineering Applications," AIAA J., Vol. 32, No. 8, August 1994, pp. 1598-1605.

3. Wray-Agarwal turbulence model, https://turbmodels.larc.nasa.gov/wray_agarwal.html. [retrieved November 2017]

4. Han, X., Wray, T. J., and Agarwal, R. K., "Application of a New DES Model Based on Wray-Agarwal Turbulence Model for Simulation of Wall-Bounded Flows with Separation," AIAA Paper 2017-3966, AIAA Aviation Forum, Denver, 5-9 June 2017.

5. Spalart, P. R., "Strategies for Turbulence Modeling and Simulations," Int. J. Heat Fluid Flow, Vol. 21, 2000, pp. 252-263.

6. Menter, F. R., Langtry, R.B., Smirnov, P. E. and Liu, T., "A One-Equation Local Correlation-Based Transition Model," Flow, Turbulence and Combustion, Vol. 5, No. 4, 2015, pp. 583-619

7. NASA Langley Research Center Turbulence Modeling Resource, http://turbmodels.larc.nasa.gov [retrieved October 2015]

8. Erturk, E., Corke, T., and Gökcöl, C., "Numerical Solutions of 2-D Steady Incompressible Driven Cavity Flow at High Reynolds Numbers," International J. of Numerical Methods in Fluids," Vol. 48, 2005, pp. 747-774.

9. Driver, D. M. and Seegmiller, H. L., "Features of Reattaching Turbulent Shear Layer in Divergent Channel Flow," AIAA Journal, Vol. 23, No. 2, Feb. 1985, pp. 163-171.

10. Coles, D. and Wadcock, A. J., "Flying-Hot-Wire Study of Flow Past an NACA 4412 Airfoil at Maximum Lift," AIAA Journal, Vol. 17, No. 4, April 1979, pp. 321-329.

11. Wellbom, S. R., Okiishi, T. H., and Reichert, B. A., "A Study of Compressible Flow Through a Diffusing S-Duct," NASA TM-106411, Dec, 1993.

12. E. Schulein, P. Krogmann, and E. Stanewsky, "Documentation of Two-Dimensional Impinging Shock/Turbulent Boundary Layer Interaction Flow," DLR Rep., vol. DLR IB 223-96 A 49, Oct. 1996.

13. Benek, J. A., Suchyta, C. J., "Simulations of Incident Shock Boundary Layer Interactions," AIAA Paper 2016-0352, AIAA SciTech Forum, San Diego, CA, 4-8 Jan. 2016.

14. Menter, F. R., Langtry, R. B., Likki, S. R., Suzen, Y. B., Huang, P. G., and Völker, S., "A Correlation-Based Transition Model Using Local Variables — Part I: Model Formulation," ASME Journal of Turbomachinery, Vol. 128, July 2006, pp. 413-422.

15. Han, X., Rahman, M. M., and Agarwal, R. K., "Development and Application of a Wall Distance Free Wray-Agarwal Turbulence Model," AIAA Paper 2018-0593, AIAA SciTech Forum, Kissimmee, FL, 8-12 January 2018.

16. Nagapetyan, H. J. and Agarwal, R. K., "Development of a New Transitional Flow Model Integrating the Wray-Agarwal Turbulence Model with an Intermittency Transport Equation," 2018 Fluid Dynamics Conference, AIAA AVIATION Forum, (AIAA 2018-3384).

17. ERCOFTAC (European Research Community on Flow, Turbulence and Combustion), http://ercoftac.mech.surrey.ac.uk/ [retrieved 15 Feb 2008]

18. Suluksna, K., Dechaumphai, P., and Juntasaro E., "Correlations for Modeling Transitional Boundary Layers under Influences of Freestream Turbulence and Pressure Gradient," Int. J. Heat and Fluid Flow, Vol. 30, 2009, pp. 66-75.

19. Somers, D. M., "Design and Experimental Results for the S809 Airfoil," Airfoils Inc., State College, PA, Jan 1997.

20. Chaput, E., "Chapter III: Application-Oriented Synthesis of Work Presented in Chapter II." Notes on Numerical Fluid Mechanics, Vol. 58, 1997, pp. 327-346.

21. Van den Berg, B., "Boundary Layer Measurements on a Two-Dimensional Wing with Flap," Report No: NLR TW 79009U, National Aerospace Laboratory, Netherlands, 1979.

22. Eiffel, G., "Sur la résistance des sphères dans l'air en movement," Comptes Rendus, Vol. 155, 1912, pp. 1597-1599.

23. Bot, P., Rabaud, M., Thomas, G., Lombardi, A., and Lebret, C., "Sharp Transition in the Lift Force of a Fluid Flowing Past Nonsymmetrical Obstacles: Evidence for a Lift Crisis in the Drag Crisis Regime," Physical Review Letters, Vol. 117, 2016, DOI: 10.1103/PhysRevLett.117.234501.

24. Zhang, L., Wray, T., and Agarwal, R. K., "Numerical Simulation of Flow Past a Circular and a Square Cylinder at High Reynolds Number," AIAA Paper 2017-3322, AIAA Aviation 2017 Conference, Denver, 5-9 June 2017.

25. Grabe, C., Shengyang, N., Krumbein, A., "Transition Transport Modeling for the Prediction of Crossflow Transition," AIAA Paper 2016-3572, 34th AIAA Applied Aerodynamics Conference, Washington, D.C.,13-17 June 2016.

26. Arnal, D., Habiballah, M. and Coustols, C., “Laminar Instability Theory and Transition Criteria in Two- and Three-Dimensional Flows," La Recherche Aerospatiale, 1984-2, 1984.

27. Cliquet, J., Houdeville, R., Arnal, D., “Application of Laminar-Turbulent Transition Criteria in Navier-Stokes Computations," AIAA Journal, Vol. 46, No. 5, 2008, pp. 1182-1190.

28. Kreplin, H.-P., Vollmers, H., Meier, H. U., “Wall Shear Stress Measurements on an Inclined Prolate Spheroid in the DFVLR 3 m x 3 m Low Speed Wind Tunnel," Göttingen, DFVLR-AVA, report IB 22-84 A 33, 1985.

29. Vizinho, R., P_ascoa, J. and Silvestre, M., "Analysis of Transitional Flow in 3D Geometries Using a Novel Phenomenological Model," Aerospace Science and Technology, Volume 45, September 2015, Pages 431-441.

30. Langtry, R. B., Sengupta, K., Yeh, D. T. and Dorgan, A. J., “Extending the γ-$Re_{\theta t}$ Local Correlation based Transition Model for Crossflow Effects," AIAA 2015-2474, 45th AIAA Fluid Dynamics Conference, Dallas, TX, 22-26 June 2015.

31. Pillai, S. V. and Lardeau, S., “Accounting Crossflow Effects in One-Equation Local Correlation-Based Transition Model,” AIAA Paper 2017-3000, 8th AIAA Theoretical Fluid Mechanics Conference, Denver, Colorado, 5-9 June 2017.

32. Walters, K. and Cokljat, D., “A Three-Equation Eddy-Viscosity Model for Reynolds-Averaged Navier–Stokes Simulations of Transitional Flow,” ASME J. of Fluids Engineering, Vol. 130, No. 12, 2008, pp. 121101-121101-12.

33. Radeztsky, R. H., Reibert, M. S., Saric, W. S., and Takagi, S., “Effect of Micron-Sized Roughness on Transition in Swept-Wing Flows,” AIAA Paper 93-0076, Jan. 1993.

Vita

Hakop J. Nagapetyan

EDUCATION

Ph.D. in Aerospace Engineering, Department of Mechanical Engineering and Materials Science, Washington University in St. Louis, Saint Louis, MO. 2015-2018

M.S. in Aerospace Engineering, Department of Mechanical Engineering and Materials Science, Washington University in St. Louis, Saint Louis, MO. 2014-2015

B.S. in Aerospace and Mechanical Engineering, Department of Mechanical and Aerospace Engineering, Case Western Reserve University, Cleveland, OH. 2009-2013

PUBLICATIONS

Nagapetyan, H. J., Wray, T., and Agarwal, R. K. "Computation of Turbulent Flow in a Lid-Driven 2D Cavity and a 3D Box Using a Number of Turbulence Models", AIAA 2016-1114, 54th AIAA Aerospace Sciences Meeting, San Diego, CA, 4-8 Jan. 2016.

Nagapetyan, H. J., Wray, T., and Agarwal, R. K. "Application of the Quadratic Constitutive Relation to Various Turbulence Models in OpenFOAM", AIAA 2016-3476, 46th AIAA Fluid Dynamics Conference, Washington, D.C., 13-17 June 2016.

Nagapetyan, H. J. and Agarwal, R. K., "Development of a New Transitional Flow Model Integrating the Wray-Agarwal Turbulence Model with an Intermittency Transport Equation," AIAA 2018-3384, 2018 Fluid Dynamics Conference, Atlanta, GA, 25-29 June 2018.

PROFESSIONAL MEMBERSHIP

American Institute of Aeronautics and Astronautics (AIAA)